Marshall Plan Research Paper

Remote Sensing-based Detection of Spatiotemporal Patterns of Urban Heat Islands

Author:	Saghi Sarafi (MSc.)
Master Program:	Spatial Information Management
Internal Supervisors:	Prof. Dr. Gernot Paulus Prof. Dr. Karl-Heinrich Anders
External Supervisor:	Prof. Dr. Christopher Lippitt; University of New Mexico

Villach (Austria), Febuary 2023

ABSTRACT

The urban heat island (UHI) effect, which is caused by the physical characteristics of cities, raises temperatures unnaturally in urban areas. Urban and rural surface temperature differences can vary significantly on a daily and seasonal basis. For many studies evaluating the state of the land's surface, such as those looking at urban climate, evapotranspiration, and vegetation stress, the importance of land surface temperature (LST) is rising. Therefore, the purpose of this study is to detect UHI in twelve distinct cities located in various climate performance zones. The analysis is based on land cover (LC) classification since the UHI effect is a typical urban climatic phenomenon and the creation and intensity of these phenomena are directly tied to the type of LC (urban, blue, green, cropland and bare areas). This study uses computing Landsat LST code that is provided by (Ermida, et al., 2020) for the year 1990, 2005, and 2021 to extract LSTs maps and compare with LC maps to extract the effects of different LC classes on the LST based on Landsat-5, 7, and 8 remote sensing images of the selected test sites within Google Earth Engine (GEE).

According to the results, there is a considerable UHI effect since the LST of urban impervious surfaces is significantly higher than that of vegetation-covered areas by a difference of 6–8 K. The temperature difference between urban areas and blue areas varies from 1 to 13 K, between urban areas and cropland areas from 2 to 8 K, between urban areas and bare areas from 11 to 18 K, and between bare and cropland areas from 13 to 30 K. The temperature difference between cropland and green areas varies from 10 to 18 K. Each of the LC classes had different LST values, and certain regions within the five classes had lower or higher LST values than those inside other categories. As a result, when compared to other categories, one category may not necessarily have the greatest LST value.

This work contributes to our understanding of how to improve urban landscapes and reduce the UHI effect. The findings of this study may also provide useful recommendations for urban planners who want to lessen the consequences of UHI in urban areas.

Keywords: urban heat island (UHI), remote sensing (RS), climate change, google earth engine (GEE)

Contents

STATUTORY DECLARATION ..... ERROR! BOOKMARK NOT DEFINED.

ABSTRACT **2**

LIST OF FIGURES **5**

LIST OF TABLES **6**

1 INTRODUCTION **7**

1.1 Motivation 7
1.2 General Objectives 8
1.3 Methodological Considerations 8
1.4 Relevance and Expected Results 11
1.5 Intended Audience and Thesis Structure 11

2 USING REMOTE SENSING TO DETECT URBAN HEAT ISLAND (UHI) IN THE LITERATURE OVERVIEW **12**

2.1 Understanding the Connotation of UHI 12
2.1.1 Definition of UHI *12*
2.1.2 Characteristics of UHI *13*
2.1.3 UHI Contributing Factors *14*
2.1.4 UHI Effect *16*
2.1.5 UHI Metrics *17*
2.2 GI Technology to Detect UHI 18
2.2.1 Thermal Sensors *18*
2.2.2 Classification of Thermal Sensors *21*
2.3 Possible Remedies for UHI 22
2.3.1 Existing UHI Mitigation Strategies *22*
2.3.2 Criteria to Mitigate UHI Phenomenon *23*

3 UHI DETECTION APPROACH **24**

3.1 Data Requirements for detecting UHIs 24
..... 25
3.2 Software Employed_ GOOGLE EARTH ENGINE (GEE) 26
3.3 Deriving Criteria for Assessment of Land Surface Temperature Measurement 26
3.3.1 Landsat Data *27*
3.3.2 Total Column Water Vapor Data *27*
3.3.3 Surface Emissivity *27*
3.3.4 Retrieval of Land Surface Temperature (LST) *27*
3.3.5 Conceptual Model of Land Surface Temperature Estimation *28*

4 IMPLEMENTATION OF THE UHI DETECTION MODEL **30**

4.1 Study Area 30
4.1.1 Human Characteristics *30*
4.1.2 physical Characteristics *31*
4.2 Geo Database 34
4.3 Spatiotemporal Analysis 37
4.4 LST Validation 42
4.4.1 In-situ LST Derivation *42*
4.4.2. Statistical Analysis *43*

5 RESULTS **44**

5.1 UHI Maps Visualization 44
5.2 Spatiotemporal Pattern of LC Dynamics 48
5.3 UHIs Spatial Patterns and Temporal Variations 58
5.4 UHI Remedies Recommendations 58

5.5 SHORT TERM SOLUTIONS 59
5.5.1 Use of Light-colored Concrete and White Roofs 59
5.5.2 Green Roofs 60
5.5.3 Green walls 60
5.5.4 Planting Trees in Cities 60
5.5.5 Green Parking Lots 60
5.6 LONG TERM SOLUTIONS 60
5.6.1 Vegetation Cover 61
5.6.2 Cool Pavement 63
5.6.3 Cool and Green Roofs 64

6 DISCUSSION OF CONTROVERSIAL ISSUES 65

7 SUMMARY AND FUTURE WORK 67

7.1 SUMMARY 67
7.2 FUTURE WORK 67

8 CONCLUSION 69

ACKNOWLEDGMENTS 70

BIBLIOGRAPHY 70

APPENDIX 1 76

LIST OF FIGURES

Figure 1 Workflow of the proposed project. 10
Figure 2 Variations of Surface and Atmospheric Temperatures. Adopted from: (EPA, 2008: 4, Fig. 2). 13
Figure 3 Factors that cause Urban Heat Island Effect. Adopted from: (Wai, et al., 2022: 2, Fig. 1). 14
Figure 4 Urban structure, cover, fabric and metabolism contribute to the UHI effect in highly developed areas; adopted from: (Soltani & Sharifi, 2017: 531, Fig. 2). 16
Figure 5 The UHI effect peaks at the clear and calm weather at winter nights. It also peaks earlier during winter Schematic representation; adopted from: (Soltani, et al., 2017: 530, Fig. 1). 17
Figure 6 The electromagnetic spectrum arranged by wavelength. Thermal infrared highlighted in bold. Adopted from: (Tomlinson, et al., 2011: 297, Fig. 1). 19
Figure 7 Requirement catalogue/requirement breakdown structure, describing needs on the project's implementation. 25
Figure 8 GEE processing chain for retrieving Landsat LST. The blue text indicates coded functions in modules. The gray text indicates GEE datasets used in the production; adopted from: (Ermida, et al., 2020: 6, Fig. 1). 29
Figure 9 Distribution of selected test sites. 31
Figure 10 Administrative boundaries of selected test sites. 32
Figure 11 LST of the urban, blue, green, cropland, and bare areas in 1990 and 2021... 38
Figure 12 LST values for all twelve cities in two different time series. Boxes indicate the inter-quartile range, red lines indicate the median, and whiskers indicate the min and max LST values. 40
Figure 13 The difference in LST values between two time series (LST2021 - LST1990) in each LC classes. 41
Figure 14 Mean LST (K) for the twelve cities in the years 1990, 2005 and 2021 assessed in this study 44
Figure 15 Spatial LC visual comparison for the twelve cities assessed in this study. 48
Figure 16 Description of area (in %) of LC statistics for twelve selected test sites in 1990 and 2021 54

List of Tables

Table 1. As the scale increases, the UHI effect gets moderated by air turbulence; adopted from: (Soltani, et al., 2017: 532, Table 1). 17
Table 2. Proportion of thermal sensors in UHI studies. Adopted from: (Zhou, et al., 2019: 7, Table 1)..... 18
Table 3. Summary of the thermal sensors most applied in UHI studies; adopted from: (Almeida, et al., 2021: 4, Table 1). 20
Table 4. Work breakdown structure, describing approach and implementation steps which needs to fulfill by requirements. 24
Table 5. Bands, GEE dataset, spatial resolution, equatorial crossing time (E.C.T.), and available date range for each Landsat satellite. Adopted from: (Ermida, et al., 2020: 3, Table 1). 26
Table 6. City classification based on the size for the study area..... 31
Table 7. Koppen-Geiger climate classifcation for the study area. 35
Table 8. Time, mission, resolution, path and row, acquisition date, sun azimuth, sensor, and cloud cover of the records of images used to extract information for Villach (Austria) as an example..... 36
Table 9. LC classifcation and defnitions are used in this study. Adapted from: (Abulibdeh, 2021: 259, Table 4). 37
Table 10. LST (K) and LC in 2021 and 1990. 39
Table 11. P-value reported from t test to represent LC relationships. 41
Table 13. Statistical analysis: mean bbe (K), mean Landsat LST (K), and mean In-situ LST (K) and variation between Landsat LST calculation and In-situ LST calculation. 43
Table 14. Summary of the LC change (in %) from the maps (1990–2021) in twelve selected test sites. 53
Table 15. Mean surface temperatures (K) for the twelve cities assessed in this study. .. 58
Table 16. The records of images used to extract information for Tehran (Iran) 76
Table 17. The records of images used to extract information for New York (US) 78
Table 18. The records of images used to extract information for Vienna (Austria) 80
Table 19. The records of images used to extract information for Washington D.C, (US) 82
Table 20. The records of images used to extract information for Helsinki (Finland) 83
Table 21. The records of images used to extract information for Quebec (Canada)..... 85
Table 22. The records of images used to extract information for Canberra (Australia) .. 87
Table 23. The records of images used to extract information for Palma (Spain) 89
Table 24. The records of images used to extract information for Latur (India) 91
Table 25. The records of images used to extract information for Niihama (Japan) 92
Table 26. The records of images used to extract information for Springfield (US) 93
Table 27. The records of images used to extract information for Villach (Austria)..... 95

CHAPTER 1

1 INTRODUCTION

1.1 MOTIVATION

Because of the increasing in the concentration of greenhouse gases (GHGs), such as water vapor, methane, ozone, carbon dioxide, chlorofluorocarbons, and nitrous oxide, global warming is defined as "the increase in the surface average temperature of the world." Without GHGs, the world's surface temperature would be too low, making it impossible for life to exist on the planet. The greenhouse effect is the primary factor that makes the earth habitable. However, the increase in GHGs in the atmosphere is what caused this disastrous phenomena, or global warming (Al-Ghussain, 2019).
Cities, which make up approximately 1% of the world's land area, use 85% of the world's resources, consume 75% of its energy, and emit around 80% of its greenhouse gas emissions (Huang, et al., 2021). By 2050, it is expected that 9.8 billion people will live in cities, up from the current level of more than 50% of the world's population. According to estimates, there will be 6.7 billion more people living in cities than in rural areas (3.1 billion) (Ritchie & Roser, 2018). Cities will experience increased environmental pressure and a conflict between the supply and demand of resources as urbanization continues (Huang, et al., 2021). Urbanization can have major influence on the local weather and climate, as is widely known and well-documented (Liu & Zhang, 2011). Living in an urban area restricts one's access to nature and can increase environmental risks like air and noise pollution, urban extreme heat exposure, and so on. Numerous urban areas are under increasing pressure due to rising population, resource scarcity, and the escalating effects of climate change (WHO, 2017). Additionally, this has increased both the degree and frequency of extreme high-temperature weather as well as the trend of global warming (Chen, et al., 2020). Physical, social, neighborhood, land-use regulation, and urban planning elements all have an impact on urban expansion, and their effects vary depending on the location and the development process (Chen, et al., 2020).
Urban regions have higher heat storage during the daytime due to increased impervious surfaces, lower albedo, and increased heat conduction and heat capacity. This phenomenon is known as the urban heat island (UHI) effect, which worsens urban air pollution and has an impact on human health (Chen, et al., 2020). Cities are currently confronting challenges with sustainable development due to the significant rise in the global mean surface temperature since the late 19th century (Chen, et al., 2006). To develop surroundings that are healthy and sustainable, these issues must be addressed (WHO, 2017). Given the ongoing changes in the global climate and the need to reduce and adapt to these changes, urban sustainability and resilience are thus more crucial than ever.
Furthermore, high temperatures put additional strain on human physiology, especially in populations that are already fragile, and increase their vulnerability to stress. Residents who reside in or relatively close a UHI region have higher health risks (Tomlinson, et al., 2011). Therefore, the UHI is a significant urban planning issue that needs monitoring as well as focused initiatives to lessen its effects (Mirzaei, et al., 2020). According to certain research, residents of UHI areas are more likely to experience infectious infections (Méndez-Lázaro, et al., 2018) as well as heat-related disorders such nervous system problems, sleeplessness, depression, and mental illnesses (Huynen, et al., 2001) (Tan, et al., 2009).
This study's purpose is to use an improved methodology to address the following questions:

- How can the spatiotemporal patterns of UHI be determined by a generic model?
- How can UHI be detected using remote sensing image-based analysis?
- What is the relationship between UHI and LC variations over various metropolitan regions according to a remote sensing image-based analysis?

- What urban planning strategies can be employed to mitigate the effects of UHI?

1.2 General Objectives

The proposed study uses remote sensing methods to detect spatiotemporal urban heat patterns. The particular objectives of this study are to:

1. Establish a thermal remote sensing system through data collection and integration, allowing for more accurate measurements of the earth's surface temperature,
2. Create a mixed-method framework (quantitative and qualitative substudy) using the data collected in objective 1 as input in order to assess the heat in cities,
3. Map Landsat LST using GEE and obtain additional urban heat data,
4. Determine how temperature distribution and LC pattern relate,
5. Apply the framework created in objective 2 in a few selected sites.

1.3 Methodological Considerations

Based on the large-scale analytic capabilities of GEE, an intuitive methodology is developed in this work to evaluate the temporal fluctuations of the UHI impacts. Figure 1 depicts the workflow that must be followed to complete the various tasks required to achieve the primary goal of the suggested research.

The first step of this research is a thorough assessment of the relevant literature with a focus on UHI, its impacts and causes, Geography Information (GI) technology to detect this issue, thermal remote sensing, and potential UHI remedies. In addition to serving as a foundation for future study, a thorough understanding of previous UHI literature is essential for developing effective UHI mitigation and adaptation methods. The limitation observed in the traditional monitoring of UHIs has been effectively addressed by the introduction of thermal remote sensing systems. The distribution characteristics of UHIs as well as the periodic and dynamic changes in urban thermal environments may be objectively and efficiently monitored using such methodologies. So, for the purpose of identifying and investigating UHI impacts, thermal remote sensing has emerged as a key approach (Tuholske, et al., 2021). Using GEE, a cloud-based platform for planetary-scale geospatial analysis, a prototype analysis model will be implemented based on a thorough requirement analysis and a conceptual workflow (Gorelick, et al., 2017). Researchers can rapidly and easily access more than thirty years of free and public data archives, including historical images and scientific datasets, enabling worldwide and extensive remote sensing applications by using a dedicated high-performance computing (HPC) infrastructure (Ravanelli, et al., 2018). Along with raw Landsat thermal data, the Earth Engine data catalog also contains land and sea surface temperature products obtained from a number of satellite sensors, including as MODIS, ASTER, and AVHRR. With the help of GEE, we can instantly process, visualize, analyze, and download a variety of global and regional climate and remote sensing data and products in real-time. Over a number of test sites, the annual median of the LST will be computed using GEE from the Landsat Top of Atmosphere Reflectance Data for each year of the temporal span between times t0 and tn. Achieving the objective of sustainable development also requires the use of fine-scale, up-to-date urban land-cover maps for urban planning, spatial governance, and sustainability assessment. To do this, it will be used Landsat, MODIS, and higher-resolution images to obtain the urban extent with less than 30 m resolution on the same test sites for times t0 and tn, respectively. This will enable the creation of fine scape maps. The evaluation of urban planning mitigation actions to lessen the impact of UHIs comes after LST estimation at selected test sites and a spatial-temporal analysis of hot islands in the city.

In order to do this, the workflow in Figure 1 provides an illustration of the general approach used in this research. In order to examine UHI's impact on population health, it is essential to first identify the areas where heat islands are existent. Therefore, satellite-based remote sensing temperature data with good adaption and high performance in LST estimation will be employed to identify the UHI's location in test sites. Second, Geodata evaluates to do some spatiotemporal analysis for detecting UHIs, visualizing the outcome, and identifying

a pattern of UHIs at selected test sites. Finally, this analysis enables an evaluation of UHI mitigation strategies through the simulation of various urban planning scenarios.

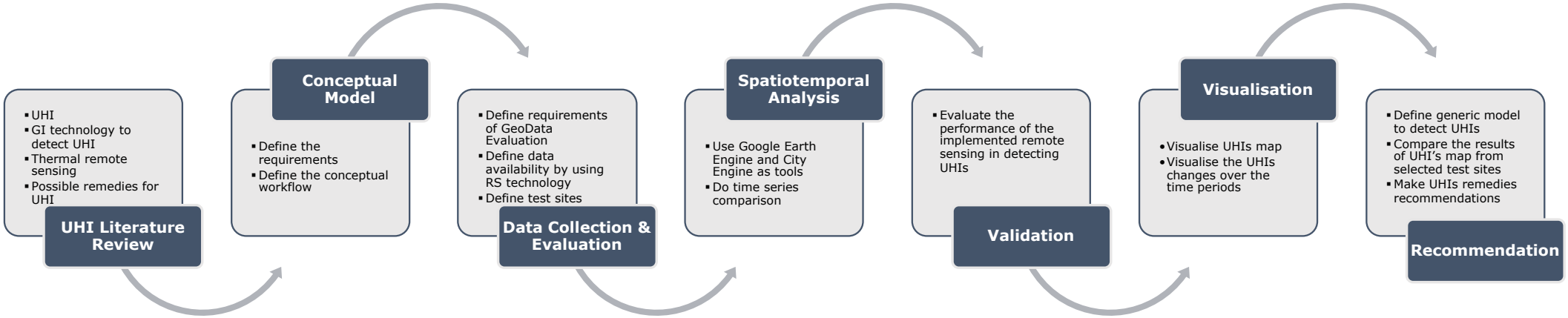

Figure 1 Workflow of the proposed project.

1.4 Relevance and Expected Results

It is expected that the suggested approach would be capable of efficiently and precisely detecting the UHI phenomena. Results show how urbanization affects the UHI magnitude with appreciable increases in LST, but they also assess the effects of various land cover types on UHI. The following is a list of anticipated outcomes:

- To develop spatiotemporal patterns for UHIs, LC changes, and available resolution of remote sensing data,
- To develop a general model for UHI detection using GEE tool.
- To compare the outcomes of different time periods at selected test sites.
- To provide practical urban spatial planning measures that will mitigate and lessen the impacts of UHI

1.5 Intended Audience and Thesis Structure

The target groups of this project are urban planners, policy makers, environmental specialists, and other groups who care about climate change and do research about its effects. This thesis with the above-mentioned research objectives is organized in 8 chapters. The next chapter covers the study of the UHI with definition, characteristics, causes and effects. Then a literature review on the criteria to mitigate UHI and the possible remedies is presented. The 3rd chapter discusses the research approach including the software tool and data which lead to creating of a conceptual model to detect UHIs. In chapter 4, the selected test sites and geo database are introduced to analyze data and validate LST estiamtes. In the following chapter, results from visualization and model performance are followed with a discussion of some issues. Finally, some short and long - term solutions are receomended for the test sites in chapter 6. The 7 and 8 chapters present the summary and possible future works and conclusion, respectively.

CHAPTER 2

2 USING REMOTE SENSING TO DETECT URBAN HEAT ISLAND (UHI) IN THE LITERATURE OVERVIEW

"Remote sensing provides global, timely, objective observations to detect UHI over time" (NASA, 2022). The major benefit of RS sensors is their continuous spatial coverage and the research area's temporal repeatability (Stathopoulou & Cartalis, 2007). Furthermore, the application of RS data/techniques onboard satellites, drones, or aircrafts allows for the determination of LST (Almeida, et al., 2021). Regarding the use of RS data for investigating UHI, the most widely employed sensors in RS in relation to the studies reviewed in this project are thermal sensors, which detect emitted and/or reflected terrestrial radiation. Thermal mapping from satellites can be used to measure LST, whilst optical data acquired from satellites can indicate where and when LC has changed over time and can be used to approximate air temperatures.

2.1 UNDERSTANDING THE CONNOTATION OF UHI

2.1.1 DEFINITION OF UHI

Heat islands, or reverse oasis areas with hotter air and surface temperatures than their rural surroundings, have long been noted in urban and suburban areas. The heat island phenomenon has been observed in cities all around the world (Gartland, 2008). This phenomenon is known as a UHI, and it has been reported since Howard. The first mention of urban heat appears in 1818, when Luke Howard's landmark research of London's climate discovered an artificial excess of heat in the city as compared to the country (Howard, 1818). During the second part of the nineteenth century, Emilien Renou made comparable discoveries about Paris, while Wilhelm Schmidt discovered similar conditions in Vienna early in the twentieth century. Heat island research in the United States began in the first half of the twentieth century (Gartland, 2008).
Heat islands grow in cities and suburbs because many typical construction materials absorb and retain more of the sun's heat than natural materials in rural areas. (Gartland, 2008) claimed that this heating is caused by two basic factors. First, because most urban building materials are impermeable and impervious, moisture is not readily available to dissipate the heat of the sun. Second, dark materials, when combined with canyon-like structure and pavement arrangements, capture and trap more of the sun's energy. During the day, dark and dry surfaces in direct sunlight may attain temperatures of up to 88°C, but vegetated surfaces with damp soil may only reach 18°C under the same conditions. Anthropogenic heat, or heat created by humans, slower wind speeds, and urban air pollution all contribute to heat island formation (Gartland, 2008).
(Oke, 1982) distinguishes three categories of UHIs:

1. Surface heat islands: Surface heat islands may be identified in a city by measuring the infrared radiation emitted and reflected by surfaces.
2. Canopy layer heat islands: The canopy layer is the layer of air between the ground and treetops, or the roofs of buildings, where most human activity occurs.
3. Boundary layer heat islands: The boundary layer is placed above the canopy layer. Air temperature is referred to this by canopy and boundary layer heat islands.

The earth's surface and the atmospheric air higher above the city have different temperatures. Because of this, the United States Environmental Protection Agency (U.S. EPA, 2008) distinguishes between two types of heat islands: surface heat islands and atmospheric heat islands. They differ in terms of how they are generated, how they are

identified and measured, how they affect things, and to some extent how they may be cooled.

1. Surface Heat Islands: Compared to most natural surfaces, urban surfaces like roads and roofs absorb and emit heat to a larger extent. Conventional roofing materials may go up to 60°F warmer than air temperatures on a hot day with a 91°F temperature. During the daytime when the sun is shining, surface heat islands frequently reach their peak intensity.
2. Atmospheric Heat Islands: These heat islands form when the air in urban areas is warmer than the air in rural areas, which is colder. The intensity of atmospheric heat islands varies significantly less than that of surface heat islands.

These differences in temperature are referred to as heat islands inside cities. Urban parks, ponds, and residential areas are cooler than downtown areas in the heat island effect diagram (Figure 2).

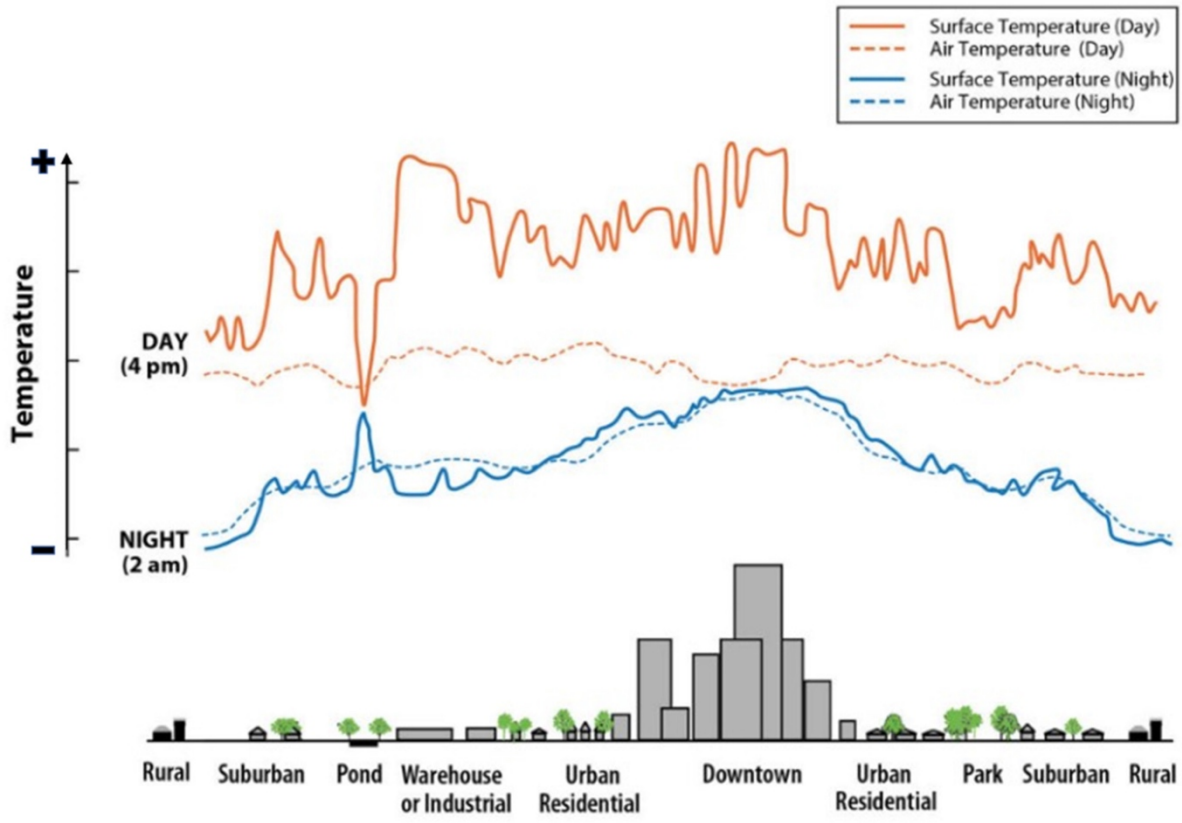

Figure 2 Variations of Surface and Atmospheric Temperatures. Adopted from: (EPA, 2008: 4, Fig. 2).

2.1.2 Characteristics of UHI

UHI characteristics and Weather patterns varies across different geographic regions (Almeida, et al., 2021). The difference in temperature between cities in relation to their surroundings is typically used to calculate heat islands. Within a city, the temperature can also change. The uneven distribution of heat-absorbing pavements and buildings makes some locations hotter than others, while trees and other vegetation keep other areas cool. (Gartland, 2008) lists the following five characteristics that describe the UHI effect:

1. Heat islands frequently become warmer compared to their rural surroundings at night and cooler before day. It is possible for urban air to be up to 6°C warmer

than rural air in the canopy layer, which is the area beneath the tops of trees and buildings.
2. Since many man-made surfaces absorb more solar heat than do natural vegetation, urban surfaces heat up and thus heats the air.
3. When the weather is calm and clear, these differences in air and surface temperatures are amplified.
4. Heat islands tend to intensify as cities get larger, and therefore tend to be hotter in areas with less greenery and more urbanization.
5. The boundary layer, a layer of air up to 2000 meters altitude, also exhibits warmer air in heat islands. Large plumes of warmer air are frequently produced by heat islands above cities, and temperature inversions (warmer air over colder air) are frequently brought on by heat islands.

2.1.3 UHI Contributing Factors

Previous research has examined the causes and elements that influence the formation of UHIs in great detail (factors affecting UHI are illustrated in Figure 3).

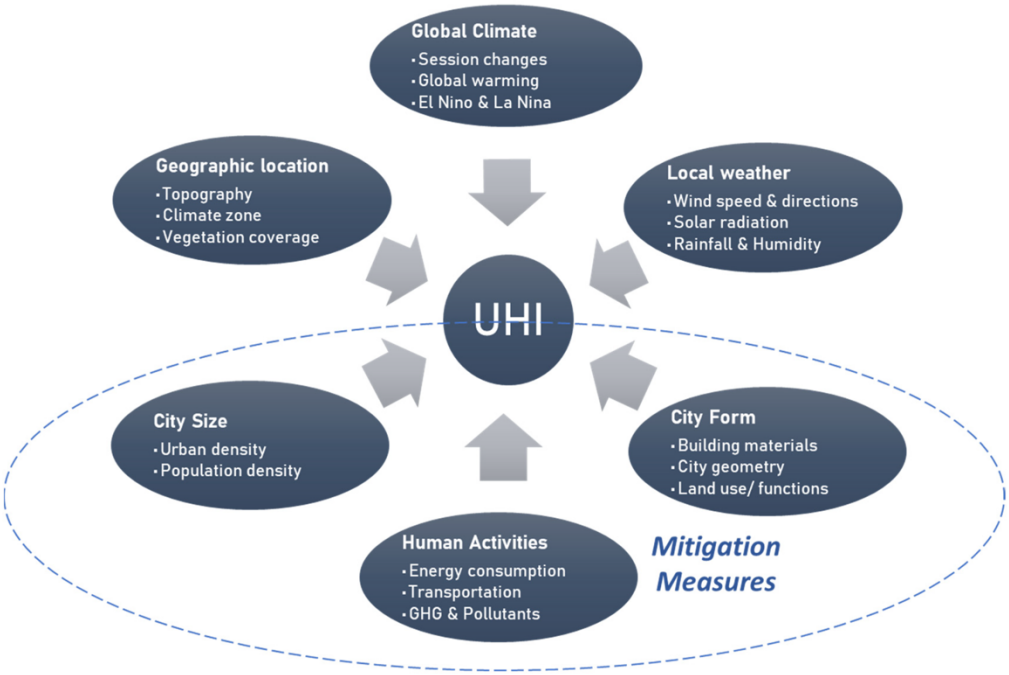

Figure 3 Factors that cause Urban Heat Island Effect. Adopted from: (Wai, et al., 2022: 2, Fig. 1).

(Oke, 2006) claims that there are four main contributing reasons to the UHI effect:
Thermal capacities, albedo coefficients, heat conductivities, and moisture levels can all vary as a result of human actions that alter natural LCs. Urban land usage can result in local air and surface temperatures that are several degrees higher than the surrounding environment's temperatures (Mirzaei, et al., 2020). Because they create changes in the physical properties of the surface (albedo, thermal capacity, heat conductivity, and moisture), as well as changes in radiative fluxes and the near surface flow, urbanization and anthropogenic activities are among the causes of UHI. These two variables are responsible for the significant replacement of soil and vegetation with pavement, building structures, and dark surfaces with urban materials (concrete, asphalt, and metal), which causes a rise in heat radiation and changes the surface energy balance, increasing LST

(Ngie, et al., 2014). Eventually, this causes the sensible heat flow to rise at the expense of the latent heat flux (Wang et al., 2007).
Due to its canyon geometry, which is characterized by narrow streets and tall buildings that block airflow, urban geometry is another important contributor to UHI. Through wind flow, geometry also influences this outcome. Wind and cloud cover are the two main meteorological factors that influence UHI development. UHIs typically develop when the winds are calm, and the sky is clear because these conditions increase the amount of solar radiation that reaches urban surfaces and reduce the amount of heat that can be convectively transported away. Strong winds, on the other hand, and cloud cover, respectively, reduce UHIs by convecting warm air away or reflecting it. The creation of UHI is influenced by topography and climate, both of which are influenced by the location of a city. Large bodies of water, for instance, can provide winds that convect heat away from towns and reduce temperatures. A city may have wind patterns that blow through it or that are blocked from reaching it by nearby mountain ranges. When larger scale factors, like prevailing wind patterns, are comparatively weak, the significance of local terrain for heat island creation increases. Large water bodies and steep terrain nearby can have an impact on local wind patterns and UHI formation (Ngie, et al., 2014).
The intensity and spatial distribution of the UHI effect are also influenced by changes in the LC pattern in response to urbanization (Chen, et al., 2006). Urban bare concrete cover, urban woods or the shade of trees, urban water areas, and urban lawn were chosen as the four types of LC to study their microclimate, and the UHI was also analyzed using air temperature data measured at four fixed observation spots in Nanjing, China (Huang, et al., 2008). This demonstrates how various land uses have distinct effects on UHI.
In addition, (Oke, 2006) claimed that the UHI effect was mostly caused by urban structure, surface cover, urban fabric, and metabolism.

- **Urban structure**, which modifies the balance of heat exchange in the built environment by influencing shadow and wind patterns. It has an impact on the amount of sunlight that materials are exposed to and the subsequent heat storage in thermal mass. The strength and patterns of airflow in urban canyons can also be altered by this complex heat radiation exchange between the atmosphere around and the building mass.
- **Urban cover and surface materials**, which have an impact on the rate of heat absorption and reflection in the built environment. The heat flux in outdoor spaces can be altered in factors are variables by the thermodynamic specification, color, texture, and density of materials, as well as their exposure to sunlight.
- **Urban fabric**, which has a greater impact on the built environment's water and heat exchange balance than its natural surrounds. The processes of photosynthesis and evaporation in urban vegetation help to lower the air temperature. Lower atmospheric air turbulence is also influenced by the type, distribution, and intensity of urban vegetation.
- **Urban metabolism** and anthropogenic waste heat in cities, which are mostly associated with the amount of energy consumed for motorized transportation and indoor air conditioning (see Figure 4).

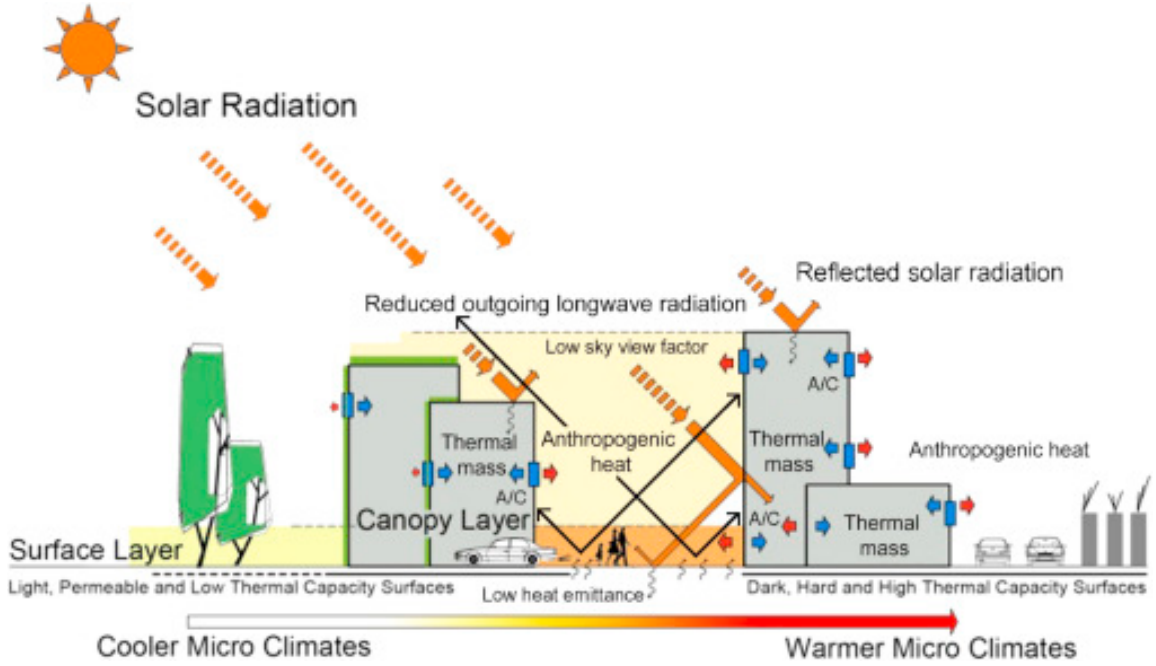

Figure 4 Urban structure, cover, fabric and metabolism contribute to the UHI effect in highly developed areas; adopted from: (Soltani & Sharifi, 2017: 531, Fig. 2).

2.1.4 UHI Effect

The UHI effect and its effects are projected to be increasingly severe in a world that is rapidly urbanizing and experiencing a warming climate (Zhou, et al., 2019). The effects of this phenomena that are the most regressive are:

- Influence on the local microclimate,
- Thermal discomfort
- Impacts on public health
- Changes in hydrological behavior, with a displacement of water masses, for instance.

UHI can have a greater negative influence on human health when paired with natural occurrences like heat waves, which can lead to an increase in mortality. Most likely, climate change will lead to an increase in air temperatures, amplifying the harmful consequences of UHI (Almeida, et al., 2021).

Due to meteorological, geographical, and urban characteristics, the extent of the temperature differential changes throughout time and place (Kleerekopera, et al., 2012). The heat island effect is frequently evaluated by the difference in air temperatures between urban and rural areas, sometimes known as the strength or intensity of the heat island. This level of intensity changes throughout the day and night. The difference in temperature between urban and rural areas is typically the smallest in the morning and increases during the day as urban surfaces heat up and warm the urban air. Since urban surfaces continue to contribute to the high and slow the process of nighttime cooling, the heat island's intensity is typically highest at night (Gartland, 2008).

Figure 5 shows the air temperature and heat island intensity for typical summer and winter days in a heat island. Due to the solar gain of urban surface materials, the urban-rural temperature differential begins to grow throughout the daytime under a clear sky. Warm air is retained in the built environment for a longer period of time when the weather is calm (Soltani & Sharifi, 2017).

Moreover, negative impacts of UHI have a hugely broad range of effects on many people. The UHI has influenced a veriety of environmental changes, including regional temperature, vegetation growth, and water and air quality. These variables, in turn, have

a significant impact on human health and wellbeing and have the potential to raise illness and mortality, energy consumption, and even violent incidents in urban areas, where 55% of the world's population currently reside (Zhou, et al., 2019).

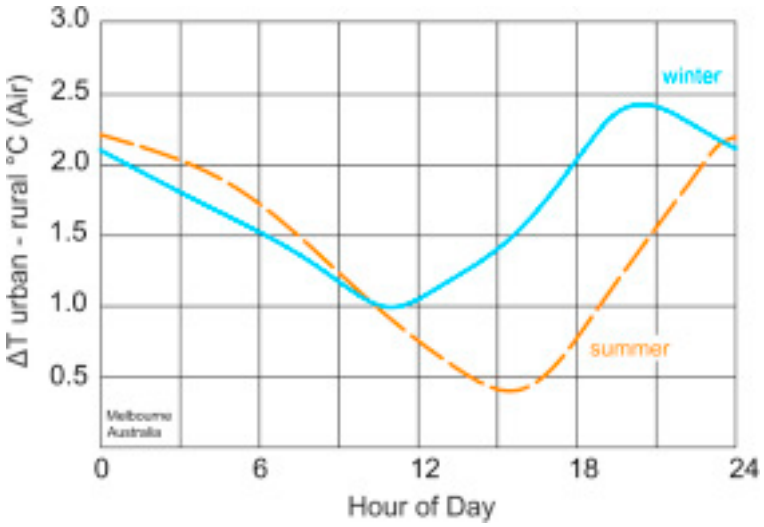

Figure 5 The UHI effect peaks at the clear and calm weather at winter nights. It also peaks earlier during winter Schematic representation; adopted from: (Soltani, et al., 2017: 530, Fig. 1).

2.1.5 UHI Metrics

(Oke, 2006) represented UHIs in three different scales:

- Urban surface material scale (surface layer),
- Building and public space scale (canopy layer),
- City scale (boundary layer).

The thermal behavior of surface materials and their exposure to solar radiation have a significant impact on the UHI effect. The air temperature above urban surfaces are impacted by the heat that is emitted from urban surfaces and is mixed by convection. Urban canopy layer is the region of the city that is bounded by surface cover and building skylines. Heat accumulation in the canopy layer is influenced by the geometry and orientation of open spaces, aspect ratio (height to width), sky view factor (the fraction of the sky visible from the ground up), LC material (asphalt, hard-landscapes, grass cover, water, tree, etc.), and wind flow (Soltani & Sharifi, 2017).
As the geographic scale is enlarged, temperature differences become less, as seen in Table 1. It is more probable to notice temperature differences between a building's north and south sides than between two separate land uses in a precinct (building block versus park).

Table 1. As the scale increases, the UHI effect gets moderated by air turbulence; adopted from: (Soltani, et al., 2017: 532, Table 1).

Scale	layer	Focused temperature	Focused elements	Dimension range (approximate)
Micro	Surface	Surface temperature	Open Space skin	1–10 m
			Building rooftops	
			Building facades	
Local	Canopy	Air temperature	Spaces between buildings	$10–10^3$ m
			Public spaces	
			Streetscapes	
			Urban precincts	
Macro	Boundary	Surface and air temperature	Land use classes	$10^3–10^5$ m
			Citywide	

2.2 GI Technology to Detect UHI

"Remote sensing technology is an important source of Earth observation from different platforms and sensors, and it offers work on a large scale with cheap, accurate (depending on the research design), and faster results compared to the conventional methods" (Sekertekin & Bonafoni, 2020). P. Krishna Rao, a research physical scientist of the National Environmental Satellite Service (NESS) of the National Oceanic and Atmospheric Administration (NOAA), launched the satellite remote sensing era of UHI investigations in 1972 (Zhou, et al., 2019). While surface temperatures have a slight but considerable indirect impact on air temperatures, they, both, can be used to identify UHIs (Almeida, et al., 2021). Therefore, there are different amounts and types of sensors used to measure UHI. The percentage of investigations using various sensors or satellite images is shown in Table 2 for the reviewed studies. Since the sensors are passive, they can detect and quantify both shortwave radiations reflected back from the Earth's surface and atmosphere (non-thermal spectral bands) and longwave radiation emitted by it (thermal spectral bands). This is crucial for UHI investigations because determining the relationship between two important parameters, such as a region's LST intensity and the underlying LC composition and configuration that are connected, is a foundational step in understanding the causes of UHI (Zhou, et al., 2019).

Table 2. Proportion of thermal sensors in UHI studies. Adopted from: (Zhou, et al., 2019: 7, Table 1).

Sensor	Landsat Series	MODIS	ASTER	Multiple Sensors	AVHRR	Others
Proportion	53%	25%	7%	6%	4%	5%

There are various methods for evaluating the thermal behavior of a site, including remote sensing, information from stationary weather stations, information from authorized sources, in-situ campaigns using portable thermal cameras, etc. S ome studies use multiple data sources from the list above to supplement the information, both at the atmospheric and surface levels (Almeida, et al., 2021). Over the last few decades have seen a significant increase in the quantity and quality of UHI studies due to developments in remote sensing and spatial science (Zhou, et al., 2019).
The LST, a relevant variable that can be used to determine the radiative load of the earth's surface, can be calculated from the remote sensing data. The LST, also known as skin temperature or radiometric temperature, refers to the precise measurement of the earth's surface temperature. Unlike measurements made by meteorological stations that record the temperature close to the surface, the LST allows for a more detailed scale of analysis: in areas of dense vegetation, it will represent the temperature of the canopy's leaves; in areas of sparse vegetation, it will correspond to the entire canopy, subsurface, and ground surface; and on the bare ground, it will represent the temperature of the top (few micrometers) from the ground s surface. In addition, LST can be employed to retrieve important climatic variables as evapotranspiration, water-stressed vegetation, soil moisture, and thermal inertia. It has a wide range of applications and is useful in UHI research, global warming, cryosphere melting, insect infestation, vector-borne diseases, etc (Almeida, et al., 2021). In regards of using remote sensing data for UHI research, thermal sensors—which identify emitted and/or reflected terrestrial radiation—are the most often employed remote sensing sensors. Using thermal sensors can be difficult, especially when clouds are present. This might have an impact on the validity of the data and the temporal analysis of the chosen sites (Almeida, et al., 2021).

2.2.1 Thermal Sensors

One of the areas of study of remote sensing known as "thermal remote sensing" focuses on the collection, analysis, and interpretation of data mainly from the Thermal Infrared (TIR) portion of the electromagnetic spectrum. To measure the surface temperature,

thermal remote sensing collects the radiation emitted by the ground. The other important biophysical parameters derived from TIR data are surface emissivity, soil moisture, and evapotranspiration in addition to surface temperature. Since these variables control energy flows and interactions between the atmosphere and the land, it is crucial to accurately estimate them in order to comprehend how the Earth behaves (Sekertekin & Bonafoni, 2020).

The thermal-infrared (TIR) region is the range of electromagnetic wavelengths between 3 and 35 µm. This range's useable spectral bands are limited by the intensity of radiation and atmospheric windows (Ngie, et al., 2014). Thermal sensors operate in the 8–15 µm range (Almeida, et al., 2021), in which most remote sensors are set up to detect the thermal radiative properties of the ground materials (Ngie, et al., 2014). The radiation is translated into temperature data after being recorded as a Digital Number (DN) (Almeida, et al., 2021). So, the thermal infrared (TIR), which ranges in wavelength from 8 to 15 µm, is therefore the most useful wavelength for LST measurements within the EMR spectrum (Figure 6) (Tomlinson, et al., 2011).

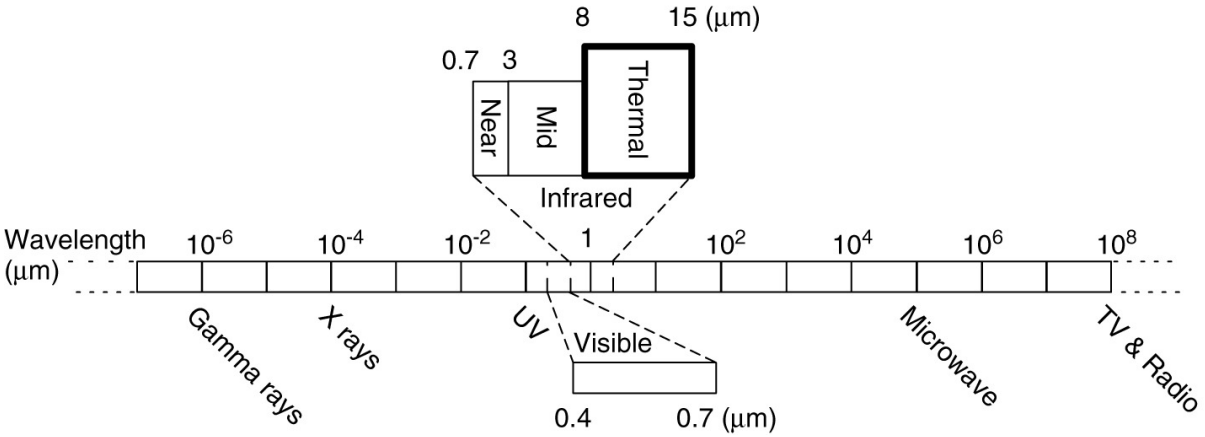

Figure 6 The electromagnetic spectrum arranged by wavelength. Thermal infrared highlighted in bold. Adopted from: (Tomlinson, et al., 2011: 297, Fig. 1).

The ability and sensitivity of each sensor to provide data within the electromagnetic spectrum, which includes both visible and non-visible zones, is determined by its spectral resolution. In practice, the sensors are cooled to near-zero degrees so that their eventual emissions do not affect the targets' measurements and temperature records (Almeida, et al., 2021).

According to Table 3, Landsat, Moderate Resolution Imaging Spectroradiometer (MODIS), and Advanced Spaceborne Thermal Emission and Reflection Radiometer (ASTER) are the thermal sensors most often used in UHI investigations. Different geographical resolution and temporal coverage data from the available satellite TIR sensors may be used to derive LST. While the National Oceanic and Atmospheric Administration (NOAA), Advanced Very High-Resolution Radiometer (AVHRR), and Terra and Aqua Moderate Resolution Imaging Spectroradiometer (MODIS) have 1-km spatial resolutions, the Geostationary Operational Environmental Satellite (GOES) has a 4-km resolution in the TIR. In comparison to Landsat-5 Thematic Mapper (TM), which has a spatial resolution of 120 m, and Landsat-7 ETM+, which has a resolution of 60 m in the TIR bands, the Terra-Advanced Space-borne Thermal Emission and Reflection Radiometer (ASTER), which has a spatial resolution of 90 m, provides significantly better data. The spatial variation within coarser-resolution observations produced by MODIS and AVHRR, which provide more frequent measurements, may be explained using Landsat's better resolution and less frequent TIR observations. Recent satellite systems, like as MODIS and ASTER, have features that make calibration simpler and offer LST as standard products. This is not true for the Landsat data (Almeida, et al., 2021).

Table 3. Summary of the thermal sensors most applied in UHI studies; adopted from: (Almeida, et al., 2021: 4, Table 1).

Sensor	Satellite Platform	Orbital Frequency	Spatial Resolution	Spectral Bands (μm)	Number Band	Data Available Since
AATSR	Envisat	35 days	1 km (approx.)	11 and 12	TIR	2002–2012
ASTER	Terra	Twice daily	90 m	8.125–8.475 8.475–8.825 8.925–9.275 10.25–10.95 10.95–11.65	10 11 12 13 14	1999
AVHRR (Advanced Very High Resolution Radiometer)	NOAA 6, 8 10, TIROS-N	Twice daily	1.1 km (approx.)	10.3–11.3 11.5–12.5	4 5	1978–2001
AVHRR/2 (Advanced Very High Resolution Radiometer/2)	NOAA 7, 9, 11, 12, 13, 14	Twice daily	1.1 km (approx.)	10.3–11.3 11.5–12.5	4 5	1981–2007
AVHRR/3 (Advanced Very High Resolution Radiometer)	METOP-A, B, C	29 days	1.1 km (approx.)	10.3–11.3 11.5–12.5	4 5	2006
AVHRR/3 (Advanced Very High Resolution Radiometer/3)	NOAA 15, 16, 17, 18, 19	Twice daily	1.1 km (approx.)	10.3–11.3 11.5–12.5	4 5	1998
ETM+	Landsat 7	16 days	60 m (resampled to 30 m)	10.4–12.5	6	1999
GOES Imager	GOES	Geostationary	4 km (approx.)	10.2–11.2 11.5–12.5	TIR	1974
IRMSS (Infrared Multispectral Scanner)	HJ-1B	31 days	300 m	10.5–12.5	TIR	2008–2018
IRMSS (Infrared Multispectral Scanner)	CBERS 1	26 days	160 m	10.4–12.5	4	1999–2003
IRMSS (Infrared Multispectral Scanner)	CBERS 2	26 days	160 m	10.4–12.5	4	2003–2009
IRMSS (Infrared Multispectral Scanner)	CBERS 2B	26 days	160 m	10.4–12.5	4	2007–2010
IRMSS-2 (HJ) (Infrared Multispectral Scanner-2)	HJ-2A and HJ-2B	4 days	300 m	10.5–12.5	TIR	2020
IRS (Infrared Medium Resolution Scanner)	CBERS 4	26 days	80 m	10.4–12.5	12	2014

IRS (Infrared Medium Resolution Scanner)	CBERS 4A	31 days	80 m	10.4–12.5	12	2019
MODIS	Terra	Twice daily	1 km (approx.)	10.78–11.28 11.77–12.27	31 32	1999
MODIS	Aqua	Twice daily	1 km (approx.)	10.78–11.28 11.77–12.27	31 32	2002
SEVIRI	Meteosat-8	Geostationary	3 km (approx.)	10.812	TIR	2005
TIRS	Landsat 8	16 days	Collected at 100 m and resampled to 30 m	10.6–11.2 11.5–12.5	TIR	2013
TIRS 2	Landsat 9	16 days	Collected at 100 m and resampled to 30 m	Similar TIRS	Similar TIRS	available from USGS in early 2022
TM	Landsat 4	16 days	Collected at 120 m and resampled to 30 m	10.4–12.5	6	1982–1993
TM	Landsat 5	16 days	Collected at 120 m and resampled to 30 m	10.4–12.5	6	1984–2011

2.2.2 Classification of Thermal Sensors

UHI is defined along space (urban/rural boundaries) so spatial resolution considers for classification of sensors. According to (Almeida, et al., 2021) the classification of these sensors according to the coarseness or fineness of a raster grid is what characterizes spatial resolution.

- **High resolution:** Thermal sensors are categorized as having a spatial resolution of 60 m. One of the most used sensors in this group for UHI investigations is Landsat. This is due to its readily available, high-quality multispectral data with global coverage for historical and multitemporal data.
- **Medium resolution:** 90 meters are thought to be the minimum spatial resolution for medium resolution. It is significant that the Terra-Advanced Space-borne Thermal Emission and Reflection Radiometer (ASTER), which has a 90 m spatial resolution, provides the medium-resolution data. In this category of sensors, it is one of the most often employed for UHI research.
- **Low resolution:** These sensors have a 250 m to 1 km spatial resolution range. The most common example of this type of data-generating instrument is MODIS. Given its spatial resolution, which extends from 250 to 1000 m, MODIS is ideally suited for UHI research across wide scene regions. Bands 24 (4.433-4.498 mm) and 25 in MODIS' hyperspectral range, which consists of 36 bands in total, cover the air temperature (4.482–4.549 mm). Since it concurrently collects data in four bands with a spatial resolution of 1.1 km in the VNIR and TIR regions of the spectrum, the NOAA AVHRR on board is another sensor being employed for UHI exploration.

As MODIS is a low-resolution sensor, it has been employed over large regions, but Landsat and ASTER are better suited for studying specific cities or smaller areas due to its medium resolution (Kaplan, et al., 2018).

2.3 Possible Remedies for UHI

In order to address the negative consequences of the UHI phenomena, local authorities throughout the world are using a variety of mitigation strategies and standards.

2.3.1 Existing UHI Mitigation Strategies

Criteria for mitigating the effects of UHI are included in major assessment methodologies like the Building Research Establishment Environmental Assessment Methodology (BREEAM), Leadership in Energy and Environmental Design (LEED), Comprehensive Assessment System for Built Environment Efficiency (CASBEE) and Building Environmental Assessment Method (BEAM).
There have been several attempts to produce catalogues suggesting mitigation strategies:

- In Quebec, the catalogue of UHI mitigation options (Giguère, et al., 2009) classifies the mitigation measures into four categories: vegetation, sustainable urban infrastructure, sustainable stormwater management, and reduction of anthropogenic heat.
- The mitigating strategies are also categorized by scale (building and urban planning). Building mitigation strategies are divided into three categories: solar radiation protection, heat infiltration minimization, anthropogenic heat reduction, and maintaining a comfortable thermal environment. In contrast, urban planning and development strategies are divided into three categories: greening, urban infrastructure, and anthropogenic heat reduction. This catalogue comprises short term mitigation measures such as ensuring the access to the so called "cooling centers" which are any airconditioned public buildings that can accommodate public (shopping centers, schools, cultural centers...), the creation of air-conditioned shelters for outdoor workers or even the access to aquatic facilities (including pools and misters) in natural environment or public installations (Filho, et al., 2017).
- The catalog was created by (Vienna University of Technology, 2014) as part of the UHI project of the Central Europe Program, which was co-financed by the ERDF and divided the actions into four packages: buildings, pavements, vegetation, and street morphology.
- Its classification does not organize the mitigation actions by the immediacy of its effect (short-, medium- or long-term effect), and in turn in its introduction a clear distinction is made between adaptation measures and mitigation measures. Adaptation measures are considered measures where the direct intervention of users is necessary, clothing, air conditioning, and that do not have any positive effect on the outdoor thermal comfort, or even that have a negative one, heat released by air conditioning. In turn, the mitigation strategies are considered well prepared and consistently applied actions. This is the reason why the mitigation measures presented include less actions than other catalogues (Filho, et al., 2017).
- The (Yamamoto, 2006) study organizes the mitigation strategies in three categories: reduction of anthropogenic heat release, improvement of artificial surface covers, improvement of urban structure.

Although the layout of the catalogues differs, there is agreement about the nature of the UHI mitigation measures, according to the assessment of the aforementioned catalogues by (Filho, et al., 2017). Different mitigation actions can be categorized according to the scale of UHI studies which are mentioned below:

- **At building scale:** choice of roofing materials, change the black roofs into green roofs, and reduction of anthropogenic heat production, the use of geothermal energy and radiant cooling systems, are alternative solutions to conventional air conditioning systems.
- **At city scale:** More urban green vegetation which provides shade, thermal insulation to keep the interior cool, manage noise and air pollution (Roth, 2013), replacing pavement materials with new surface cover, urban structure by designing buildings with considering wind properties. Moreover, at city scale, anthropogenic

heat is produced either by buildings or by cars. Several measures can help reduce traffic anthropogenic: greener cars, improving public transit, reducing sprawl, increasing mixed-used development and by encouraging the use of electro-mobility.

- **At regional scale:** the European Environment Agency urban adaptation document ((EEA), 2012) suggests interventions to reinforce green infrastructure outside the city boundaries in order to manage the three main climate change phenomena threatening cities: heat waves, floods and droughts, which are projected to increase in frequency, intensity and duration. Furthermore, land use should be taken into consideration according to the average night-time LST of different land use patches which varies depending on the size, shape, and nature of the land use (forests, cropland, grassland, water surfaces, built areas and greenhouse areas). Other strategies in this level are catering for wind corridors (Echevarria, et al., 2016) and using the ecological functions of water bodies (Hendel, et al., 2016).

2.3.2 Criteria to Mitigate UHI Phenomenon

The criteria for mitigating the effects of UHI are included in major assessment methods like the Building Research Establishment Environmental Assessment Methodology (BREEAM), Leadership in Energy and Environmental Design (LEED), Comprehensive Assessment System for Built Environment Efficiency (CASBEE) and Building Environmental Assessment Method (BEAM). The largest number of UHI parameters belongs to CASBEE, with three toolkits: CASBEE for Urban Development, CASBEE for Home (Detached House), CASBEE for New Construction (O'Malley, et al., 2014). Although the criteria are represented differently by each of the aforementioned assessment techniques, there is agreement on the assessment criteria for all techniques, which can be summed up as follows: air circulation or passage, shading of buildings, the presence of greenery or roofs, the use of water, and external use of high-albedo materials on buildings' surfaces. Therefore, according to (Monsefi, et al., 2015), the following criteria to control UHI might be investigated (Monsefi, et al., 2015):

- **H/W ratio:** The ratio between the building height and street width is a prominent factor and effective on thermal comfort, especially in tropical climates.
- **Orientation:** Considering thermal comfort, the orientation of the street network in relation to the patterns of sun movement and prevailing winds is an important issue.
- **Reflectivity:** Varying materials used for the surface of the wall, street, and building roof that reflect light differently can have different impacts on warming the environment.
- **Conductivity:** The characteristics of the materials utilized in urban areas directly affect the regional microclimate. It is essential to look at the connection between thermal conductivity and people's comfort levels in the heat of the outdoors.
- **Plot coverage:** There are certain limitations for the location of a building within its land plot and the percentage of the plot that it covers.
- **Balconies:** The primary method for enhancing outdoor thermal comfort is the provision of shade. This may be accomplished by installing structures like balconies, colonnades, pergolas, and other things that cast shadows over public areas, particularly pedestrian routes.
- **Vegetation:** In the world of outdoor thermal comfort and reducing UHI, vegetation and green infrastructure of a city have also been mentioned as important elements (Monsefi, et al., 2015).

CHAPTER 3

3 UHI DETECTION APPROACH

3.1 DATA REQUIREMENTS FOR DETECTING UHIS

There are two categories within the requirements for UHI detection. requirements for the program used, as well as for the data/map used for UHI detection. The precise data must be identified in order to detect UHIs. These specifications include identifying the temperature sensors, establishing time frames, and choosing test locations. The functions and methods of the application/software are relevant to the needs to demonstrate UHI maps. A requirement catalogue or requirement breakdown structure contains a summary of the needs (Figure 7).
The two requirements also concentrate on the test locations and durations that are depicted in the work breakdown table (Table 4).

Table 4. Work breakdown structure, describing approach and implementation steps which needs to fulfill by requirements.

Level 1	Level 2	Level 3
Detecting UHIs by using remote sensing technique	1 Approach	1.1 Define the conceptual model 1.2 Define requirements (data requirement) 1.3 Use Google Earth Engine as a tool (software requirement)
	2 Implementation	2.1 Define test sites according to the resolution of satellite 2.2 Define requirements of Geodata evaluation 2.3 Define data availability by using remote sensing technology 2.4 Select time periods 2.5 Setup the model

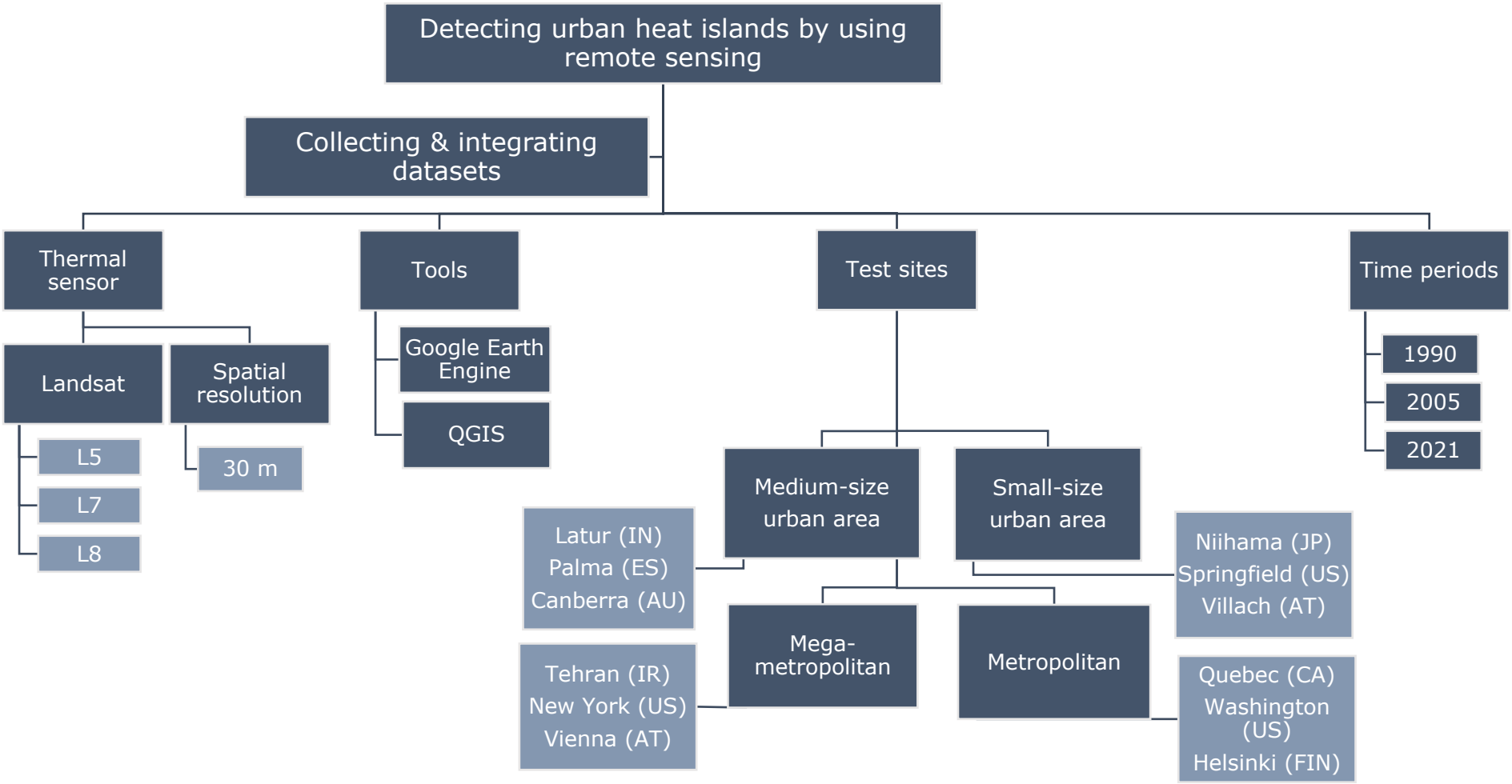

Figure 7 Requirement catalogue/requirement breakdown structure, describing needs on the project's implementation.

3.2 Software Employed_ Google Earth Engine (GEE)

The focus of the two criteria is also on the locations and lengths of the tests as shown in the work breakdown table.
Due to the use of big data and the cloud platform, global urban land mapping has significantly advanced toward finer-scale and higher spatiotemporal resolutions; for instance, GEE significantly increases the data-processing capacity (Kuang, et al., 2021). GEE is an online platform designed to make it simple for users of remote sensing to carry out large data analytics without having to download any data (Ermida, et al., 2020). In other words, GEE is a website that offers access to cloud computing, global time-series satellite images, vector data, and software and methods for processing such data (Gorelick, et al., 2017). The data repository has more than 40 years' worth of satellite images for the whole planet, as well as a sizable collection of daily and sub-daily data. Many sites also include two-week repeat data for the entire time period. The data is derived from a variety of satellites, including the entire Landsat series, Moderate Resolution Imaging Spectrometer (MODIS), National Oceanographic and Atmospheric Administration Advanced very high-resolution radiometer (NOAA AVHRR), Sentinel 1, 2, and 3, Advanced Land Observing Satellite (ALOS), and others (the most popular thermal sensors in UHI's studies with highest resolution are listed in Table 3).
For local and small-scale research, the Landsat series of satellites have the capacity to offer LST estimations at a high geographic resolution. GEE has direct access to all Landsat Level-1 and Level-2 data, including surface reflectance (SR) and top-of-atmosphere (TOA) data (Ermida, et al., 2020).

3.3 Deriving Criteria for Assessment of Land Surface Temperature Measurement

TOA brightness temperatures (BT), surface reflectance (SR), total column water vapor (TCWV), and correction of surface emissivity by NDVI are the four key factors used to extract LST.
This study loaded and computed these criteria using Landsat data. Table 5 describes the spectral band characteristics for each Landsat.

Table 5. Bands, GEE dataset, spatial resolution, equatorial crossing time (E.C.T.), and available date range for each Landsat satellite. Adopted from: (Ermida, et al., 2020: 3, Table 1).

Satellite	Used Bands	Wavelength (μm)	Dataset	Spatial Resolution	E.C.T.	Date Range
Landsat 4 (TM)	Red: B3 NIR: B4 TIR: B6	0.63–0.69 0.76–0.90 10.4–12.5	C01/T1_SR C01/T1_SR C01/T1_TOA	30 m 30 m 120[2] m	9:45 am (16-day)	22 August 1982 to 14 December 1993
Landsat 5 (TM)	Red: B3 NIR: B4 TIR: B6	0.63–0.69 0.76–0.90 10.4–12.5	C01/T1_SR C01/T1_SR C01/T1_TOA	30 m 30 m 120[2] m	9:45 am (16-day)	1 January 1984 to 5 May 2012
Landsat 7 (ETM+)	Red: B3 NIR: B4 TIR: B6[1]	0.63–0.69 0.77–0.90 10.4–12.5	C01/T1_SR C01/T1_SR C01/T1_TOA	30 m 30 m 60[2] m	10:00 am (16-day)	1 January1999 to present
Landsat 8 (OLI; TIRS)	Red: B4 NIR: B5 TIR: B10	0.64–0.67 0.85–0.88 10.6–11.19	C01/T1_SR C01/T1_SR C01/T1_TOA	30 m 30 m 100[2] m	10:00 am (16-day)	11 April 2013 to present

Note: [1] low gain band (B6_VCID_1); [2] resampled to 30 m.

3.3.1 Landsat Data

The spatial resolution of all TIR bands has been resampled to 30 m. The Normalized Difference Vegetation Index (NDVI), which is derived from the SR data, is also derived from the red and near-infrared (NIR) bands in addition to the TIR band (instead of the TOA values, which is less accurate). Thematic Mapper (TM) sensors are used by Landsat-4, Landsat-5, and Landsat-7 to acquire data in the visible and infrared spectral areas, while Enhanced Thematic Mapper Plus (ETM+), an upgraded version of the TM, is used by Landsat-7. For Landsat-8, the Thermal Infrared Sensor (TIRS) provides the TIR data while the Operational Land Imager (OLI) collects data in the visible and short-wave infrared spectrum (Ermida, et al., 2020).
The United States Geological Survey (USGS) provides TOA brightness temperatures for the Landsat thermal infrared (TIR) channels, which are accessible in GEE for Landsats-5,7, and 8, collection 2.
The USGS has made the SR data for each Landsat accessible in GEE as well. The Land Surface Reflectance Code (LaSRC) technique is used to create the SR data from Landsat-8. It does atmospheric correction using a radiative transfer model, supplementary atmospheric data from MODIS, and aerosol inversion tests using the coastal aerosol band (Ermida, et al., 2020). The Landsat Ecosystem Disturbance Adaptive Processing System (LEDAPS) method, which computes the radiative transfer for atmospheric data from MODIS and the National Center for Environmental Prediction (NCEP), is used to estimate SRs for Landsat-4 to 7 (Ermida, et al., 2020).
Additionally, the quality assessment band (BQA), which is also made available by the USGS through GEE, can be used to acquire information about cloud coverage, including cloud shadowing (Ermida, et al., 2020).

3.3.2 Total Column Water Vapor Data

In order to account accurately atmospheric contributions in the TIR measurements, information on the water vapor concentration of the atmosphere is needed. On GEE, you may find TCWV values using reanalysis data from NCEP and the National Center for Atmospheric Research (NCAR). Currently, the only global TCWV dataset on GEE that spans the entire Landsat series' operational life is the NCEP/NCAR reanalysis. The TCWV data have a six-hourly temporal resolution and a spatial resolution of 2.5 degrees, and they are accessible globally from 1948 to the present (Ermida, et al., 2020).

3.3.3 Surface Emissivity

In this investigation, the GEE codes that were just recently developed by (Ermida, et al., 2020) to recover LST were employed to compute the surface emissivity. The ASTER Global Emissivity Dataset (ASTER GEDv3), created by JPL, is included in this code.
This dataset, which was obtained using a Temperature-Emissivity Separation (TES) technique from all clear-sky ASTER photos, contains the emissivity for the five ASTER bands in the TIR region. The reported precision of the emissivity data is 0.01, and it has a spatial resolution of 100×100 m2 (Ermida, et al., 2020).
This code makes a vegetation correction using mean ASTER GEDv3 NDVI and Landsat-derived NDVI, which is frequently used to calculate surface emissivity by calculating the proportion of vegetation cover (FVC). More information is available in (Ermida, et al., 2020).

3.3.4 Retrieval of Land Surface Temperature (LST)

commonly known as skin temperature, is the temperature of the Earth's surface (Martin, et al., 2019). Applications of LST data sets in climate research are numerous. Improved knowledge of the climatic impacts of changing land use and LC, monitoring of droughts,

LC and energy balance changes, heatwave monitoring, estimation of evapotranspiration, examinations of UHIs, and daily cycles of UHIs are some examples of this (Martin, et al., 2019). LST is one of the crucial variables that affects surface energy balance, regional climates, heat fluxes, and energy exchanges. It is the radiative temperature of any land surface, including soil, grass, pavements, asphalt, and building roofs. Numerous researchers have looked at the significance of LST and its effects on a variety of subjects, such as urban climate and Surface Heat Island (SHI) studies, evapotranspiration, monitoring of forest fires, geological study, and geothermal studies (Sekertekin & Bonafoni, 2020), (Alahmad, et al., 2020). In order to assess land surface conditions, high-resolution satellite derived LST is increasingly used in a variety of applications. These applications include mapping the extent of urbanization and the intensity of urban microclimates, estimating high-resolution evapotranspiration for the management of water resources, and determining the stress of vegetation (Ermida, et al., 2020). So, from radiance readings taken by meteorological stations, LST can be approximated. However, because it is a point-based measurement, this method typically does not permit a large-scale monitoring. Additionally, not all-weather stations continuously produce data. These factors have led to the adoption of remotely sensed data for UHI analysis in numerous research. (Wang, et al., 2016). LSTs are usually measured by remote sensing techniques that retrieve satellite thermal infrared data (Alahmad, et al., 2020).

Thermal energy is emitted in wavelengths from all surfaces. These wavelengths can be recognized and measured by equipment on satellites and by other remote sensing techniques, which can then be used to determine temperature. Thus, measurements of the energy reflected and emitted from the land surface, including roofs, pavements, vegetation, bare ground, and water, can be obtained from satellite photos. It is simple to gather a large number of surface observations using radiometers placed on an aircraft or a satellite (Ngie, et al., 2014). For instance, heat islands can be located using Landsat satellite data [Enhanced Thematic Mapper plus (ETM+) band 6 for LST].

As a result of the equipment's preference for observing emissions from horizontal surfaces like streets, rooftops, and treetops, surface measurements made by remote sensing have some limitations. For example, they do not completely capture radiant emissions from vertical surfaces like a building's wall. In addition, since wavelengths travel from the sun to the earth as well as from the earth to the atmosphere, remotely sensed data represent radiation that has passed through the atmosphere twice. In order to predict surface attributes like temperature and solar reflectance accurately, the data must be rectified. Remotely sensed temperature readings, however, offer a broader regional coverage and greater temporal resolution (Ngie, et al., 2014). This study has investigated the spatial distribution of LST at a few chosen test sites using historical satellite data on daytime and nighttime LST.

3.3.5 Conceptual Model of Land Surface Temperature Estimation

The algorithm developed by (Ermida, et al., 2020) is used to extract the Landsat LST data and define fine-scale spatiotemporal trends in UHI studies. This approach is used to rebuild the LST time-series. LST data is specifically derived from scenes acquired by Landsat-5, 7, and 8, which have spatial resolutions of 120, 60, and 100 m, respectively.

The statistical mono-window (SMW) algorithm, built on the GEE platform, is used by the Landsat LSTs (Gorelick, et al., 2017). To guarantee consistency of the recovered LSTs among satellites, this mono-window technique uses an identical calibration database. It is decided to use the method proposed by (Ermida, et al., 2020) to derive the Landsat LSTs rather than the LST products offered by the United States Geological Survey (USGS). Because we could efficiently perform the analysis on the GEE platform and the Root Mean Square Error (RMSE) of the LSTs estimated by this method has been demonstrated with an acceptable Root Mean Square Error (RMSE) which is an standard way to measure the error of a model in predicting quantitative data, of around 2.0 K (Li, et al., 2022).

Figure 8 illustrates the processing chain for generating Landsat LSTs by (Ermida, et al., 2020). The date range, the Landsat satellite, the processing region of interest, and an

NDVI flag designating the application of the NDVI-based emissivity correction are first provided. Landsat LST loads the appropriate collections of Surface Reflectance and TOA Brightness Temperatures (BT) based on this information (SR). The quality information bands are used while a cloud mask is applied. Two of the TCWV NCEP analysis times that are closest to the Landsat observation time are chosen for each TOA BT image and interpolated. To get the fractional vegetation cover (FVC) values, the SR data are used to calculate the NDVI. These FVC values are then used to calculate the equivalent Landsat emissivity, which is then compared to previously computed ASTER emissivity values for bare ground. Finally, the Landsat TOA TB of the TIR band is subjected to the SMW algorithm; the algorithm coefficients are overlaid into the Landsat image based on TWVC from NCEP (Ermida, et al., 2020).

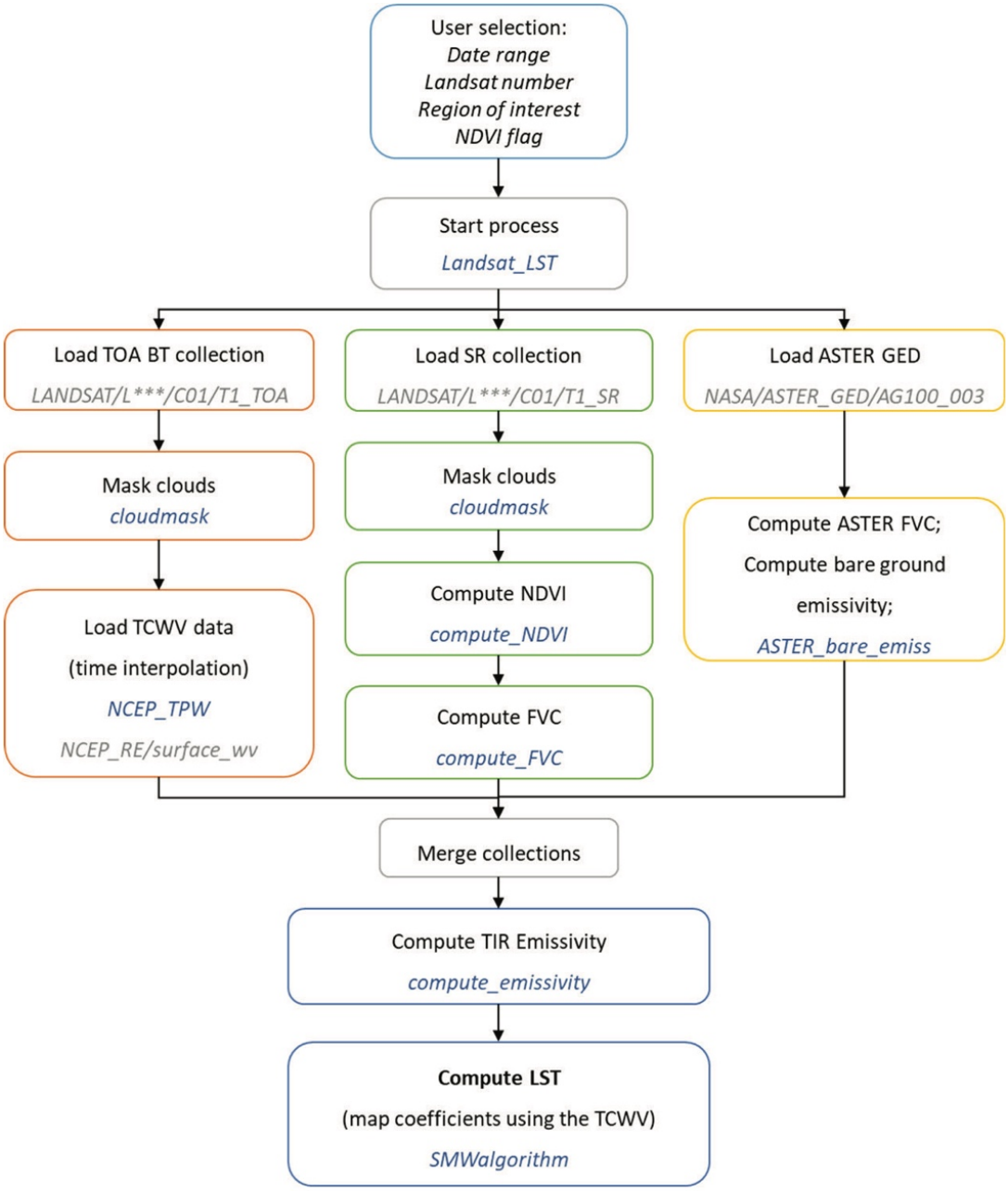

Figure 8 GEE processing chain for retrieving Landsat LST. The blue text indicates coded functions in modules. The gray text indicates GEE datasets used in the production; adopted from: (Ermida, et al., 2020: 6, Fig. 1).

CHAPTER 4

4 IMPLEMENTATION OF THE UHI DETECTION MODEL

This work uses multi-spectral and multi-temporal satellite data to determine the LST and, consequently, the development of UHIs as well as mitigation suggestions in four different classes of cities based on city size. Utilizing the GEE platform, the LSTs are extracted from remote sensing photos.
In this study, spatial and temporal LST data are taken from three summer seasons (1990, 2005, and 2021) and are evaluated for changes in temperature distribution throughout space using Landsat photos. UHI fluctuations are analyzed, mapped, and evaluated using high spatial and temporal resolution data from Landsat-5 Enhanced Thematic Mapper (ETM+), Landsat-7 Operational Land Imager (OLI), and Landsat-8 OLI/TIRS. The summer season was the main focus of this investigation.

4.1 STUDY AREA

Physical and human characteristics together define places. Their topography, climate, soils, and hydrology are some of their physical features. Human traits include things like language, religion, political and economic systems, and population distribution ((NGE), 2013).

4.1.1 HUMAN CHARACTERISTICS

One of the major geographic biases of the cities under investigation is the distribution of the population. Europe has received the most of attention in the chosen area (33%). Following the US, which had the second-highest number of studies (25%) and was followed by Iran, India, Australia, Japan, and Canada, which had about 10% of the studies, these cities were primarily included in global-scale studies without a specific focus.
Mega-metropolitan, metropolitan, medium-sized, and small urban areas are the four categories used to categorize the cities seen in this study. These cities include New York, Washington D.C., and Springfield in the United States; Vienna and Villach in Austria; Tehran in Iran; Quebec in Canada; Helsinki in Finland; Canberra in Australia; Palma in Spain; Latur in India; and Niihama in Japan (see Figure 9). The summer season defines them. Between June and August, throughout the summer, temperatures between 290 and 330 k. With the exception of Latur, which enjoys two summer months each year (April and May), Canberra's summer months are December, January, and February.

- Small urban areas, with population between 50,000 and 200,000
- Medium-sized urban areas, with population between 200,000 and 500,000
- Metropolitan areas, with population between 500,000 and 1.5 million
  Large metropolitan areas, with population above 1.5 million ((OECD), 2022).

Here is a list of the four kinds of functioning urban areas, organized by country, that the Organisation for Economic Cooperation and Development (OECD) determined using the approach stated in its study.
Test sites in this study are presented on the map as following (see Figure 9).

Table 6. City classification based on the size for the study area.

Country	Name of functional urban area	Class type	Total population in 2021
Iran	Tehran	Mega-metropolitan area	9,381,546
US	New York	Mega-metropolitan area	8,823,559
Austria	Vienna	Mega-metropolitan area	1,691,468
US	Washington D.C.	Metropolitan area	718,355
Finland	Helsinki	Metropolitan area	558,457
Canada	Quebec	Metropolitan area	528,595
Australia	Canberra	Medium-sized urban area	462,984
Spain	Palma	Medium-sized urban area	401,270
India	Latur	Medium-sized urban area	382,754
Ehime, Japan	Niihama	Small urban area	123,059
Ilinois, US	Springfield	Small urban area	113,394
Austria	Villach	Small urban area	61,879

4.1.2 PHYSICAL CHARACTERISTICS

In order to not only show LST changes during chosen time series (1990, 2005, 2021), but also to identify the differences in LST changes between various urban areas around the world, test sites from all over the world with various climatic characteristics (see Figure 9) and urban forms (see Figure 10) were chosen.

Figure 9 Distribution of selected test sites.

Figure 10 Administrative boundaries of selected test sites.

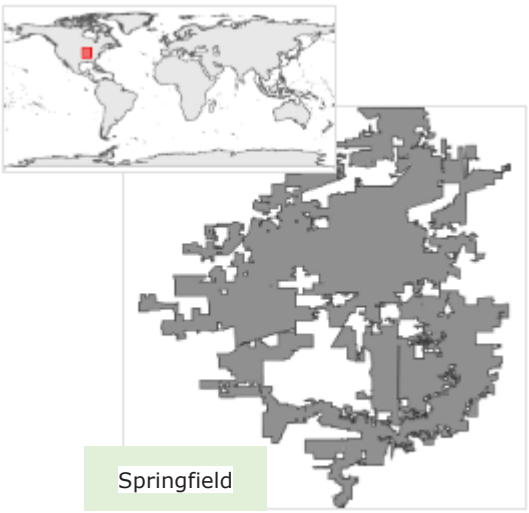

Figure 10 (continued)

The research region, comprising the twelve cities, is classified in six classes by Koppen-Geiger (Kottek, et al., 2006) as follows: Humid subtropical climate (Cfa), Marine west coast climate (Cfb), Mediterranean climate (Csa), Humid continental climate (Dfa, Dfb), and Tropical wet-dry climate (Aw) (see Table 7). Summertime is a feature of the test locations. The summer months are from June to August. Two exclusions apply. There are differences between Canberra in Australia and Latur in India during the summer. In Latur, it begins at the end of March and lasts through the end of May, whereas in Canberra, it lasts through the end of February. The summer months have very little precipitation. The summer months are from June to August. Two exclusions apply. There are differences between Canberra in Australia and Latur in India during the summer. In Latur, it begins at the end of March and lasts through the end of May, whereas in Canberra, it lasts through the end of February. The summer months have very little precipitation. Some coastal cities, like New York City, can experience simultaneous temperature increases of more than 300 K and relative humidity levels of up to 70%.

4.2 GEO DATABASE

This study uses remote sensing and GIS data to compare LSTs in twelve different cities which are classified based on their size. The study is conducted using multi-spatial and multi-temporal Landsat satellite (collection 2) data acquired from a Landsat-5 (TM) for years 1990 and 2005, and Landsat-8 Thermal Infrared sensors (OLI/TIRS) for year 2021. This study uses Landsat-5 instead of Landsat-7 to avoid scan line error in Landsat-7. There are some exceptions; Landsat-7 (ETM) was used for year 2005 in Tehran, Canberra, and Latur. Because Landsat-5 has no images for these cities in a certain time. In Landsat-8, band 10 is used for calculating surface temperature, while band 6 is used for Landsat-5 and 7.
Refers to (Ermida, et al., 2020) Landsat LST code repository, cloud coverage information, including cloud shadowing which is retrieved from the quality assessment band (BQA), is available in GEE. The characteristics of images used for the analysis are summarised in Table 8 (Villach city as an example to show which information are used) and all other eleven selected sites are presented in appendix 1.

Table 7. Koppen-Geiger climate classifcation for the study area.

City	Climate classification	Climate characteristics						
		Average annual temperature (K)	Warmest month		Coolest month		Average annual precipitation (mm)	Average annual percentage of humidity (%)
			Month	Temperature (K)	Month	Temperature (K)		
Tehran	Csa	290.93	July	309.26	January	260.35	236.22	43.8%
New York	Cfa	286.21	July	302.76	January	273.15	1135.38	71%
Vienna	Cfb	284.54	July	294.87	January	274.37	548.6	80.8%
Washington D.C.	Cfa	287.71	July	299.71	January	275.37	1008.4	65%
Helsinki	Dfb	278.15	July	294.26	February	251.98	632.5	79.6%
Quebec	Dfb	277.59	July	292.59	January	260.93	1137.9	78%
Canberra	Cfb	285.93	January	293.71	July	278.71	629.9	67.5%
Palma	Csa	291.04	August	299.04	January	284.87	464.8	70%
Latur	Aw	299.93	May	305.71	December	295.21	797.6	48.1%
Niihama	Cfa	286.32	August	297.54	January	275.15	1839	78.4%
Springfield	Dfa	284.82	July	297.48	January	270.21	950	71.1%
Villach	Dfb	281.37	July	291.87	January	269.93	1074.4	90.1%

Table 8. Time, mission, resolution, path and row, acquisition date, sun azimuth, sensor, and cloud cover of the records of images used to extract information for Villach (Austria) as an example.

City	Landsat Scene Identifier	Time	Mission	Resolution (m)	Path and Row	Acquisition date	Sun Azimuth angle	Sensor	Cloud Cover
Villach	LC81910272021166LGN00	9:51:37	L8	30*30	191×27	2021-06-15	142.76900404	OLI/TIRS	3,14
	LC81910272021182LGN00	9:51:41	L8	30*30	191×27	2021-07-01	141.60374855	OLI/TIRS	99,91
	LC81910272021214LGN00	9:51:51	L8	30*30	191×27	2021-08-02	145.23333874	OLI/TIRS	80,09
	LC81910272021230LGN00	9:51:56	L8	30*30	191×27	2021-08-18	149.23620275	OLI/TIRS	83,88
	LC81910282021166LGN00	9:52:01	L8	30*30	191×28	2021-06-15	140.31397837	OLI/TIRS	13,75
	LC81910282021182LGN00	9:52:04	L8	30*30	191×28	2021-07-01	139.16456406	OLI/TIRS	65,99
	LC81910282021198LGN00	9:52:06	L8	30*30	191×28	2021-07-17	140.21449440	OLI/TIRS	98,74
	LC81910282021214LGN00	9:52:15	L8	30*30	191×28	2021-08-02	143.27834461	OLI/TIRS	69,92
	LC81910282021230LGN00	9:52:20	L8	30*30	191×28	2021-08-18	147.60735077	OLI/TIRS	27,76
	LT51910272005154KIS00	9:39:14	L5	30*30	191×27	2005-06-03	139.47096964	TM	6
	LT51910272005170KIS00	9:39:21	L5	30*30	191×27	2005-06-19	137.15787149	TM	8
	LT51910272005202KIS00	9:39:37	L5	30*30	191×27	2005-07-21	138.10590551	TM	54
	LT51910272005218KIS00	9:39:46	L5	30*30	191×27	2005-08-06	141.44359826	TM	84
	LT51910282005154KIS00	9:39:38	L5	30*30	191×28	2005-06-03	137.10213231	TM	5
	LT51910282005170KIS00	9:39:44	L5	30*30	191×28	2005-06-19	134.67328898	TM	2
	LT51910282005202KIS00	9:40:01	L5	30*30	191×28	2005-07-21	135.90748456	TM	36
	LT51910282005218KIS00	9:40:10	L5	30*30	191×28	2005-08-06	139.53666557	TM	50
	LT51910271990177FUI00	9:11:57	L5	30*30	191×27	1990-06-26	126.44418946	TM	12
	LT51910271990193FUI00	9:11:55	L5	30*30	191×27	1990-07-12	126.94752318	TM	2
	LT51910271990209FUI00	9:11:51	L5	30*30	191×27	1990-07-28	129.49816191	TM	6
	LT51910271990225FUI00	9:11:46	L5	30*30	191×27	1990-08-13	133.61240714	TM	4
	LT51910271990241FUI00	9:11:40	L5	30*30	191×27	1990-08-29	138.55194470	TM	11
	LT51910281990177FUI00	9:12:21	L5	30*30	191×28	1990-06-26	124.07352076	TM	11
	LT51910281990193FUI00	9:12:19	L5	30*30	191×28	1990-07-12	124.69842050	TM	2
	LT51910281990209FUI00	9:12:15	L5	30*30	191×28	1990-07-28	127.46119445	TM	6
	LT51910281990225FUI00	9:12:10	L5	30*30	191×28	1990-08-13	131.83456972	TM	3
	LT51910281990241FUI00	9:12:03	L5	30*30	191×28	1990-08-29	137.03946203	TM	3

When researching the effects of the spatial pattern of LC on LST, the spatial resolution of an imagery is crucial (Abulibdeh, 2021). High temporal resolution and wide time coverage of the air temperature UHI allow it to accurately characterize UHI's temporal volatility but fall short in illustrating its geographic variation. Surface temperature UHI, which can give continuous and simultaneous surface temperature for a whole city, can address this flaw in air temperature UHI (Li, et al., 2013). LST has been extensively used to analyze the spatial pattern of UHI and its relationship with LC. LST is retrieved from infrared remote sensing pictures.

Different research on UHI produced different LC maps using remotely sensed image data with various spatial resolutions (Vannier, et al., 2011), (Liu & Weng, 2009), (Townsend, et al., 2009), (Wenga, et al., 2004). (Liu & Weng, 2009) for example, applied a spatial resolution of 90 m and 30 m, respectively, to study the connections between the LST and landscape level and pattern. (Wenga, et al., 2004) discovered that the 120 m is the optimal resolution for describing the link between LST and NDVI. (Li, et al., 2013) looked at the role of spatial resolution in defining the LST. Based on seven landscape indicators, they measured the spatial pattern of greenspace using three spatial resolutions (2.44 m, 10 m, and 30 m). They observed that photos with high spatial resolution allow for more accurate quantification of the greenspace spatial pattern, and as a result, the link between LST and the spatial configuration of greenspaces varies depending on the spatial resolution (Abulibdeh, 2021).
Five LC classes are identifed within the selected test sites using unsupervised classifcation to investigate the LST and the UHI efect as shown in Table 9.

Table 9. LC classifcation and defnitions are used in this study. Adapted from: (Abulibdeh, 2021: 259, Table 4).

Classes	**Definition**
Blue area	All water areas (water bodies, perennial Ice and Snow, open water)
Urban area	All built-up areas (residential, commercial, industrial, roads, parking lots, paved areas, construction sites)
Bare area	All areas containing exposed and non-developed surfaces (sand, rocks, soil)
Green area	All areas of natural or vegetation (parks, trees, grasses, golf courses)
Cropland area	All areas of lands that crop is grown in addition to the area cultivated, headlands, ditches and other non-cultivated areas.

4.3 Spatiotemporal Analysis

The findings, which are displayed as LST maps below, show that surface temperatures ranged between 290 and 330 K. 1990 is the year with the lowest remotely felt LST value, followed by 2005, which is higher than 2021 temps, although both years exhibit comparable spatiotemporal LST patterns across time for the eleven research locations (Figure 11). The only exception is Quebec City, Canada, where the temperature continues to drop over time.
Additionally, between 1990 and 2021, LST maps for the five LC types display various spatial patterns. All cities share the following similarity: blue regions have the lowest mean LST values, followed by green areas with lower mean LST values than cropland areas, and cropland and urban areas with higher LST values than bare areas (Table 10), which emphasizes the impact of LC on LST values (Figure 11).

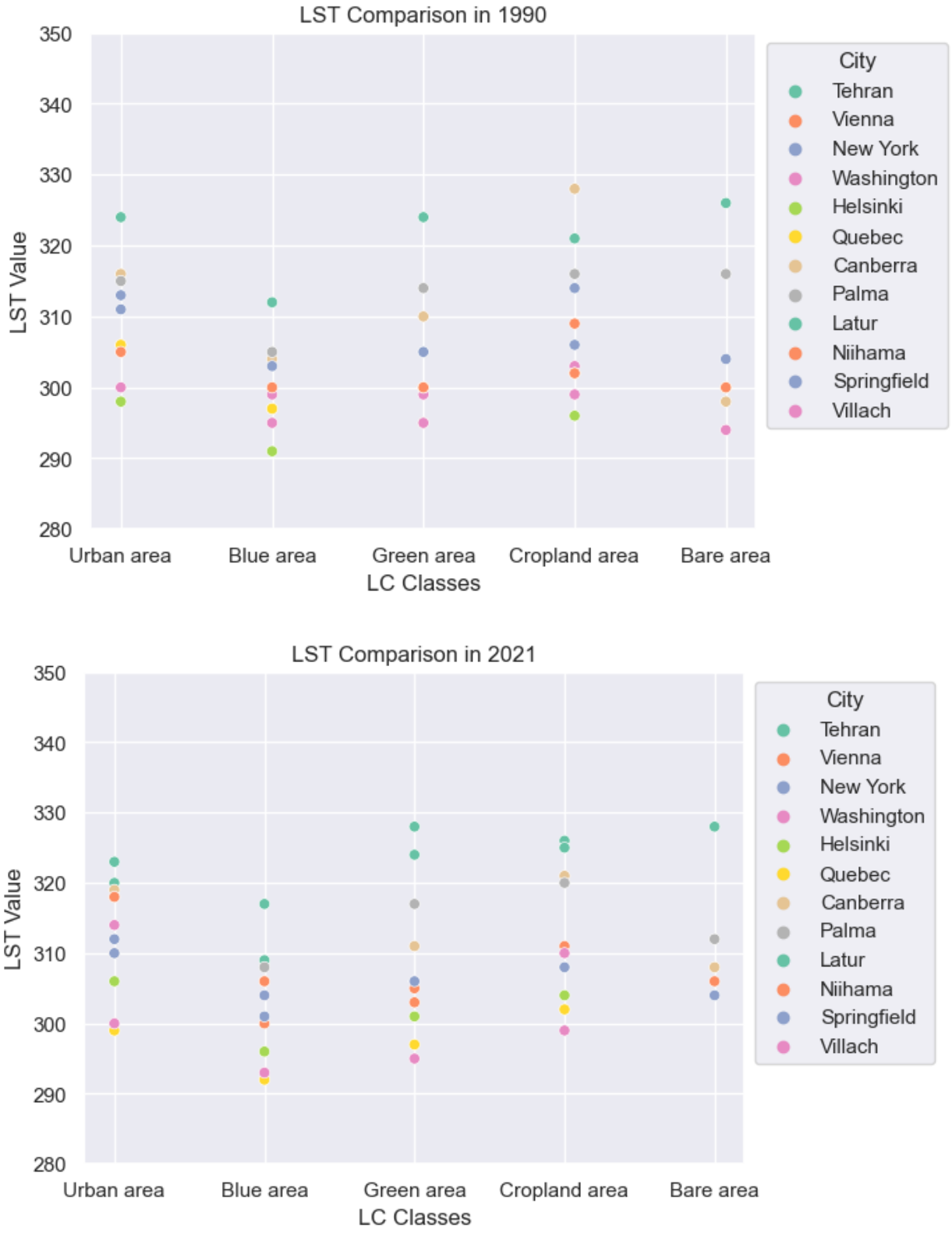

Figure 11 LST of the urban, blue, green, cropland, and bare areas in 1990 and 2021.

The LST comparison results show an inversion of the UHI phenomena in these cities since the major urban area's surface is impermeable, which absorbs more sunlight than blue or green areas due to the poor reflection of the pavement and buildings. Additionally, this pattern demonstrates a positive link between farmland, barren, and urban regions with mean LSTs and a negative correlation between green and blue areas and LST.
According to Table 10, the twelve cities experienced the greatest differences in the mean LST values between the five types of LC throughout time. The table displays the temperature pattern as temperature data are subject to LC categories at the chosen time series (figure 12).

Table 10. LST (K) and LC in 2021 and 1990.

		count	mean	std	min	0.25	0.5	0.75	max
LC Classes	**Year**								
Bare area	1990	8	267.3	108.50	0	297	300	307	326
	2021	6	259.7	127.50	0	304.5	307	311	328
Blue area	1990	11	300	5.73	291	297	299	303.5	312
	2021	12	303	7.14	292	299	304	306.5	317
Cropland area	1990	11	308.7	9.95	296	302	306	315	328
	2021	11	312.2	9.38	299	306	310	320.5	326
Green area	1990	11	304.3	8.79	295	299.5	300	307.5	324
	2021	12	308.3	10.14	295	302.5	306	312.5	328
Urban area	1990	11	309	7.63	298	305	306	314	324
	2021	12	312.4	7.77	299	309	313	318.25	323

Box and Whisker Plots were utilized in this study as an easy method of graphically exhibiting the results and explanatory data analysis to demonstrate the distribution of the data via their quartiles.

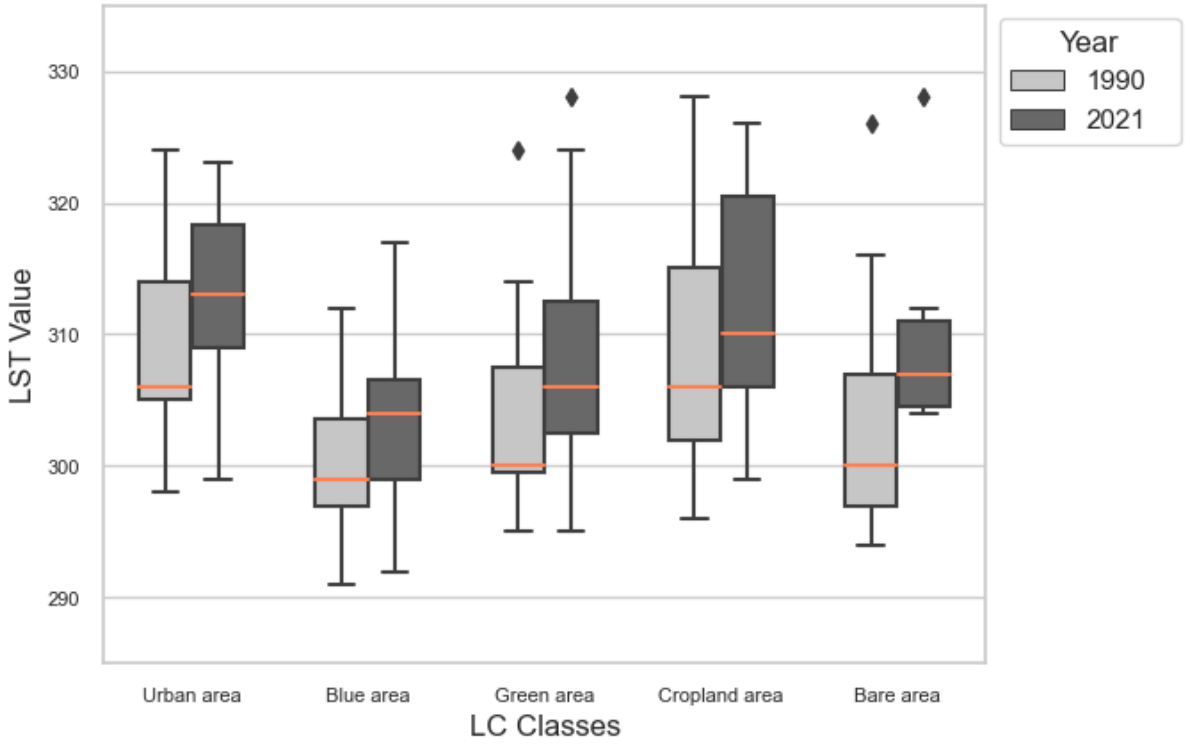

Figure 12 LST values for all twelve cities in two different time series. Boxes indicate the inter-quartile range, red lines indicate the median, and whiskers indicate the min and max LST values.

In the year 1990, although Latur has no data, the diference in temperatures between the bare areas and the urban areas range between 2 and 18 K, between the urban areas and green areas ranges between 0 and 7 K, between the green areas and cropland areas ranges between 2 and 18 K, between the cropland areas and bare areas ranges between 2 and 5 K (except Canberra city that has a huge difference temperature, around 30 K), between the blue areas and green areas ranges between 0 and 12 K, between green areas and bare areas ranges between 1 and 7 K (with this consideration that most of the selected test sites have no bare areas), bare areas and blue areas have a LST differences between 1 and 18 K, between blue areas and urban areas ranges between 5 and 14 K, and between urban areas and cropland areas ranges between 1 and 6 K (except Canberra city that has a difference temperature, around 12 K). The year 2021 shows a similar trend with a slightly diferent range in temperature between the five areas compared to 1990 period (Figure 13).

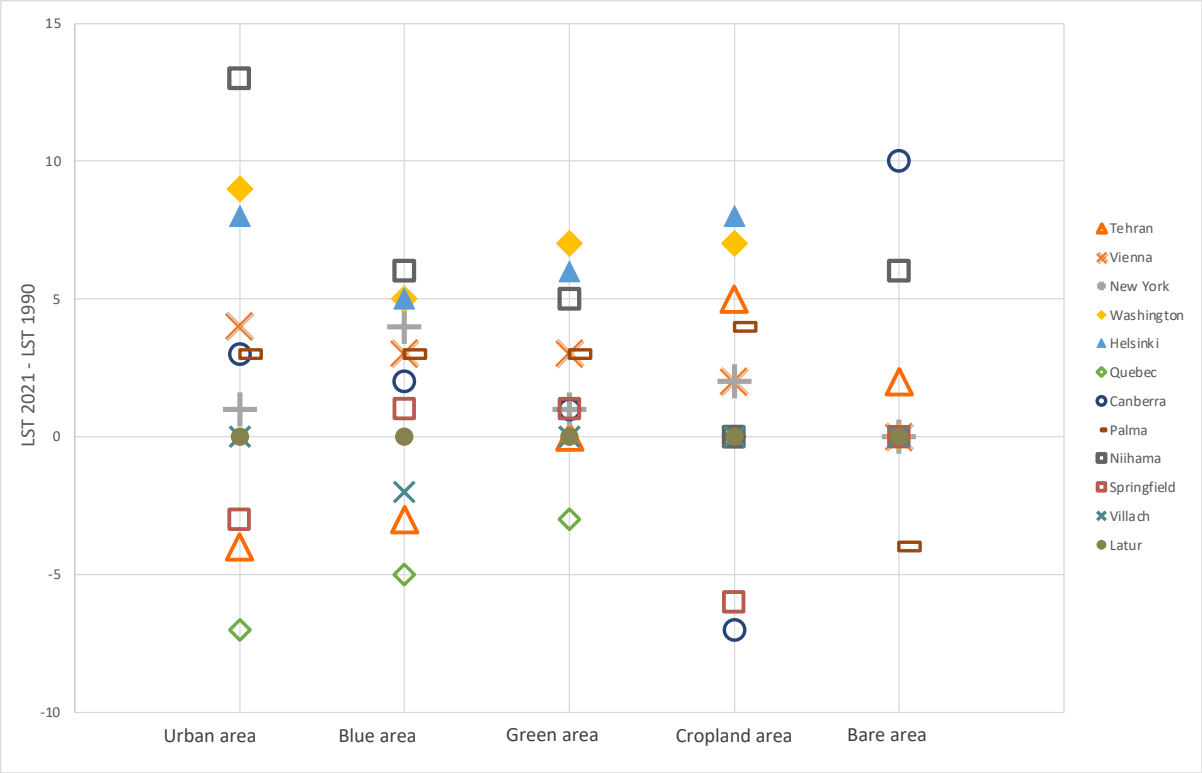

Figure 13 The difference in LST values between two time series (LST_{2021} - LST_{1990}) in each LC classes.

In mega-metropolitan cities (Tehran, New York, and Vienna), although the diference in temperatures between 1990 and 2021 ranges between 1 and 4 K in all three cities, but the point is that New York and Vienna have higher temperature in 2021 and this is vice versa about Tehran. It shows Tehran is a successful example in terms of lowering LST.
In metropolitan areas, Washington D.C. and Helsinki have 2 to 9 K higher temperature in 2021 in compare with 1990. While Quebec City has experienced lower temperature (between 0-7 K) in 2021 that it depicts Quebec is another successful case study to cool down the LST during the time series.
The diferences in temperatures between the year 1990 and 2021 for medium-size and small-size urban areas range between 1 and 10 K. While there is Villach city as an exception in the class of small-size urban areas with the same LST's value for each LC class. On the other hand, P-values of mean LST value (in K) between different LCs are listed in Table 11. P-value reported from t test is more than 0.05 that is said the result is insignificant means there is no relationship between each two LC classes being studied (one LC class does not affect the other). Table 11 states the results are due to chance and are not significant in terms of supporting this idea that there is a relashinship between each two LC classes.

Table 11. P-value reported from t test to represent LC relationships.

P-Value	Urban	Blue	Green	Cropland	Bare
Urban		0.24	0.20	0.29	0.27
Blue			0.20	0.41	0.38
Green				0.26	0.27
Cropland					0.48
Bare					

4.4 LST Validation

For a meaningful scientific use of satellite LST, information about the quality of the data sets has to be available. This can be obtained in several ways, including validation against in-situ data, radiance-based validation, satellite-satellite intercomparisons, or time series analysis (Martin, et al., 2019).
This study compares satellite data sets against in-situ measurements to validate them in order to learn more about the quality of the satellite data sets. Over one of the in-situ stations, which is situated in regions with various LC types, LST data sets obtained for a number of regularly used polar-orbiting and geostationary satellites are specifically compared. The in-situ station is: SURFRAD (Surface Radiation Budget Network) stations operated by the National Oceanic and Atmospheric Administration's (NOAA's) Office of Global Programs. SURFRAD stations provide hemispherical measurements of broadband infrared radiative flux. Despite offering high-quality data, a number of writers noted the SURFRAD measurements' limits for confirming satellite LST, chief among them a lack of spatial representativeness (Ermida, et al., 2020). One of the seven SURFRAD sites, which is mentioned in Table 12, is dispersed around the world. But due to surface heterogeneity difficulties that led to an incompatibility between ground and satellite footprints, we disqualified one of the SURFRAD sites. With in-situ LST derived from the Desert Rock, Nevada (DRA) site validation station, the quality of the derived Landsat LST is evaluated. In-situ data comparisons are only performed for Landsat-8 in the year 2021.
Landsat LST data are only validated for Vienna, New York, and Washington in June 2021, Tehran, and Palma in June, July, and August due to a lack of the information needed to calculate broad band emissivity, LST at well-maintained Landsat satellites and in-situ SURFRAD sites in specified time series (2021). Towards the conclusion, it displays a sizable number of Landsat LST values that are significantly lower/higher than the in-situ estimates, which is likely due to cloud contamination, a lack of data for a few days throughout the entire month, as well as global average variables for DRA data.

Table 12. Location, elevation, land cover type, and start date of the records of the SURFRAD stations used to assess the quality of the Landsat LST retrievals. Adapted from: Sekertekin, et al., 2019: 4, Table 1).

ID	Name	Latitude	Longitude	Elevation	Time Zone	Installed Date
DRA	Desert Rock, Nevada	36.62373°N	116.01947°W	1007m	8 hours from UTC	1-Mar-1998

4.4.1 In-situ LST Derivation

With an error of around 5Wm^ (-2), the SURFRAD stations give broadband measurements of hemispherical upwelling and downwelling infrared brightness. Every three minutes up to 2009, every minute following 2009, and every minute thereafter, two pyrgeometers measured upwelling and downwelling longwave radiations at a height of 10 m. (Duan, et al., 2021). All information can be accessed for free at (https://www.esrl.noaa.gov/gmd/grad/surfrad/). In this work, the Landsat LST product is validated using in-situ data gathered at the DRA site. Equation (1) uses the Stefan-Boltzmann formula to determine in-situ LST using upwelling and downwelling longwave radiations.

$$LST = \sqrt[4]{\frac{L_u - (1 - \varepsilon_{BB})L_d}{\varepsilon_{BB}\sigma_{SB}}} \quad (1)$$

where LST is the in-situ LST, Lu and Ld are the upwelling and downwelling longwave radiations, respectively, σ_{SB} is the Stefan–Boltzmann constant, and ε_{BB} is the broadband emissivity, which can be calculated from the ASTER GEDv3 product using a regression relationship (Duan, et al., 2021):

$$\varepsilon_{BB} = 0.128 + 0.014\varepsilon_{A10} + 0.145\varepsilon_{A11} + 0.241\varepsilon_{A12} + 0.467\varepsilon_{A13} + 0.004\varepsilon_{A14} \quad (2)$$

where εA10–εA14 are in ASTER bands emissivity 10-14, respectively.
The respective broadband value for each Landsat pixel is then obtained with Equation (2).

4.4.2. Statistical Analysis

Analysis revealed variations between the in-situ and estimated Landsat LST products between 0 and 5 K. Comparisons of in-situ LST and Landsat LST over Dfb regions, however, show that satellite estimates considerably underestimate the LST and that the Landsat LST algorithm can produce considerable inaccuracies in the recovered LST over places with high atmospheric water vapor. Due to inaccurate emissivity characterisation, differences of up to 4 K were seen over Csa and Mediterranean climate regions. In contrast, differences of up to 15 K were seen over Cfb and Aw regions with high atmospheric water content.
(Duan, et al., 2021) stated that there is a significant bias in the Landsat LST product at some vegetated sites because the land surface emissivity (LSE) estimation was flawed because LSE is independent of the normalized difference vegetation index (NDVI). A mean bias of the discrepancies between Landsat LST and in-situ LST is 1.0 K (2.1 K) over snow-free land surfaces, 1.1 K (1.6 K) over snow surfaces, and 0.3 K (1.1 K) over water surfaces, with the exception of the sites with inaccurate LSE estimation (Duan, et al., 2021). Due to the summer's higher spatial LST heterogeneity and somewhat lower atmospheric transmittance, large LST differences are observed at the DRA location (Duan, et al., 2021). However, bare soil surfaces have greater error in LST retrieval than vegetated surface s due to factors other than atmospheric and surface variables, such as greater uncertainty in the LSE determination (Li, et al., 2013).
The areas we chose for the time-series retrieval are far from the DRA stations, and the DRA station is situated in a desert region with little plant cover. These could be the cause of the significant bias between in-situ LST and LST computed by Landsat.

Table 13. Statistical analysis: mean bbe (K), mean Landsat LST (K), and mean In-situ LST (K) and variation between Landsat LST calculation and In-situ LST calculation.

June	**New York**	**Tehran**	**Vienna**	**Washington**	**Palma**
Mean bbe	0.97	0.98	0.97	0.97	0.65
Mean Landsat LST	306.04	315.80	308.60	307.89	205.37
Mean In-situ LST	311.95	311.75	311.90	311.84	207.89
Landsat LST-In situ LST	**-5.90**	**4.05**	**-3.30**	**-3.94**	**-2.52**
July					
Mean bbe		0.98			0.97
Mean Landsat LST		316.16			310.18
Mean In-situ LST		314.94			315.02
Landsat LST-In situ LST		**1.22**			**-4.85**
August					
Mean bbe		0.98			0.97
Mean Landsat LST		313.85			311.30
Mean In-situ LST		314.50			314.59
Landsat LST-In situ LST		**-0.65**			**-3.29**

CHAPTER 5

5 RESULTS

5.1 UHI MAPS VISUALIZATION

Using remote sensing and satellite images, the spatial LST value distributions are computed and visualized for each of the twelve cities. As illustrated in Figure 14, this is done to represent temperature differences and, consequently, the areas affected by UHIs for the years 1990, 2005, and 2021.

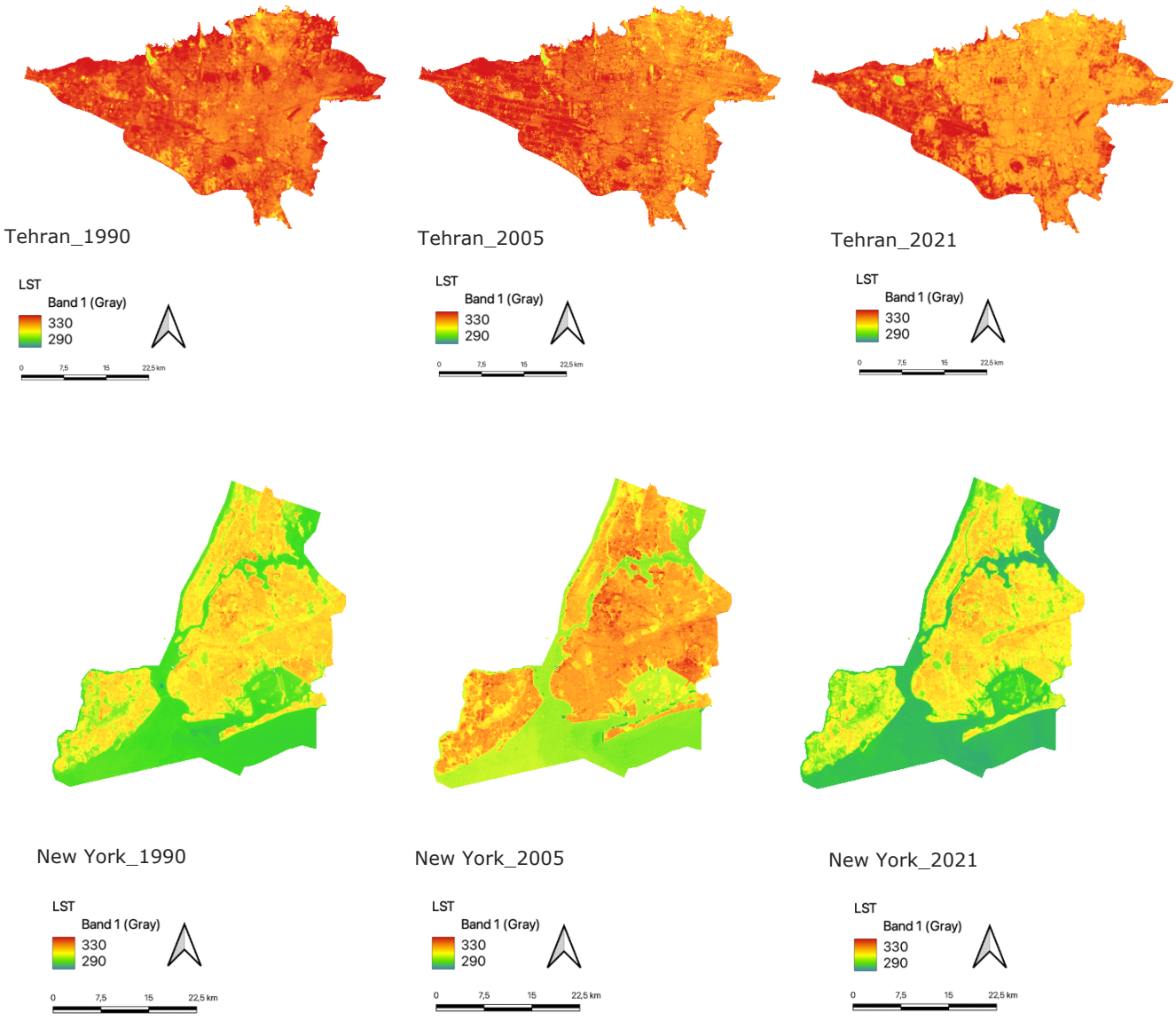

Figure 14 Mean LST (K) for the twelve cities in the years 1990, 2005 and 2021 assessed in this study.

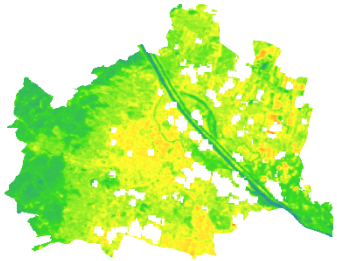

Vienna_1990

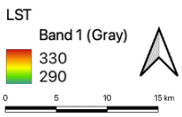

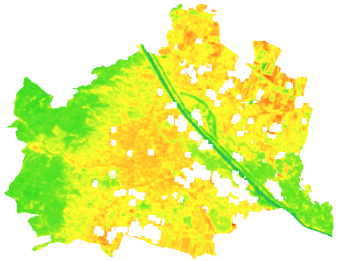

Vienna_2005

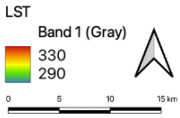

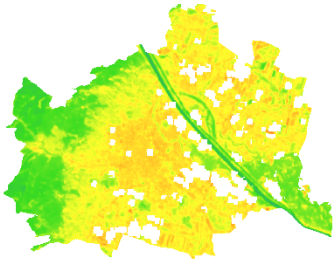

Vienna_2021

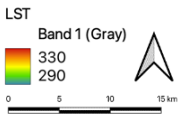

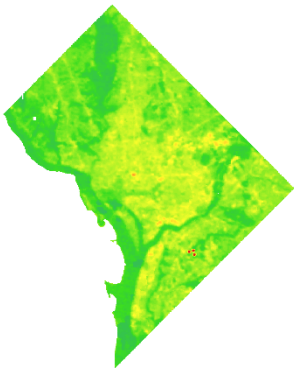

Washington_1990

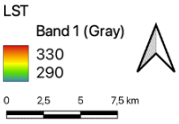

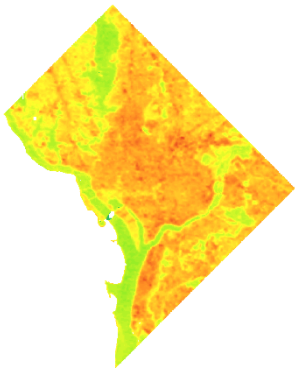

Washington_2005

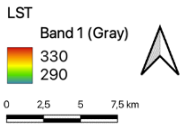

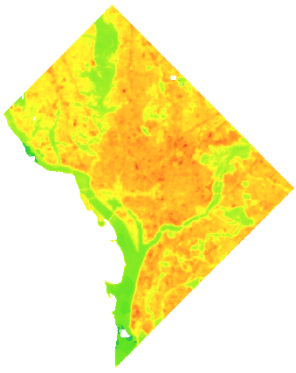

Washington_2021

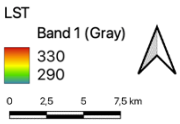

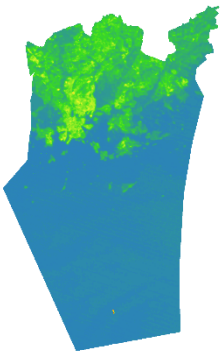

Helsinki_1990

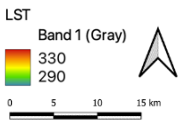

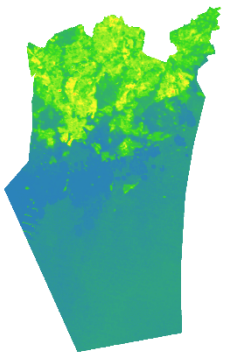

Helsinki_2005

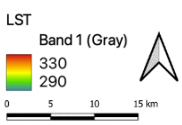

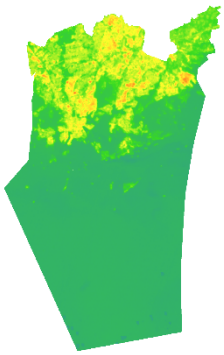

Helsinki_2021

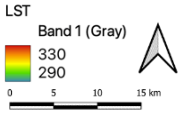

Figure 14 (continued)

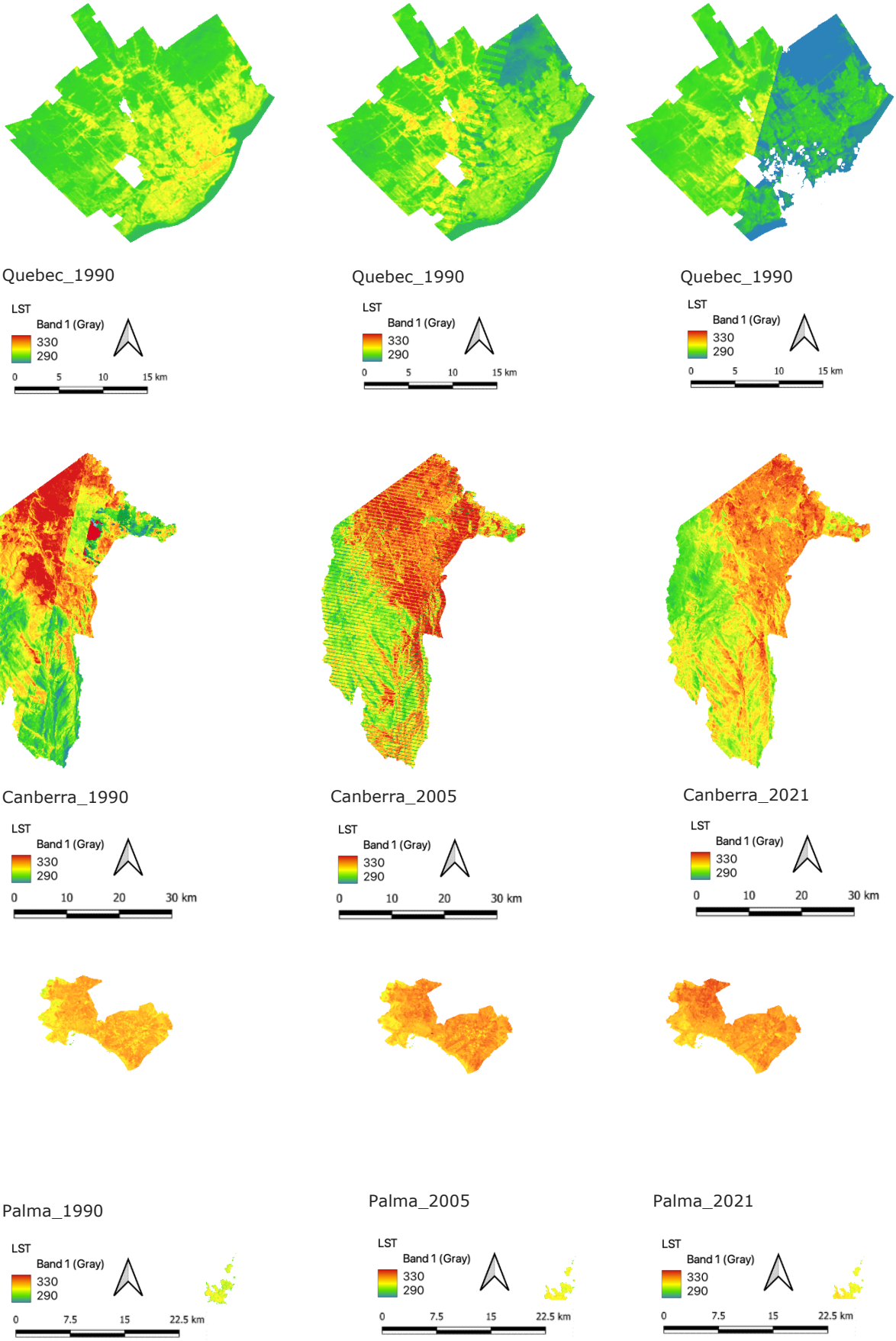

Figure 14 (continued)

No Data!

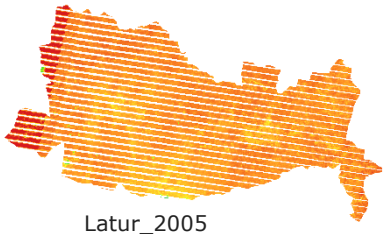

Latur_1990

Latur_2005

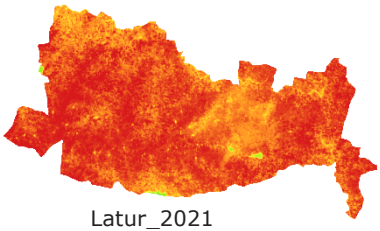

Latur_2021

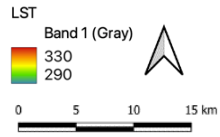

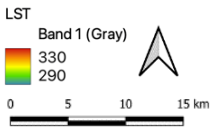

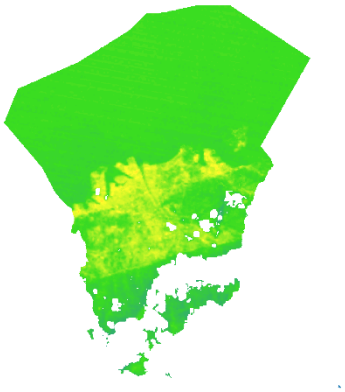

Niihama_1990

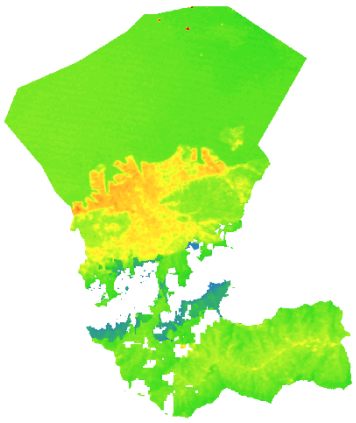

Niihama_2005

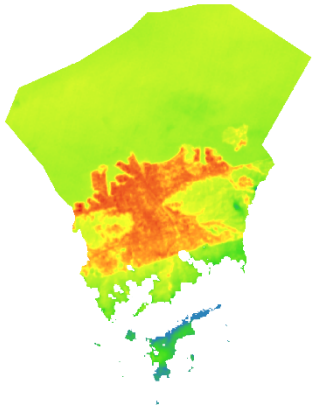

Niihama_2021

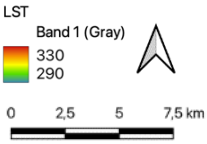

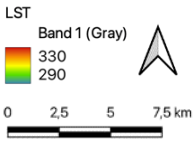

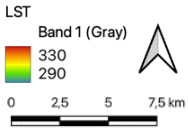

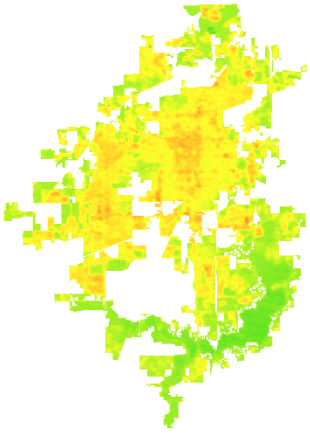

Springfield_1990

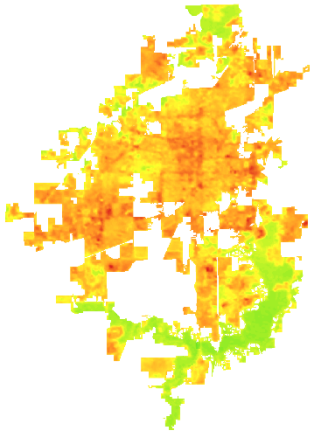

Springfield_1990

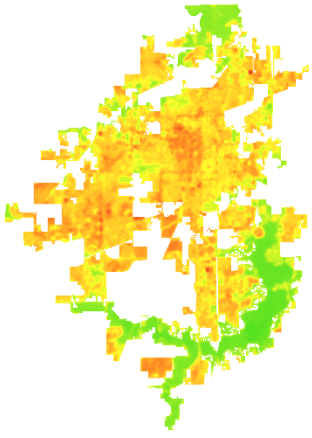

Springfield_1990

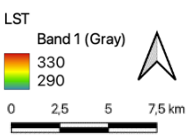

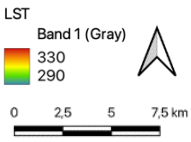

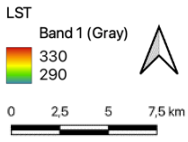

Figure 14 (continued)

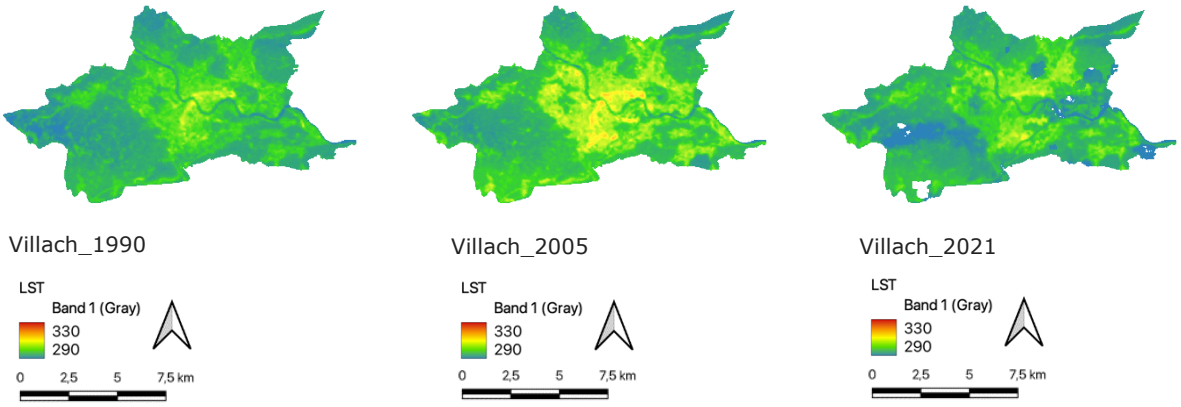

Figure 14 (continued)

5.2 Spatiotemporal Pattern of LC Dynamics

In Figure 15, the spatial LC maps of the twelve selected test sites are displayed. The observed changes show the percentage of each LC class that was converted to another LC between 1990 and 2021 (Table 14).

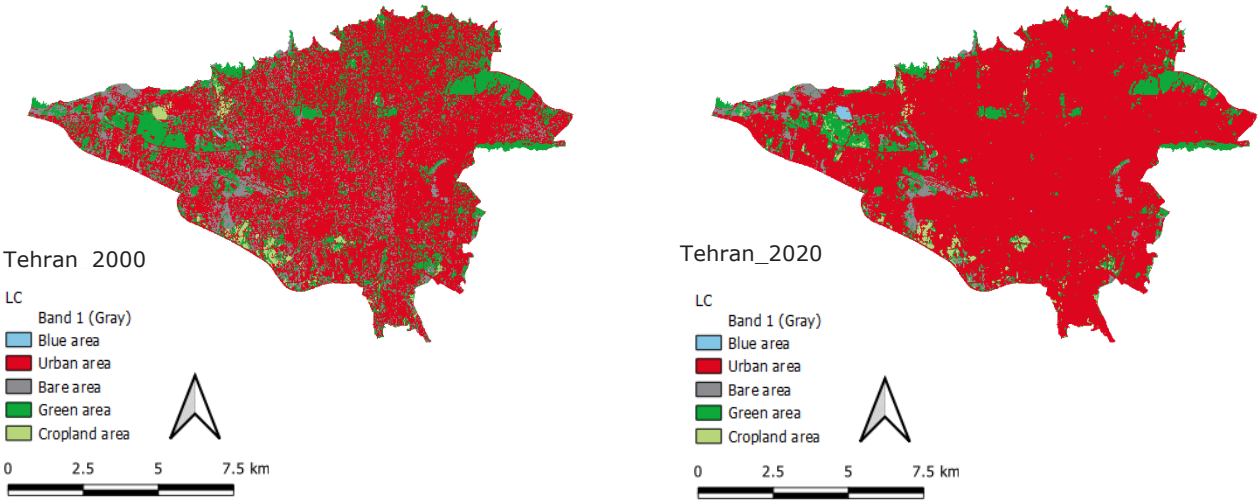

Figure 15 Spatial LC visual comparison for the twelve cities assessed in this study.

New York_2000

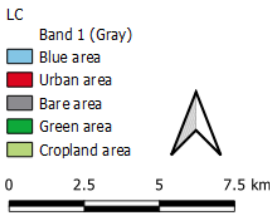

New York_2020

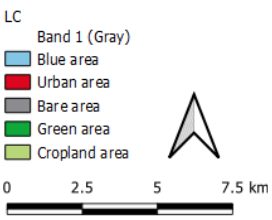

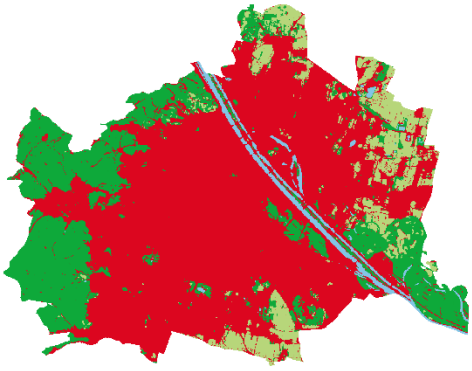

Vienna_2000

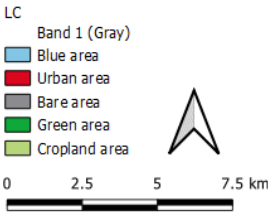

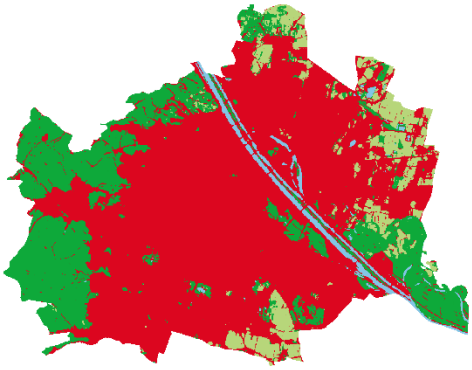

Vienna_2020

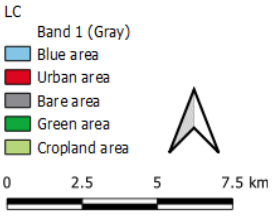

Figure 15 (continued)

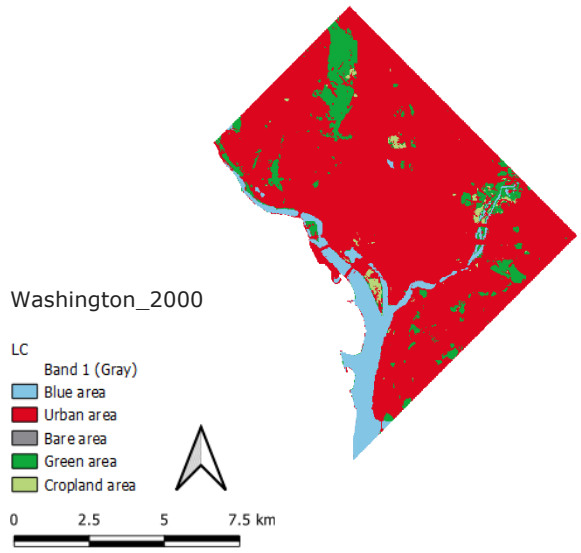

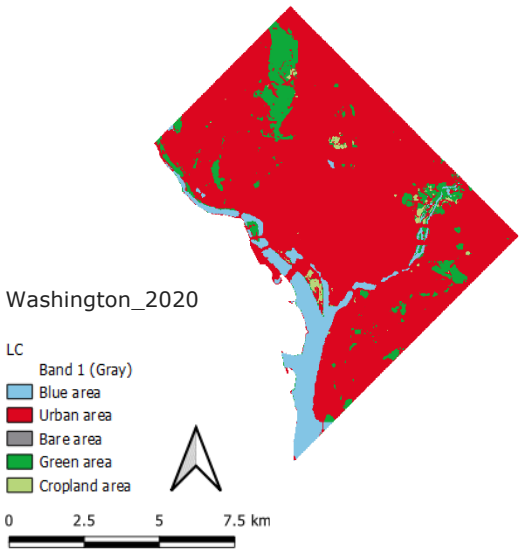

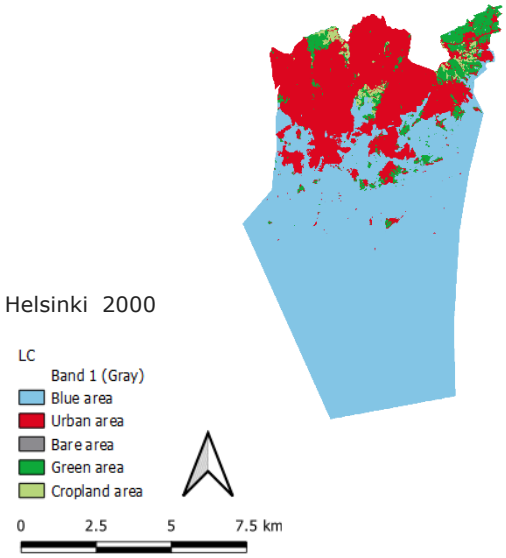

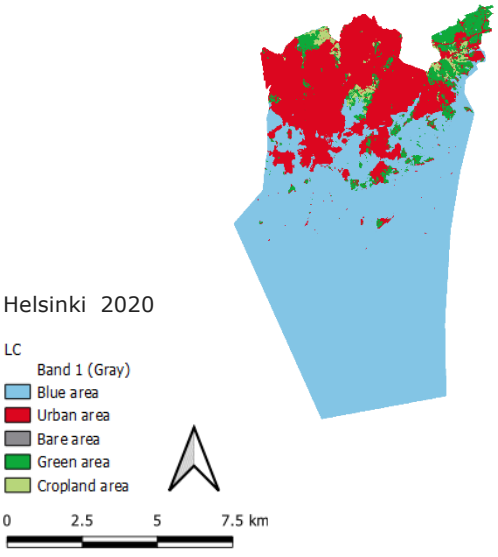

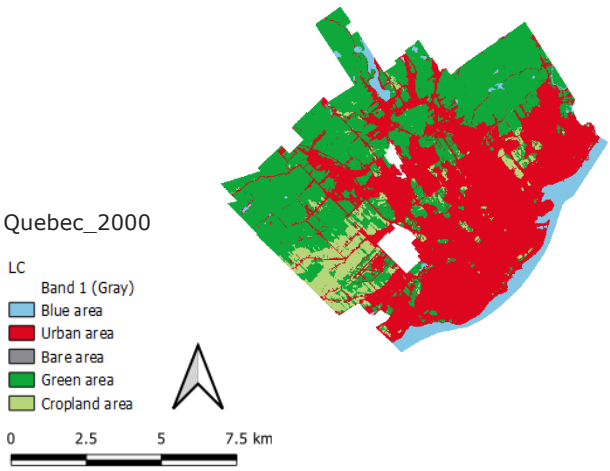

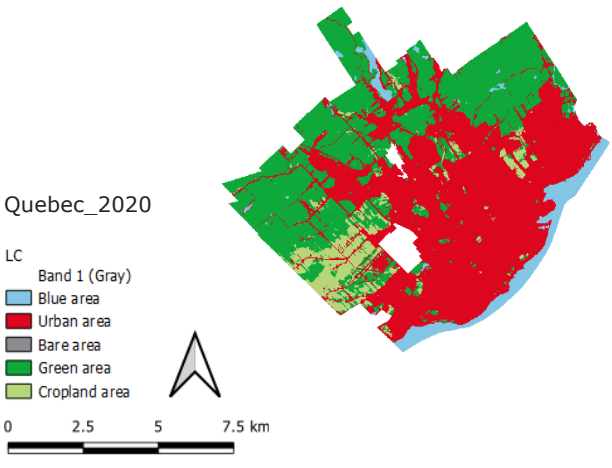

Figure 15 (continued)

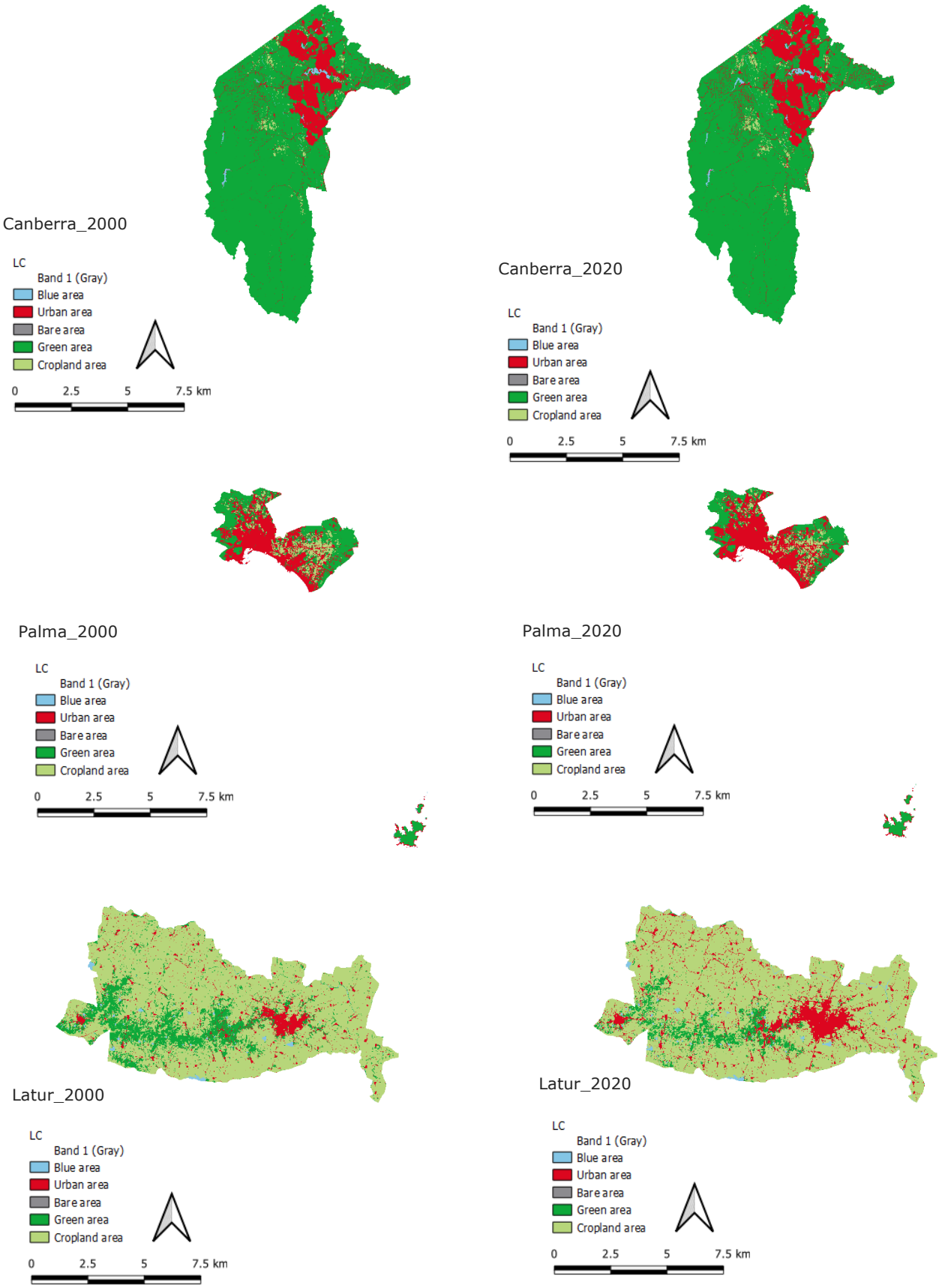

Figure 15 (continued)

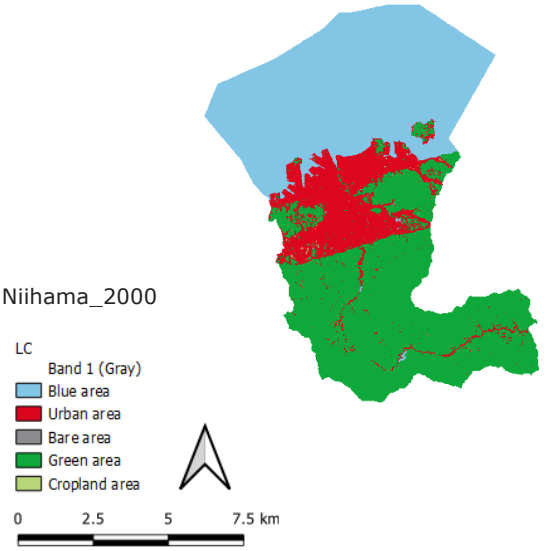

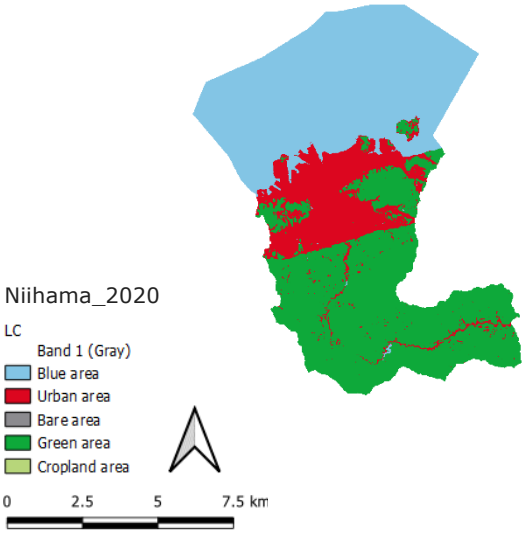

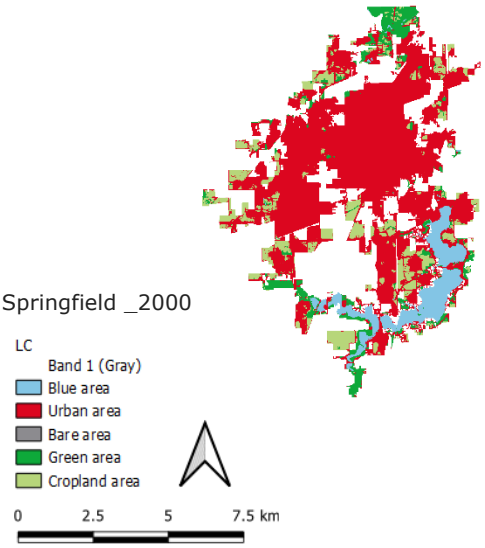

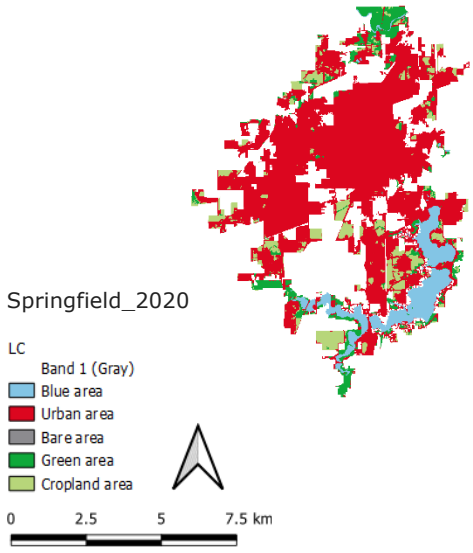

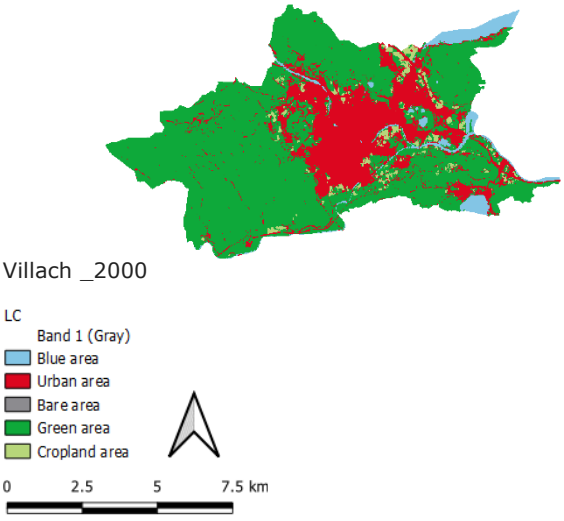

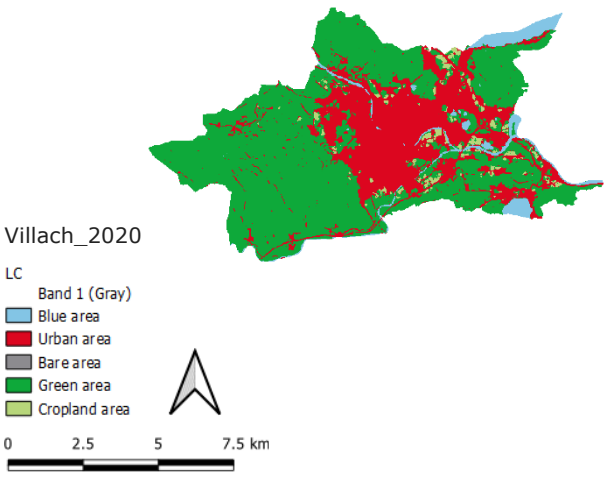

Figure 15 (continued)

Table 14 represents the area (in %) of each LC class in two different time series (1990 and 2021) for the selected test sites.

Table 14. Summary of the LC change (in %) from the maps (1990–2021) in twelve selected test sites.

LC Classes	Tehran		New York		Vienna	
	1990	2021	1990	2021	1990	2021
Urban	66.87	85.16	60.06	60.31	63.59	65.43
Blue	0.05	0.24	35.48	35.54	2.71	2.67
Green	19.88	9.75	3.99	3.45	24.47	24.28
Cropland	1.45	1.59	0.48	0.71	9.23	7.62
Bare	11.75	3.26	0.00	0.00	0.00	

	Washington		Helsinki		Quebec	
	1990	2021	1990	2021	1990	2021
Urban	82.11	82.95	23.13	23.96	46.60	49.95
Blue	8.79	8.58	70.24	70.05	5.82	5.83
Green	8.12	7.63	5.39	4.84	40.82	37.52
Cropland	0.98	0.83	1.23	1.15	6.76	6.70
Bare					0.00	

	Canberra		Palma		Latur	
	1990	2021	1990	2021	1990	2021
Urban	12.64	0.71	41.94	49.20	5.89	10.96
Blue	0.63	15.26	0.52	0.19	0.88	1.19
Green	85.44	82.22	45.35	40.34	15.20	7.53
Cropland	1.30	1.80	12.17	10.25	78.03	80.33
Bare	0.00	0.00	0.02	0.01		

	Niihama		Springfield		Villach	
	1990	2021	1990	2021	1990	2021
Urban	14.90	15.97	68.89	72.47	23.69	29.12
Blue	43.95	43.87	9.09	9.35	4.38	4.59
Green	41.09	40.15	8.53	8.16	69.11	63.94
Cropland	0.06		13.49	10.02	2.82	2.34
Bare	0.00	0.00			0.01	

Figure 16 gives a better insight not only about what is the relationship betwen different LC classes but also it depicts LC changes in different time periods.

Figure 16 Description of area (in %) of LC statistics for twelve selected test sites in 1990 and 2021.

Figure 16 (continued)

Figure 16 (continued)

Figure 16 (continued)

5.3 UHIs Spatial Patterns and Temporal Variations

As previously explained, LST is listed at five LC classes (urban, blue, green, cropland, and bare area) for the Landsat TM, ETM, and OLI/TIRS thermal bands. According to Table 15, the twelve cities experienced the greatest differences in the mean LST values between the five types of LC throughout time. For the five LC categories, each city displayed different LST spatial patterns. However, the majority of the selected test sites show that green and blue areas had lower mean LSTs than urban and bare areas, whereas cropland areas had higher mean LST values than bare areas (Table 15), which emphasizes the impact of LC on LST values. Additionally, this pattern reveals a negative relation between green and blue areas with mean LSTs and a positive relation between urban and bare areas with mean LSTs.

Table 15. Mean surface temperatures (K) for the twelve cities assessed in this study.

City	1990					2021				
	Urban	Blue	Green	Cropland	Bare	Urban	Blue	Green	Cropland	Bare
Tehran	324	312	324	321	326	320	309	324	326	328
New York	311	297	305	306	304	312	301	306	308	304
Vienna	306	297	300	309		310	300	303	311	
Washington	305	299	299	303		314	304	306	310	
Helsinki	298	291	295	296		306	296	301	304	
Quebec	306	297	300	302	300	299	292	297	302	
Canberra	316	304	310	328	298	319	306	311	321	308
Palma	315	305	314	316	316	318	308	317	320	312
Latur						323	317	328	325	
Niihama	305	300	300	302	300	318	306	305		306
Springfield	313	303	305	314		310	304	306	308	
Villach	300	295	295	299	294	300	293	295	299	

5.4 UHI Remedies Recommendations

Urban planning aims to balance conflicts between the need for expansion, social equality, and the environment while managing the use and development of land. To mitigate the effects of UHI effects, moderate temperatures, and increase urban areas' capacity to adapt to a warming climate, a range of solutions, policies, and strategies had been proposed, advocated for, and implemented in various cities. Applying cooling materials, increasing the amount of vegetation and water in urban areas, and reducing anthropogenic heat and water have been some of these strategies. However, only some of the many factors that affect these strategies' adoption and success can be taken into account by urban planning policies or urban contexts (density, scale, design, geometry). Environmental factors including scale, geography, climatology, and surface morphology are also included (Abulibdeh, 2021).

Therefore, the purpose of this chapter is to offer environmental experts' evidence and valuable advice so that development strategies and projects may be adjusted to reduce the effects of UHIs and moderate urban microclimates in urban areas. Planning takes such measures into account in order to reduce city temperatures, particularly in the summer. And hence, the findings of this chapter can be used to establish the fundamental principles that urban designers, urban planners, architects, and landscape designers, as well as public health departments, should follow in order to reduce urban areas' UHI impressions and increase their thermal comfort.

This can be done by highlighting how crucial green spaces are for minimizing the impacts of UHI. This necessitates analyzing the relationships between LC and LSTs in order to evaluate the city and its methods. These strategies not only help urban areas cool down,

but they also lower energy consumption and reduce on sources of air and water pollution, including greenhouse gas emissions (Giguère, 2009).

"By diminishing the accumulation of heat and applying cooling techniques, cities can reduce the temperature difference between urban and rural areas" (Filho, et al., 2017). The result of this study indicates that Quebec is one of the selected test sites that is successful to cooling down the temperature over time. There have been the UHI Mitigation Strategies catalogue in Quebec that can be used to suggest mitigation strategies:

- Vegetation.
- Sustainable urban infrastructure.
- Sustainable stormwater management.
- Reduction of anthropogenic heat.

The mitigating methods are then divided into groups according to magnitude (building and urban planning). The building mitigation measures are divided into three categories: protection from solar radiation, minimizing heat infiltration, reducing anthropogenic heat, and maintaining a comfortable thermal environment. In contrast, the urban planning and development measures are divided into three categories: greening, urban infrastructure, and anthropogenic heat reduction. The actions are arranged into four packages in the catalog created as part of the UHI project, which was carried out via the Central Europe Programme co-financed by the ERDF (Vienna University of Technology, 2014) structures the actions in four packages:

- Buildings.
- Pavements.
- Vegetation.
- Street morphology.

Since the mitigation strategies must be considered well prepared and consistently applied actions, three blocks of mitigation techniques are used in the Yamamoto compilation research (Yamamoto, 2006).

- Reduction of anthropogenic heat release.
- Improvement of artificial surface covers.
- Improvement of urban structure.

And introduces important characteristics for each mitigation strategy:

- Scale (individuals, buildings, ward, city).
- Period (short, medium, or long term).
- Degree of effect (on sweltering nights or on daytime temperature rise).
- Administrators of the actions (individuals, business institutions, local governments…).

The analysis of the aforementioned catalogues led researchers to the conclusion that, despite differences in catalog format, the essence of UHI mitigation measures is generally agreed upon.

5.5 Short term Solutions

5.5.1 Use of Light-colored Concrete and White Roofs

Researchers have discovered that using white roofs and light-colored concrete can reflect up to 50% more light and lower the ambient temperature. It's been demonstrated that these strategies provide excellent ways to lessen the UHI effect. Massive volumes of solar heat are absorbed by black and dull colors, making surfaces warmer. Overall air conditioning requirements can be decreased by using white roofs and light-colored concrete. For instance, as part of the GAF Cool Community Project, 1 million square feet of asphalt on Los Angeles (L.A.) roadways are being painted with solar-reflective paint. The program spans parking lots, playgrounds, and roads, and it has already cooled the surface by 10 to 12 degrees.

5.5.2 Green Roofs

A great way to decrease the effects of UHIs is using green roofs. The concept of "green roofing" involves growing plants on roofs in a similar way to how plants grow in gardens. In the summer, plants on the roof act as great insulators and reduce the total UHI effect. Plants reduce the need for air conditioning by cooling the surrounding environments. Additionally, because the plants create fresh air and absorb carbon dioxide, the air quality is enhanced. Street trees, curbside planting, and open space planting are additional techniques that can be applied. All of these methods reduce the cost of cooling urban areas while producing a cooling impact. "Using green roofs in cities or other built environments with limited vegetation can moderate the heat island effect, particularly during the day. Green roof temperatures can be 272-278 K (30–40°F) lower than those of conventional roofs and can reduce city-wide ambient temperatures by up to 258 K (5°F)" (EPA., 2014).

5.5.3 Green walls

Vertical ecosystems called "green walls" significantly reduce the temperature of the building envelope and increase energy efficiency. By increasing the building's thermal mass, these walls enable to prevent significant temperature fluctuations (Giguère, et al., 2009).
Protecting the building envelope from UV rays, capturing suspended particulates, and shielding walls from graffiti are a few advantages of these green installations (Lepp, 2008). They can be installed on any kind of structure, including fences, phone poles, and light standards.

5.5.4 Planting Trees in Cities

Planting trees in and around cities is a great way to reflect solar radiation and reduce the UHI impact at the same time. Trees have cooling effects, release oxygen and fresh air, absorb carbon dioxide, and provide shade. The ideal trees for urban areas are deciduous ones since they don't block out the sun's warmth in the winter and have a cooling impact in the summer. In addition, several studies have found that urban greening is a powerful method for lowering LST and so minimizing the impacts of UHIs (Abulibdeh, 2021).
Increased green space within the city is a crucial mitigating strategy. Evapotranspiration assists in keeping the air temperature between 1.6 and 3.3°C by intercepting solar energy before it is absorbed by the impermeable materials of the city, in addition to acting as a filter against wind currents. In addition, vegetation helps recharge groundwater and reduces surface temperature increases through evapotranspiration, which also applies to green roofs (Villanueva-Solis, 2017).

5.5.5 Green Parking Lots

The UHI effect is influenced by parking lots that are asphalt-paved because asphalt has a poor albedo (Rosenzweig, et al., 2005). It is advised that vegetation be grown within (vegetation medians) and around the perimeter of parking lots (vegetation strips) in order to lessen the heat retained in these asphalt surfaces and in the vehicles parked there. On paved areas, shade is to be produced. On paved areas, shade creation is the goal. According to (Giguère, et al., 2009), the shade provided by the trees will help shield the pavement from extreme heat fluctuations and increase its longevity.

5.6 Long Term Solutions

Characteristics of urban areas can affect how UHI effects arise. The lack of trees and vegetation, a large proportion of impervious surface area, less reflecting building and paving materials, and dense, compact construction that prevents heat loss can all

exacerbate the UHI impact. Consequently, a large part of the UHI impact is influenced by the built environment (U.S. EPA, 2008). When analyzing long-term UHI mitigation, it is preferable to take all possible alternatives into account. In order to mitigate UHI, this section will finish with a discussion of smart growth and nature-based solutions (NbS).
Smart growth strategies assist protects the environment while improving the aesthetics, livability, and economic vitality of communities. The main objectives of these plans are to increase the effectiveness of the transportation system and to determine how and where to accommodate both new and redevelopment ((EPA), 2011). In 1991, the Local Government Commission created the Ahwahnee Principles for Resource-Efficient Communities, which established the basis for new urbanism efforts and provided development vision for smart growth programmes. The principles are intended to assist local government decision-makers in reducing sprawl and promoting efficient development ((SMAQMD), 2019).
Due to UHI's possible health consequences, NbS are also becoming more and more popular in recent years for addressing environmental problems, including air pollution and climate change. NbS is defined by the European Commission as "Solutions that are inspired and supported by nature, which are cost-effective, simultaneously provide environmental, social and economic benefits and help build resilience" ((EC), 2021). It means NbS are resource-effective ways to reduce the negative effects of pollution and climate change while also enhancing the health and well-being of city dwellers and promoting (Menon & Sharma, 2021). The following is the NbS for UHI mitigation and adaptation:

5.6.1 Vegetation Cover

In metropolitan areas, increasing plant cover is one of the simplest strategies to reduce the impact of UHI. To assist reduce the consequences of UHI, several municipalities in the Capital Region have included this strategy into general plans, climate action plans, and other planning documents (WSP, 2019). Numerous studies have shown that vegetation cover has a great impact on moderating temperature, especially in urban areas (Chen, et al., 2020). It is proposed that increasing vegetation cover and greenery can reduce UHI, reduce air pollution, and enhance thermal comfort in cities. Native plant species with increased cooling capability and pollution tolerance provide excellent alternatives as a general solution to the issue of UHI. Thus, while developing mitigation strategies for urban heat, planners must pay attention to both the area covered by vegetation and its spatial distribution as well as the plant species that need to be planted. Green areas have effects on climate change mitigation and local and global adaptation (Menon & Sharma, 2021).
Additionally, greenery and open areas have many positive environmental effects. They provide ground water recharge and reduce surface runoff, which both contribute to better hydrology (Zhang, et al., 2015), (Ramaiah & Avtar, 2019). (Bai, et al., 2018) claim that green cover might also serve as a buffer to severe events like floods and support in climate adaptation by serving as natural storm water drains, lowering the risks of climate-related disasters for urban areas. So, large green areas with a single composition have larger cooling effects in terms of morphology (Kong, et al., 2014). To comprehend the relevance of the morphology of the urban greens, many landscape matrices have been investigated. An essential element in characterizing the morphology of a city's green space is the Landscape Shape Index. The cooling intensity is often low or occasionally negative for small green areas with complicated forms (Jaganmohan, et al., 2016). The form of the green spaces, in addition to their size, affects how well they can keep cool. For instance, it's been discovered that circular green area absorbs heat more effectively than square green space (Yu, et al., 2018). The impact of the shape and arrangement of green space on temperature reduction has been extensively explored, and conflicting results have been recorded in various case studies, which are studied by (Lu, et al., 2020) as follows:

- It was discovered by (Li, et al., 2012) that LST increased significantly with higher patch density, given a constant quantity of greenspace in the Beijing metropolitan area.

- (Peng, et al., 2016) stated a positive association between LST and the shape and fragmentation index of vegetated land in Beijing.
- In Isfahan, Iran, it was discovered by (Asgarian, et al., 2015) that a complex patch shape with extremely convoluted edges had higher moderating effects on LST.
- In Sacramento, CA, with a Mediterranean climate and hot and dry summers, (Ma, et al., 2016) found that mean patch size and edge density of trees had negative and positive effects on LST. They accomplished this by using analytical units with the greatest size of 1080 × 1080 m.
- (Masoudi, et al., 2019) used 240 × 240 m grids to analyze the complex relationship between green space pattern and LST in four major Asian cities. They discovered that while configuration was not a factor in Kuala Lumpur and Hong Kong, it was in Jakarta and Singapore where simply shaped, more aggregated, less fragmented patches of green space produced the best cooling effects.

Furthermore, the vegetation configuration is also observed to influence the cooling capacity of the green spaces. Green spaces with trees have stronger cooling effect than grass.

Planting trees has several advantages, but its shade, which helps prevent the low albedo surfaces that are common in urban areas from absorbing and releasing solar heat, is by far the most advantageous. Additionally, evapotranspiration—the term for the combined effects of transpiration and evaporation—has a very slight cooling impact. Water vapor is produced when water evaporates from a land surface and enters the atmosphere. Plants emit water vapor through a process called transpiration (WSP, 2019).

Plants often cover their stomata to decrease water loss during hot weather, hence the cooling potential of evapotranspiration is frequently exaggerated. Although other local factors, such humidity, have an influence, most plants start to close their stomata at 96.8°F (36°C), which limits evapotranspiration's ability to mitigate the effects of UHI (Giguère, et al., 2009).

Two significant cooling processes for cooling urban forestry are the increase in surface roughness (variation in height between urban landscape features) and the decrease in air pollution concentrations (which can trap heat). Height variability enhances atmospheric convection, which increases the efficiency with which surface heat is transported to the higher atmosphere (Giguère, et al., 2009).

A wider variety of transportation projects can combine the following green infrastructure strategies, which Georgetown Climate Center has studied ((GCC), 2022):

- **Green roofs**: Traditional roofs absorb sunlight and release heat into the atmosphere. On green roofs, vegetation provides shade for the roof and cools the air through evapotranspiration. In this approach, vegetation can make a green roof 100 °F cooler than a typical black roof, and these cooler roofs transfer less heat to the surrounding air. Although green roofs don't take up any additional land and help keep building occupants cooler, they don't have as much of an impact on air temperatures as vegetation at ground level does. Green roofs aid in lowering energy use, enhancing air quality, and lowering heat in addition to managing stormwater.
- **Permeable pavements**: Permeable pavements feature gaps that air and water may pass through. These gaps enable water to seep into the ground, minimizing runoff. By leaving out the smaller stones that are typically included, porous asphalt and concrete can both be created. More specialized types of porous pavements include interlocking concrete pavers, in which water drains through the spaces between precast blocks, and grass or gravel pavers, in which fill materials are arranged on top of a plastic grid. Due to lower heat storage and evaporation, permeable pavements can offer cooling effects. Streets, parking lots, alleys, and sidewalks can all benefit from permeable pavements. Some concerns about whether permeable pavements are suitable for cold climates or high-traffic areas are currently being tracked and evaluated in cities like Chicago and Washington, DC, with encouraging results so far.

- **Bioretention and bioswales**: Bioswales are a form of stormwater retention that employ vegetation and an open-channel shape to reduce runoff and filter pollutants, putting less load on stormwater infrastructure and enhancing water quality. By absorbing and storing part of the stormwater, bioswales—often incorporated into streetscapes or used to divert stormwater away from vital infrastructure—can help lessen the need for the installation of gray stormwater systems. Bioswales may lower temperatures, expand habitat for city animals, and enhance air quality. Moreover, they frequently have a positive aesthetic impact and may raise property prices.
- **Green streets, alleys, and parking lots:** Green streets, alleys, and parking lots can integrate all of the aforementioned strategies into a cohesive plan. Green streets and alleys can offer a number of advantages by combining the measures, including runoff and pollutant reduction, improved air quality, and UHI mitigation. Green parking lots can be constructed on both public and private property, although local governments often place them in the public right-of-way.
- **Rain gardens**: "Rain gardens are small gardens that are designed to survive extremes in precipitation and help retain or reduce stormwater runoff through infiltration or storage ((GCC), 2022)". The gardens are frequently tiny and positioned purposefully in places where rainwater already overwhelms drainage capacity. They can be incorporated into a larger streetscape or into a general landscape design. Rain gardens may lower temperatures, provide habitat for wildlife, and enhance aesthetics in addition to managing runoff and lowering nutrient pollution.
- **Urban forestry**: Urban forestry is appropriate for both public and private lands, including rights of way and close to already-existing structures and dwellings for shade. Along with advantages to mental health and other social factors, urban trees can help to reduce heat and improve air quality. In addition to expanding the current canopy and planting new trees, urban forestry regulations can also include legislation to protect older trees that already exist since they are better for stormwater management and public health than young trees. Urban forestry may need to balance canopy aspirations with power utility considerations and ongoing maintenance and care, especially during extreme weather events.

5.6.2 Cool Pavement

Cool pavements offer a chance to incorporate urban heat mitigation strategies, along with urban forestry, green roofs, rain gardens, and green streets. As a third of the urban land cover, pavement can have a substantial impact on the UHI effect. Conventional black pavements may absorb a lot of heat because they absorb 80–95 percent of incoming sunlight, with peak heat absorption occurring at surface temperatures of 48–67°C (120–150°F) (Akbari, et al., 1999), ((EPA), 2012). After then, at night, this heat is released, warming up neighborhoods and affecting public health. Pavements with lower surface temperatures than standard products are referred to as cool pavements. Although cool pavements lack a formal definition, practitioners tend to concentrate on two main types: reflecting (or high albedo) pavements and permeable or evaporative pavements ((EPA), 2012), ((EC), 2021). Reflective or cool-colored pavements absorb less sunlight, and therefore hold less heat than conventional pavement. They may be used to cover both fresh pavement and pre-existing pavement. They are made by utilizing a reflective or transparent binder, or a cool-colored surface coating.

Evaporative cooling is made possible by permeable pavements, which are porous and enable air, water, and water vapor to enter voids. The best places for permeable pavements are low-traffic areas like roadsides, alleyways, parking lots, and parking lanes. Non-vegetated permeable pavements include porous or rubberized asphalt, pervious concrete, and brick or block pavers (Ralla & Saadeh, 2018).

5.6.3 Cool and Green Roofs

Cool and green roofs are two common methods for reducing the impact of UHI. In general, cool roofs are less expensive and provide less co-benefits. Depending on their design, green roofs may have higher upfront expenses with more cobenefits. Plants adapted to hotter, drier regions with higher leaf succulence and lower water requirements can be used into adaptable green roof designs. In general, green roofs provide all the advantages of cool roofs, such as lower albedo, in addition to extra cooling and aesthetic advantages.

5.6.3.1 Cool Roofs

High solar reflectance and thermal emittance materials are used in cool roofs to reduce the temperature of the roof, which has a negative impact on UHI (EPA., 2014). The effectiveness of cool roofs in reducing the UHI impact in California was evaluated in 2019 research from the Lawrence Berkeley National Laboratory of the Department of Energy. The research discovered that, for California's urban regions, widespread adoption of cool roofs by 2050 might counteract 51–100% of the additional heat exposure projected as a result of climate change (Vahmani, et al., 2019). Even in places without air conditioning, cool roofs reduce interior temperatures, which lowers energy consumption and improves occupant comfort (such as patios or garages). There are several cool-roof systems available, each of which is appropriate for a particular architectural context. These methods employ white or reflective, cool-colored coatings when applied retrospectively to existing roofs. The optimum technology relies on a variety of project-specific factors, but all roofing materials with the energy star badge must satisfy minimal standards for solar reflectance and reliability criteria.

5.6.3.2 Green Roofs

Green roofs, often referred to as vegetated roofs or living roofs, typically cover a conventional roof with a waterproofing membrane, soil as the growth medium, and vegetation (plants). This kind of roof is a common UHI reduction strategy. Depending on the scope and requirements of the project, there are two broad types of green roof designs: extensive and intense. A thin covering of soil and hardy plants, such succulents, that require minimal maintenance, make up extensive roofs. Intensive roofs include deeper soil layers, a wider range of plants, and more elaborate architectural elements. Unless the area is open to the public and used for recreation, commercial and public buildings often have large green roofs ((GSA), 2011). Green roofs in many ways combine the advantages of cool roofs with urban forestry. A green roof, like cool roofs, lowers the energy consumption of a structure and its associated effects. Similar to urban forestry projects, green roofs reduce heat by boosting evapotranspiration and shading the building they are located on, which minimizes heat absorption. Although the roof surface in the transportation sector is significantly less than that in the construction sector, many structures associated with transportation (like bus stops) are highly visible, making them excellent candidates for green roof pilot projects ((SMAQMD), 2019).

CHAPTER 6

6 DISCUSSION OF CONTROVERSIAL ISSUES

This work presents a methodology to derive LST from the Landsat-5, 7, 8 within GEE and then, extensively analyse them based on LC classification. The drieved LST maps show Landsat-7 has the largest errors, followed by Landsat-5, and 8. These discrepancies are related to the different spectral characteristics of the sensors.
The quality of the LST retrievals was further assessed in comparisons with in-situ LST estimates from DRA station obtained from the SURFRAD network. Analysis revealed that the Landsat LST computed result was accurate and precise, with variations within the in-situ LST measurement site ranging from 0-5 K. The satellite output severely underestimates the LST, and the Landsat LST can have major inaccuracies in the recovered LST across regions of high atmospheric water vapor, according to comparisons between in-situ LST and the Landsat LST over Dfb climate regions. Due to inaccurate emissivity characterisation, errors of up to 4 K were seen over Csa and Mediterranean climatic regions, while variations of up to 15 K between the Landsat LST and in-situ measurement were seen over regions with high atmospheric water content Cfb and Aw.
In comparison to vegetation and water bodies, the mean LST in urban and barren regions is continuously greater. Vegetated areas can emit less radiation, enhance evapotranspiration, and give shade from canopies compared to impermeable surfaces like roads, pavements, buildings, and parking lots, which lowers the temperature in the area. The rising LST trend across all LC types over the research period suggests a general trend of surface warming. For instance, in the selected test sites, the mean LST of impervious surface was 0.39-7.96 K higher than the mean LST of green space. The initial hypothesis is that the increase in LST through time is due to an increase in human heat emission during urbanization, a decrease in naturally occurring vegetation, and an increase in the amount of heat-absorbing artificial materials.
Obtaining high-resolution images for each site is necessary in order to study and better comprehend how LC heterogeneity affects LST comparisons. When modeling environmental characteristics between LST and LC, the ideal cell grid size should be taken into account. Moreover, given that certain years are warmer than others, it is important to look at how LC affects LST by either reducing or amplifying it.
This study provided reference datasets on the seasonal severity of UHI throughout the summer, and it depicts that LST varies differently between districts. Given the possibility that the effects of UHI might be exacerbated in the near future by global climate warming, the findings of our study are expected to provide crucial information for future research.
It is important to consider a number of drawbacks of this study as follows:

- First, this study used only remote sensing derived index to identify UHI over the selected test sites with different size and climate performance. Further research may be more beneficial if it takes into account the meteorological variables, landscape metrics, and clear albedo because these factors have a significant impact on LST.
- Second, since UHI has significant daily and seasonal fluctuations, which would also be of great utility, we only took the summer season into account and so restricted its widespread application.
- Third, the issue of lowering pixel values caused by a lack of clear sky is most notably observed during the summer at most selected test sites, and as a result, the impact on LST is most noticeable during that time of year.
- Finally, the estimation of the validation of LST may also be done using an in-situ measurment. But it is important to note that the conclusions drawn from our study

were based on the analysis of high-resolution satellite data utilizing remote sensing methods, and the estimated LST was not completely validated with the real ground situation. Additionally, for DRA stations all over the world, some of the selected test sites are placed a little bit farther from the station location to cover more homogenous surfaces.

Despite these drawbacks, this research gives a better understanding of the local temperature changes and global warming within the large districts of the world and gives further information for developing potential mitigation actions. At the end, this chapter drives us to answer our research questions:

- How can a generic model determine spatiotemporal patterns of UHI?

UHIs are identified by measuring surface temperatures. Therefore, by using remote sensing technologies and satellite imagery, the spatial LST value distributions for the various LC classes were computed and mapped for each of the twelve cities. This was done to illustrate temperature variations and, consequently, the geographic regions affected by UHIs between 1990 and 2021. Then, comparisons against in-situ LST, which were obtained using radiance measurements from DRA station affiliated with the SURFRAD, are used to evaluate the accuracy of the Landsat LST computed using the suggested technique.

- How remote sensing image-based analysis can be used to detect UHI?

GEE is an online platform designed to make large data analysis simple for remote sensing users without increasing the need for local computer resources. In this work, we modified a code repository that provided by (Ermida, et al., 2020) to enable computing LSTs from Landsat-5, 7, and 8 within GEE.

- What is the remote sensing image-based analysis of the relationship between UHI and LC changes over different urban areas?

This study used data from the Landsat-5, 7 and 8 satellite images to analyze the UHIs in twelve cities with varying climatic performance. The analysis was based on LC classification including urban, blue, green, cropland and bare areas. The results showed that the mean LST in urban and bare areas is consistently higher than green and blue areas. So, compared to impervious surfaces, vegetated areas can reduce their surrounding temperature. Finally, an overall tendency of surface warming over the studied periods is indicated by the rising mean LST across all LC classes.

- What are the possible urban planning actions can be applied to mitigate UHI effects?

This research collects the possible urban planning actions which were proposed in two different categories, short-term and long-term solutions to reduce UHI effects.

CHAPTER 7

7 SUMMARY AND FUTURE WORK

7.1 SUMMARY

This study used satellite images from Landsat-5, Landsat-7, and Landsat-8 to detect the UHIs in twelve distinct cities located in various climatic zones. LC classification establishes the basis for the analysis (urban, blue, green, cropland, and bare areas). According to the results, despite the fact that the mean LST was highest in urban areas, there were some bare, green, and cropland regions that had greater LST. Urban and cropland regions predominate in the selected test sites, which is why they have a greater concentration of heat sinks than blue and green areas, despite the fact that they have a greater cooling impact. This indicates that other criteria could be important in figuring out LSTs and, thus, UHIs. For instance, Canberra City has the biggest deviation in mean LST since it is adjacent to both water and vegetation.
The difference between the minimum and maximum LST in each of the LC categories, however, did not necessarily come from the same category. The temperature difference between urban areas and blue areas varies from 1 to 13 K, that between urban areas and green areas from 6 to 8 K, that between urban areas and cropland areas from 2 to 8 K, that between urban areas and bare areas from 11 to 18 K, that between bare areas and cropland areas from 13 to 30 K, and that between cropland areas and green areas from 10 to 18 K.
The LST and LC comparison have no noticeable relationship based on the analysis of the Pearson correlation coefficient. That might be more reliable if the study used the ideal cell grid size in LC maps.
Additionally, each category's LST showed regional variation based on other factors like proximity to the sea or the density of urban and green regions. In order to research and keep track of the UHI rise in these cities, monitoring the time-series of LST is a valuable tool. To mitigate the consequences of UHI, as well as to moderate temperatures and improve urban regions' capacity to adapt to a warming climate, a range of initiatives, policies, and approaches had been developed, advised, and put into practice in various cities. These tactics have included employing cooling materials, boosting the amount of plant and water in urban areas, and lowering anthropogenic heat. However, the implementation and effectiveness of these strategies depend on many variables, and only some of these only some of these factors can be taken into account in urban planning policies.

7.2 FUTURE WORK

It will be necessary for future research to evaluate thermal data and images of temperature distribution over an area, which is frequently difficult due to several complicated controlling elements. Based on the review of recent literature, many critical elements that will affect satellite remote sensing of UHIs in the future can be identified: Based on a review of the recent research, many critical elements for the advancement of satellite remote sensing of UHIs can be identified:

- First, it is possible to determine the surface radiant temperature at each class of LC with greater accuracy than is now possible. It is crucial to assess the temperatures in each part of the ground and the impacts of various canopy structures.
- Second, the relationship between LST and NDVI needs to be considered. The platform dependency and nonlinearity of the relationship between NDVI suggest

that it may not be a suitable indicator for quantitative analyses of vegetation (Ngie, et al., 2014). For applications requiring biophysical metrics, as (Small, 2001) pointed out, more precise, physically based measures of vegetation abundance are needed. Therefore, the significance of spatial resolution for identifying patterns and changes in the landscape should also be highlighted, and further research into the relationship between NDVI variability and pixel size is necessary.

- Third, research should be done to determine how urban morphology affects UHI. More study is required to use elevation information and height measurements to UHI studies. In order to link urban morphology and topography to UHI studies, it is argued by (Ngie, et al., 2014) that radar-generated topography data (such as Shuttle Radar Topography Mission (SRTM), Light Detection and Ranging (LIDAR), and Interferometric Synthetic Aperture Radar (IFSAR) data) are particularly desirable.
- Forth, to conduct more in-depth research of the UHI formation in various cities, future research should take nighttime data, multiple daytime measurements, and seasonal change into consideration. For the purpose of developing planning suggestions, it is also important to take into account the various effects of day and night as well as seasonal conditions.
- Finally, further research is required to examine the continuing pandemic occurrences between 2020 and 2021 to have a better understanding of how human mobility limits affect the intensity of UHI. LSTs collected by satellites can aid in a better study of the temperature variations on a map, which will enhance the findings for further studies. To make the solutions better, it would be more useful to look at the specific human activities that had the most effects on UHI.

CHAPTER 8

8 CONCLUSION

Open soil and natural landscapes have been replaced by artificially constructed surfaces and infrastructure as a result of urbanization. The temperature of the land surface is significantly impacted by these changes. It emphasizes how crucial LC is in influencing the earth's temperature. Based on remote sensing data from Landsat-5, Landsat-7, and Landsat-8, this study computes Landsat LST for the years 1990, 2005, and 2021 to extract LSTs maps and compare with LC maps to determine the effects of various LC classes on the LST within GEE. The twelve test sites included in this study are Tehran (IR), New York (US), Vienna (AT), Washington (US), Helsinki (FIN), Quebec (CA), Canberra (AU), Palma (ES), Latur (IN), Niihama (JP), Springfield (US), and Villach (AT).
The main conclusions of the study are as follows:

- The generated LST maps depict that the surface temperatures varied between 290 and 330 K. Remotely sensed LST's value in 1990 is lowest, followed by 2005 are higher than 2021 temperatures, but they show similar LST spatio-temporal patterns over time for the study areas.
- According to the generated LC maps, during the past three decades, UHI has intensified by an average of 6 to 8 K as a result of the simultaneous loss of greenery and the growth of urban areas.
- Despite the fact that the mean LST was highest in urban areas, there were some bare, green, and cropland areas that had greater LST.
- In the selected test sites, arbitrary urban development was also associated with noticeable thermal comfort decrease, particularly in blue and green areas.
- According to the examination of the Pearson correlation coefficient, there is no meaningful association between the LST and the LC comparison.
- The findings of this study can be used by policymakers and urban planners to prevent further environmental destruction and promote the development of sustainable cities. In order to improve the environmental condition, nature-based solutions (such as using light-colored concrete materials, developing urban parks, forests, green roofs, and green walls) can be taken into consideration.

This research provides guidance for efforts to adapt to climate change, particularly for urban planning policies. Furthermore, the spatiotemporal analysis of LST around the world can be applied to improve temperature exposure estimation for varied researchs.

ACKNOWLEDGMENTS

This work was supported by the Austrian Marshall Plan Foundation. The author would like to thank the United States Geological Survey (USGS) and Google Earth Engine (GEE) to freely provide Landsat Archive satellite data and to analyze and download data, respectively. Additionally, the author thanks the department of Engineering and IT, Carinthia University of Applied Science (Austria) for their support and supervisions in doing this research. Also, many thanks to the department of Geography and Environmental Studies, University of New Mexico (US) for their resources as much of this work was completed during a visit to the University of New Mexico as a Marshall Plan Fellow.

BIBLIOGRAPHY

Abulibdeh, A. (2021). Analysis of urban heat island characteristics and mitigation strategies for eight arid and semi-arid gulf region cities. Environmental Earth Sciences, 80(7), 259. doi:10.1007/s12665-021-09540-7.

Akbari, H., Rose, L. S., & Taha, H. (1999). Characterizing the Fabric of the Urban Environment: A Case Study of Sacramento, California. Lawrence Berkeley National Laboratory. doi:10.2172/764362.

Al-Ghussain, L. (2019). Global Warming: Review on Driving Forces and Mitigation. Environmental Progress & Sustainable Energy [Online], 38(1), 13-21, doi: 10.1002/ep.13041.

Alahmad, B., Tomasso, L. P., Al-Hemoud, A., James, P., & Koutrakis, P. (2020). Spatial Distribution of Land Surface Temperatures in Kuwait: Urban Heat and Cool Islands. International Journal of Environmental Research and Public Health, 17(9), 2993, doi: 10.3390/ijerph17092993.

Almeida, C. R., Teodoro, A. C., & Gonçalves, A. (2021). Study of the Urban Heat Island (UHI) Using Remote Sensing Data/Techniques: A Systematic Review. Environments, 8(10), 105, doi: 10.3390/environments8100105.

Asgarian, A., Amiri, B. J., & Sakieh, Y. (2015). Assessing the effect of green cover spatial patterns on urban land surface temperature using landscape metrics approach. Urban Ecosystems, 18(1), 209-222. doi:10.1007/s11252-014-0387-7.

Bai, T., Mayer, A. L., Shuster, W. D., & Tian, G. (2018). The Hydrologic Role of Urban Green Space in Mitigating Flooding (Luohe, China). Sustainability, 10(10), 3584. doi:10.3390/su10103584.

Capital Region Transportation Sector. (2019). Retrieved from Urban Heat Island Mitigation Plan: https://www.airquality.org/LandUseTransportation/Documents/UHI%20Mitigation%20Plan.pdf.

Chen, M., Zhou, Y., Hu, M., & Zhou, Y. (2020). Influence of Urban Scale and Urban Expansion on the Urban Heat Island Effect in Metropolitan Areas: Case Study of Beijing–Tianjin–Hebei Urban Agglomeratio. Remote Sens., 12(21), 3491. doi:10.3390/rs12213491.

Chen, X.-L., Zhao, H.-M., Li, P.-X., & Yin, Z.-Y. (2006). Remote sensing image-based analysis of the relationship between urban heat island and land use/cover changes. Remote Sensing of Environment, 104(2), 133-146.

Cooling Singapore. (2017). A catalogue of strategies to mitigate Urban Heat Island and improve outdoor thermal comfort for tropical climate. Retrieved October 2017, from https://www.coolingsingapore.sg/reports.

Department of Energy. (n.d.). Retrieved from https://www.fueleconomy.gov/feg/atv.shtml.

Duan, S.-B., Li, Z.-L., Zhao, W., Wu, P., Huang, C., & Xiao-Jing. (2021). Validation of Landsat land surface temperature product in the conterminous United States

using in situ measurements from SURFRAD, ARM, and NDBC sites. International Journal of Digital Earth, 14(5), 640-660. doi:10.1080/17538947.2020.1862319.

Echevarria, L., Dobbelsteen, A., & van der Hoeven, F. (2016). The Urban Heat Island Effect in Dutch City Centres: Identifying Relevant Indicators and First Explorations. In W. L. Filho, K. Adamson, R. M. Dunk, U. M. Azeiteiro, S. Illingworth, & F. Alves, Implementing Climate Change Adaptation in Cities and Communities. Switzerland: Springer International Publishing.

Environmental Protection Agency U.S., (2012). Retrieved from Urban Heat Island: Cool Pavements: www.epa.gov/heat-islands/heatisland-compendium.

Environmental Protection Agency U.S., (2011). Smart Growth, a Guide to Developing and Implementing Greenhouse Gas Reductions Programs, s.l.: s.n.

Environmental Protection Agency U.S., (2012). Heat Island Compendium [Online] Available at: www.epa.gov/heat-islands/heatisland-compendium

Euoropean Environment Agency, E. E. A., (2012). Urban adaptation to climate change in Europe Challenges and opportunities for cities together with supportive national and European policies, Copenhagen: https://www.eea.europa.eu/publications/urban-adaptation-to-climate-change.

Environmental Protection Agency U.S., (2008). Urban Heat Island Basics. In Reducing Urban Heat Islands: Compendium of Strategies. https://www.epa.gov/heat-islands/ heat-island-compendium. Retrieved from https://www.epa.gov/heat-islands/heat-island-compendium.

Environmental Protection Agency U.S., (2014). Retrieved from Reducing Urban Heat Islands: Compendium of Strategies: Cool Roofs: https://www.epa.gov/sites/default/files/2014-06/documents/coolroofscompendium.pdf.

Ermida, S. L., Soares, P., Mantas, V., Göttsche, F.-M., & Trigo, I. F. (2020). Google Earth Engine Open-Source Code for Land Surface Temperature Estimation from the Landsat Series. Remote Sensing, 12(9), 1471; doi:10.3390/rs12091471.

European Commission. n.d. (2021, April 20). Retrieved from Nature-Based Solutions: https://ec.europa.eu/info/researchand-innovation/researcharea/environment/nature-basedsolutions_en.

Filho, W. L., Echevarria, L., Omenche, V., & Al-Amin, A. Q. (2018). Impacts, strategies and tools to mitigate UHI. In L. E. Icaza, Urban and regional heat island adaptation measures in the Netherlands. A+BE | Architecture and the Built Environment.

Gartland, L. (2008). Heat Islands: Understanding and Mitigating Heat in Urban Areas. Washington: Earthscan.

Georgetown Climate Center. (n.d.). Retrieved 2022, from Green Infrastructure Strategies and Techniques: https://www.georgetownclimate.org/adaptation/toolkits/green-infrastructure-toolkit/introduction.html.

Giguère, M. (2009). Urban Heat Island Mitigation Strategies. Institut National de Santé Publique du Quebec. Retrieved from https://www.inspq.qc.ca/pdf/publications/1513_UrbanHeatIslandMitigationStrategies.pdf.

Giguère, M., Dubé, N., & Colas, J. (2009, July). Urban Heat Island Mitigation Strategies. Retrieved 2012, from https://www.inspq.qc.ca/pdf/publications/1513_UrbanHeatIslandMitigationStrategies.pdf.

Goldberg, D. (1978). Manual of the general health questionnaire. Windsor: NFER-Nelson.

Gorelick, N., Hancher, M., Dixon, M., Ilyushchenko, S., Thau, D., & Moore, R. (2017). Google Earth Engine: Planetary-scale geospatial analysis for everyone. Remote Sensing of Environment, 202(0034-4257), 18-27, doi: 10.1016/j.rse.2017.06.031.

Hendel, M., Gutierrez, P., Colombert, M., Diab, Y., & Royon, L. (2016). Measuring the Effects of UHI Mitigation in the Field: Application to the Case of Pavement-Watering in Paris. Urban Climate, 16, 43-58, doi: 10.1016/j.uclim.2016.02.003.

Howard, L. (1818). The Climate of London. Retrieved from https://www.urban-climate.org/documents/LukeHoward_Climate-of-London-V1.pdf.

Huang, K., Luo, W., Zhang, W., & Li, J. (2021). Characteristics and Problems of Smart City Development in China. Smart Cities, 4, 1403-1419, doi: 10.3390/smartcities4040074.

Huang, L., Li, J., Zhao, D., & Zhu, J. (2008). A fieldwork study on the diurnal changes of urban microclimate in fourtypes of ground cover and urban heat island of Nanjing, China. Building and Environment, 43, 7-17, doi: 10.1016/j.buildenv.2006.11.025.

Jaganmohan, M., Knapp, S., Buchmann, C. M., & Schwarz, N. (2016). The Bigger, the Better? The Influence of Urban Green Space Design. J. Environ. Qual., 45, 134–145. doi:10.2134/jeq2015.01.0062.

Kaplan, G., Avdan, U., & Avdan, Z. Y. (2018). Urban Heat Island Analysis Using the Landsat 8 Satellite Data: A Case Study in Skopje, Macedonia. Remote Sensing, 2(7), 358, doi:10.3390/ecrs-2-05171.

Kleerekopera, L., Escha, M. v., & Salcedo, T. B. (2012). How to make a city climate-proof, addressing the urban heat island effect. Resources, Conservation and Recycling, 64, 30-38, doi: 10.1016/j.resconrec.2011.06.004.

Kong, F., Yin, H., James, P., Hutyra, L. R., & He, H. S. (2014). Effects of spatial pattern of greenspace on urban cooling in a large metropolitan area of eastern China. Landscape and Urban Planning, 128, 35-47. doi:10.1016/j.landurbplan.2014.04.018.

Kottek, M., Grieser, J., Beck, C., Rudolf, B., & Rubel, F. (2006). World Map of the Köppen-Geiger climate classification updated. Meteorologische Zeitschrift, 15(3), 259-263. doi:10.1127/0941-2948/2006/0130.

Kuang, W., Hou, Y., Dou, Y., Lu, D., & Yang, S. (2021). Mapping Global Urban Impervious Surface and Green Space Fractions Using Google Earth Engine. Remote Sensing, 13(20), 4187, doi:10.3390/rs13204187.

Kumar, L., & Mutanga, O. (2018). Google Earth Engine Applications Since Inception: Usage, Trends, and Potential. Remote Sensing, 10(10), 1509; doi: 10.3390/rs10101509.

Lawrence Berkeley National Laboratory. (n.d.). Retrieved from Cool Pavements: https://heatisland.lbl.gov/coolscience/cool-pavements

Lepp, N. W. (2008). Planting Green Roofs and Living Walls (Vol. 37). Journal of Environmental Quality. doi:10.2134/jeq2008.0016br

Li, C., Cao, Y., Zhang, M., Wang, J., Liu, J., Shi, H., & Geng, Y. (2015). Hidden Benefits of Electric Vehicles for Addressing Climate Change. Scientific Reports, 5(9213). doi:10.1038/srep09213.

Li, L., Zhan, W., Huilin, D., Lai, J., Wang, C., Fu, H., . . . Miao, S. (2022). Long-Term and Fine-Scale Surface Urban Heat Island Dynamics Revealed by Landsat Data Since the 1980s: A Comparison of Four Megacities in China. Journal of Geophysical Research Atmospheres, 127(5), 1-21, doi: 10.1029/2021JD035598.

Li, X., Zhou, W., & Ouyang, Z. (2013). Relationship between land surface temperature and spatial pattern of greenspace: What are the effects of spatial resolution? Landscape and Urban Planning, 114, 1-8. doi:https://doi.org/10.1016/j.landurbplan.2013.02.005.

Li, X., Zhou, W., Ouyang, Z., Xu, W., & Zheng, H. (2012). Spatial pattern of greenspace affects land surface temperature: evidence from the heavily urbanized Beijing metropolitan area, China. Landscape Ecol, 27, 887-898. doi:10.1007/s10980-012-9731-6.

Lillesand, T., Kiefer, R. W., & Chipman, J. (2008). Remote Sensing and Image Interpretation (7th Edition ed.). (Wiley, Ed.) United States of America: Hoboken.

Liu, H., & Weng, Q. (2009). Scaling Effect On the Relationship Between Landscape Pattern and Land Surface Temperature. Photogrammetric engineering and remote sensing, 75(3), 291-304. doi: 10.14358/PERS.75.3.291.

Liu, L., & Zhang, Y. (2011). Urban Heat Island Analysis Using the Landsat TM Data and ASTER Data: A Case Study in Hong Kong. Remote Sensing, 3(7), 1535-1552. doi:10.3390/rs3071535.

Liu, M., & Tian, H. (2010). China's land cover and land use change from 1700 to 2005: Estimations from high-resolution satellite data and historical archives. Global Biogeochemical Cycles, 24(3), doi:10.1029/2009GB003687.

Liu, Z., Lai, J., Zhan, W., Bechtel, B., Voogt, J., Quan, J., . . . Li, J. (2022). Urban Heat Islands Significantly Reduced by COVID-19 Lockdown. Geophysical Research Letters, 49(2). doi:10.1029/2021GL096842.

Lu, L., Weng, Q., Xiao, D., Guo, H., Li, Q., & Hui, W. (2020). Spatiotemporal Variation of Surface Urban Heat Islands in Relation to Land Cover Composition and Configuration: A Multi-Scale Case Study of Xi'an, China. Remote Sens, 12(17), 2713. doi:10.3390/rs12172713.

Ma, Q., Wu, J., & He, C. (2016). A hierarchical analysis of the relationship between urban impervious surfaces and land surface temperatures: spatial scale dependence, temporal variations, and bioclimatic modulation. Landscape Ecology, 31(5), 1139–1153. doi:10.1007/s10980-016-0356-z.

Martin, M. A., Ghent, D., Pires, A. C., Göttsche, F.-M., Cermak, J., & Remedios, J. J. (2019). Comprehensive In Situ Validation of Five Satellite Land Surface Temperature Data Sets over Multiple Stations and Years. Remote Sensing, 11(5), 479, doi: 10.3390/rs11050479.

Masoudi, M., Tan, P. Y., & Liew, S. C. (2019). Multi-city comparison of the relationships between spatial pattern and cooling effect of urban green spaces in four major Asian cities. Ecological Indicators, 98, 200-213. doi:10.1016/j.ecolind.2018.09.058.

Memon, R. A., Leung, D. Y., & Chunho, L. (2008). A review on the generation, determination and mitigation of Urban Heat Island. Journal of Environmental Sciences, 20(1), 120-128.

Menon, J. S., & Sharma, R. (2021). Nature-Based Solutions for Co-mitigation of Air Pollution and Urban Heat in Indian Cities. Front. Sustain. Cities, 3(705185), 1-11. doi:10.3389/frsc.2021.705185.

Mirzaei, M., Verrelst, J., Arbabi, M., Shaklabadi, Z., & Lotfizadeh, M. (2020). Urban Heat Island Monitoring and Impacts on Citizen's General Health Status in Isfahan Metropolis: A Remote Sensing and Field Survey Approach. Remote Sens, 12(8), 1-17.

Monsefi, D., Taslim, S., & Shafaghat, A. (2015). Urban Design Guidelines to Mitigate Urban Heat Island (UHI) Effects In Hot- Dry Cities. Jurnal Teknologi, 74(4), 119-124, doi: 10.11113/jt.v74.4619.

Monteiro, M. V., Doick, K. J., Handley, P., & Peace, A. (2016). The impact of greenspace size on the extent of local nocturnal air temperature cooling in London. Urban Forestry & Urban Greening, 16, 160-169. doi:10.1016/j.ufug.2016.02.008.

National Center for Sustainable Transportation. (2018). Retrieved from Sustainable Mitigation of Stormwater Runoff Through Fully Permeable Pavement: . https://www.metrans.org/research/sustainable-mitigationstormwater-runoff-through-fully-permeable-pavement.

National Geographic Education, (2013). Geography Standard 4: the physical and human characteristics of places. Retrieved from NatGeoEd.org.

Ngie, A., Abutaleb, K., Ahmed, F., Darwish, A., & Ahmed, M. (2014). Assessment of urban heat island using satellite remotely sensed imagery: a review. South African Geographical Journal, 96(2), 198-214, doi: 10.1080/03736245.2014.924864.

OECD. (2022). Urban population by city size (indicator). (OECD, Producer) Retrieved July 4, 2022, from doi: 10.1787/b4332f92-en.

O'Malley, C., Piroozfarb, P. A., Farr, E. R., & Gates, J. (2014). An Investigation into Minimizing Urban Heat Island (UHI) Effects: A UK Perspective. Energy Procedia, 62, 72-80, doi: 10.1016/j.egypro.2014.12.368.

Oke, T. (1982). The energetic basis of the urban heat island. Quarterly Journal of the Royal Meteorological Society, 108, 1–24، doi:10.1002/qj.49710845502.

Oke, T. (1987). Boundary Layer Climates (Second ed.). New York: Routledge.

Oke, T. (2006). Towards Better Scientific Communication in Urban Climate. Theoretical and Applied Climatology, 84(1), 179-190, doi: 10.1007/s00704-005-0153-0.

Parida, B. R., Bar, S., Kaskaoutis, D., Pandey, A. C., Polade, S. D., & Goswami, S. (2021). Impact of COVID-19 induced lockdown on land surface temperature, aerosol, and urban heat in Europe and North America. Sustain Cities Soc., 75(103336). doi:10.1016/j.scs.2021.103336.

Peng, J., Xie, P., Liu, Y., & Ma, J. (2016). Urban thermal environment dynamics and associated landscape pattern factors: A case study in the Beijing metropolitan region,. Remote Sensing of Environment, 173, 145-155. doi:10.1016/j.rse.2015.11.027.

Ramaiah, M., & Avtar, R. (2019). Urban Green Spaces and Their Need in Cities of Rapidly Urbanizing India: A Review. Urban Sci., 3(3), 94. doi:10.3390/urbansci3030094

Ravanelli, R., Nascetti, A., Cirigliano, R., Rico, C., Monti, P., & Crespi, M. (2018). Monitoring urban heat island through google earth engine: potentialities and dificulties in different cities of the United States. The International Archives of the Photogrammetry, Remote Sensing and Spatial Information Sciences, XLII-3, 1467-1472, doi:10.5194/isprs-archives- XLII-3-1467-2018.

Ritchie, H., & Roser, M. (2018). Urbanization. Retrieved December 2021, from Urbanization: 'https://ourworldindata.org/urbanization'.

Rosenzweig, C., Solecki, W. D., Parshall, L., Chopping, M., Pope, G., & Goldberg, R. (2005). Characterizing the urban heat island in current and future climates in New Jersey. Global Environmental Change Part B: Environmental Hazards, 6(1), 51-62. doi:10.1016/j.hazards.2004.12.001.

Roth, M. (2013). Urban Heat Islands. In Handbook of Environmental Fluid Dynamics. (H. J. Fernando, Ed.) CRC Press/Taylor & Francis Group, LLC.

Sekertekin, A., & Bonafoni, a. S. (2020). Land Surface Temperature Retrieval from Landsat 5, 7, and 8 over Rural Areas: Assessment of Different Retrieval Algorithms and Emissivity Models and Toolbox Implementation. Remote Sensing, 12(2), 294, doi: 10.3390/rs12020294.

Secretariat of the Convention on Biological Diversity. (2016). Cities and Biodiversity Outlook. Retrieved January 2012, from http://www.cbd.int/en/subnational/partners- and-initiatives/cbo.

Singh, A., & Purohit, B. M. (2014). Public Health Impacts of Global Warming and Climate Change. Peace Review, 26(1), 112-120, DOI: 10.1080/10402659.2014.876326.

Singh, P., Kikon, N., & Verma, P. (2017). Impact of land use change and urbanization on urban heat island in Lucknow city, Central India. A remote sensing based estimate. Sustainable Cities and Society, 32(2210-6707), 100-114, doi:10.1016/j.scs.2017.02.018.

Small, C. (2001). stimation of urban vegetation abundance by spectral mixture analysis. International Journal of Remote Sensing, 22(7), 1305-1334. doi:10.1080/01431160151144369.

Soltani, A., & Sharifi, E. (2017). Daily variation of urban heat island effect and its correlations to urban greenery: A case study of Adelaide. Frontiers of Architectural Research, 6(4), 529-538.

Tomlinson, C., Chapman, L., Thornes, J., & Baker, C. (2011). Remote sensing land surface temperature for meteorology and climatology: A review . Meteorological Applications, 18(3), 296-306, doi: 10.1002/met.287.

Townsend, P. A., Lookingbill, T. R., Kingdon, C. C., & Gardner, R. H. (2009). Spatial pattern analysis for monitoring protected areas. Remote Sensing of Environment, 113(7), 1410-1420. doi:10.1016/j.rse.2008.05.023.

Tuholske, C., Caylor, K., Funka, C., Verdine, A., Sweeneya, S., Gracee, K., . . . Evansg, T. (2021). Global urban population exposure to extreme heat. National Academy of Sciences, 118(41), doi:10.1073/pnas.2024792118.

UN-Habitat, 2020. Annua Progress Report 2019, Nairobi, Kenya: UN-Habitat.

U.S. General Services Administration. (2011). Retrieved from "The Benefits and Challenges of Green Roofs on Public and Commercial: https://www.gsa.gov/cdnstatic/The_Benefits_and_Challenges_of_Green_Roofs_on_Public_and_Commercial_Buildings.pdf.

Vahmani, P., Jones, A. D., & Patricola, C. M. (2019). Interacting implications of climate change, population dynamics, and urban heat mitigation for future exposure to heat extremes. Environ. Res. Lett, 14(8), 1-10. doi:10.1088/1748-9326/ab28b0.

Vannier, C., Vasseur, C., Hubert-Moy, L., & Baudry, J. (2011). Multiscale ecological assessment of remote sensing images. Landscape Ecology, 26(8), 1053-1069. doi:10.1007/s10980-011-9626-y.

Vienna University of Technology. (2014). Development and Application of Mitigation and Adaptation Strate- gies and Measures for Counteracting the Global Urban Heat Islands Phenomenon. Vienna.

Villanueva-Solis, J. (2017). Urban Heat Island Mitigation and Urban Planning: The Case of the Mexicali, B. C. Mexico. American Journal of Climate Change, 6(1), doi:10.4236/ajcc.2017.61002.

Voogt, J., & Oke, T. (2003). Thermal remote sensing of urban climates. Remote Sensing of Environment, 86(3), 370-384, doi:10.1016/S0034-4257(03)00079-8.

Wai, C. Y., Muttil, N., Tariq, M. A., Paresi, P., Nnachi, R. C., & Ng, A. W. (2022). Investigating the Relationship between Human Activity and the Urban Heat Island Effect in Melbourne and Four Other International Cities Impacted by COVID-19. Sustainability, 14(1), 378, doi: 10.3390/su14010378.

Wang, C., Myint, S. W., Wang, Z., & Song, J. (2016). Spatio-Temporal Modeling of the Urban Heat Island in the Phoenix Metropolitan Area: Land Use Change Implications. Remote Sensing, 8(3), 185, doi: 10.3390/rs8030185.

Welch, R., Jordan, T., Lang, H., & Murakami, H. (1998). ASTER as a source for topographic data in the late 1990's. IEEE Transactions on Geoscience and Remote Sensing, 36(4), 1282-1289.

Wenga, Q., Lub, D., & Schubringa, J. (2004). Estimation of land surface temperature–vegetation abundance relationship. Remote Sensing of Environment, 89(4), 467 – 483.

WHO. (2017). Urban green spaces: a brief for action. Denmark: World Health Organisation. Retrieved from World Health Organisation.

WSP. (2019). Urban Heat Island Mitigation Plan. Sacramento, CA: Capital Region Transportation Sector. Retrieved from wsp.com/usa.

Wu, J. (2014). Urban ecology and sustainability: The state-of-the-science and future directions. Landscape and Urban Planning, 125(0169-2046), 209-221.

Yamamoto, Y. (2006, January). Measures to Mitigate Urban Heat Islands. Retrieved October 2017, from https://coolrooftoolkit.org/wp-content/uploads/2012/04/Measures-to-Mitigate-UHI-Yamamoto.pdf.

Yu, Z., Guo, X., Zeng, Y., Koga, M., & Vejre, H. (2018). Variations in land surface temperature and cooling efficiency of green space in rapid urbanization: The case of Fuzhou city, China. Urban Forestry & Urban Greening, 29, 113-121. doi:10.1016/j.ufug.2017.11.008.

Zhang, B., Xie, G.-d., Li, N., & Wang, S. (2015). Effect of urban green space changes on the role of rainwater runoff reduction in Beijing, China. Landscape and Urban Planning, 140, 8-16. doi:10.1016/j.landurbplan.2015.03.014.

Zhou, D., Xiao, J., Bonafoni, S., Berger, C., Deilami, K., Zhou, Y., . . . Sobrino, J. A. (2019). Satellite Remote Sensing of Surface Urban Heat Islands: Progress, Challenges, and Perspectives. Remote Sensing, 11(1), 1-36, doi: 10.3390/rs11010048.

APPENDIX 1

There is some important information about images which are used to calculate LST including time, mission, resolution, path and row, acquisition date, sun azimuth, sensor, and cloud cover of the records of images used to extract information for each selected test sites, Tehran, New York, Vienna, Washington, Helsinki, Quebec, Canberra, Palma, Latur, Niihama, Springfield, and Villach respectively.

Table 16. The records of images used to extract information for Tehran (Iran)

City	Landsat Scene Identifier	Time	Mission	Resolution	Path and Row	Acquisition date	Sun Azimuth angle	Sensor	Cloud Cover
Tehran	LC81640352021153LGN00	07:07:51	L8	30*30	164 × 35	2021-06-02	122,245866	OLI/TIRS	0,08
	LC81640352021169LGN00	07:07:57	L8	30*30	164 × 35	2021-06-18	118,689656	OLI/TIRS	5,94
	LC81640352021185LGN00	07:08:00	L8	30*30	164 × 35	2021-07-04	118,619094	OLI/TIRS	6,98
	LC81640352021201LGN00	07:08:03	L8	30*30	164 × 35	2021-07-20	122,059554	OLI/TIRS	4,53
	LC81640352021217LGN00	07:08:11	L8	30*30	164 × 35	2021-08-05	128,110981	OLI/TIRS	20,08
	LC81640352021233LGN00	07:08:16	L8	30*30	164 × 35	2021-08-21	135,471506	OLI/TIRS	48,34
	LC81650352021160LGN00	07:14:05	L8	30*30	165 × 35	2021-06-09	120,320808	OLI/TIRS	15,79
	LC81650352021176LGN00	07:14:09	L8	30*30	165 × 35	2021-06-25	118,199363	OLI/TIRS	0,53
	LC81650352021192LGN00	07:14:11	L8	30*30	165 × 35	2021-07-11	119,728912	OLI/TIRS	22,15
	LC81650352021208LGN00	07:14:18	L8	30*30	165 × 35	2021-07-27	124,463634	OLI/TIRS	5,84
	LC81650352021224LGN00	07:14:24	L8	30*30	165 × 35	2021-08-12	131,246660	OLI/TIRS	1,94
	LC81650352021240LGN00	07:14:29	L8	30*30	165 × 35	2021-08-28	138,785569	OLI/TIRS	0,17
	LE71640352005165ASN00	06:57:33	L7	30*30	164 × 35	2005-06-14	115,366679	ETM	37
	LE71640352005181ASN01	06:57:30	L7	30*30	164 × 35	2005-06-30	114,443825	ETM	15
	LE71640352005197ASN00	06:57:31	L7	30*30	164 × 35	2005-07-16	116,964976	ETM	78
	LE71640352005213ASN00	06:57:30	L7	30*30	164 × 35	2005-08-01	122,298734	ETM	43
	LE71640352005229ASN00	06:57:25	L7	30*30	164 × 35	2005-08-17	129,305599	ETM	0
	LE71650352005156ASN00	07:03:48	L7	30*30	165 × 35	2005-06-05	117,347062	ETM	12
	LE71650352005172ASN00	07:03:42	L7	30*30	165 × 35	2005-06-21	114,526055	ETM	19

	LE71650352005188ASN00	07:03:42	L7	30*30	165 × 35	2005-07-07	115,141790	ETM	22
	LE71650352005204ASN00	07:03:42	L7	30*30	165 × 35	2005-07-23	119,017908	ETM	6
	LE71650352005220ASN00	07:03:39	L7	30*30	165 × 35	2005-08-08	125,226425	ETM	8
	LE71650352005236ASN00	07:03:33	L7	30*30	165 × 35	2005-08-24	132,601591	ETM	4
	LT51640351990164RSA00	06:28:16	L5	30*30	164 × 35	1990-06-13	107,150932	TM	5
	LT51640351990196RSA01	06:28:12	L5	30*30	164 × 35	1990-07-15	108,307459	TM	18
	LT51640351990212ISP00	06:28:08	L5	30*30	164 × 35	1990-07-31	112,994488	TM	49
	LT51640351990228RSA00	06:28:03	L5	30*30	164 × 35	1990-08-16	119,481889	TM	28
	LT51650351990155RSA00	06:34:27	L5	30*30	165 × 35	1990-06-04	108,922455	TM	1
	LT51650351990171RSA00	06:34:26	L5	30*30	165 × 35	1990-06-20	106,373857	TM	18
	LT51650351990203RSA00	06:34:20	L5	30*30	165 × 35	1990-07-22	110,078163	TM	36
	LT51650351990219ISP00	06:34:16	L5	30*30	165 × 35	1990-08-07	115,668639	TM	14
	LT51650351990235RSA02	06:34:11	L5	30*30	165 × 35	1990-08-23	122,625984	TM	3

Table 17. The records of images used to extract information for New York (US)

City	Landsat Scene Identifier	Time	Mission	Resolution	Path and Row	Acquisition date	Sun Azimuth angle	Sensor	Cloud Cover
NewYork	LC80130322021167LGN00	15:33:32	L8	30*30	13 × 32	2021-06-16	128,913561	OLI/TIRS	7,46
	LC80130322021199LGN00	15:33:37	L8	30*30	13 × 32	2021-07-18	130,362770	OLI/TIRS	36,95
	LC80130322021231LGN00	15:33:51	L8	30*30	13 × 32	2021-08-19	140,885564	OLI/TIRS	83,38
	LC80140312021158LGN00	15:39:15	L8	30*30	14 × 31	2021-06-07	133,524325	OLI/TIRS	6,88
	LC80140312021174LGN00	15:39:20	L8	30*30	14 × 31	2021-06-23	131,240848	OLI/TIRS	23,89
	LC80140312021190LGN00	15:39:22	L8	30*30	14 × 31	2021-07-09	131,627756	OLI/TIRS	88,73
	LC80140312021206LGN00	15:39:28	L8	30*30	14 × 31	2021-07-25	134,668989	OLI/TIRS	90,58
	LC80140312021222LGN00	15:39:35	L8	30*30	14 × 31	2021-08-10	139,575827	OLI/TIRS	8,29
	LC80140312021238LGN00	15:39:40	L8	30*30	14 × 31	2021-08-26	145,327387	OLI/TIRS	15,1
	LC80140322021158LGN00	15:39:39	L8	30*30	14 × 32	2021-06-07	130,561647	OLI/TIRS	24,54
	LC80140322021174LGN00	15:39:44	L8	30*30	14 × 32	2021-06-23	128,212628	OLI/TIRS	14,26
	LC80140322021190LGN00	15:39:46	L8	30*30	14 × 32	2021-07-09	128,771286	OLI/TIRS	59,57
	LC80140322021206LGN00	15:39:52	L8	30*30	14 × 32	2021-07-25	132,145149	OLI/TIRS	66,5
	LC80140322021222LGN00	15:39:59	L8	30*30	14 × 32	2021-08-10	137,458514	OLI/TIRS	68,36
	LC80140322021238LGN00	15:40:03	L8	30*30	14 × 32	2021-08-26	143,619070	OLI/TIRS	8,84
	LT50130322005155GNC01	15:21:09	L5	30*30	13 × 32	2005-06-04	126,188332	TM	85
	LT50130322005171GNC01	15:21:15	L5	30*30	13 × 32	2005-06-20	123,508931	TM	32
	LT50130322005203EDC00	15:21:32	L5	30*30	13 × 32	2005-07-22	126,541330	TM	17
	LT50130322005219GNC01	15:21:41	L5	30*30	13 × 32	2005-08-07	131,601945	TM	54
	LT50130322005235GNC02	15:21:46	L5	30*30	13 × 32	2005-08-23	137,787832	TM	4
	LT50140312005162GNC01	15:26:59	L5	30*30	14 × 31	2005-06-11	127,626985	TM	45
	LT50140312005178GNC01	15:27:04	L5	30*30	14 × 31	2005-06-27	126,088692	TM	21
	LT50140312005194GNC01	15:27:12	L5	30*30	14 × 31	2005-07-13	127,267056	TM	80
	LT50140312005210GNC01	15:27:23	L5	30*30	14 × 31	2005-07-29	130,945353	TM	73
	LT50140312005226GNC01	15:27:30	L5	30*30	14 × 31	2005-08-14	136,258839	TM	8
	LT50140322005162GNC01	15:27:23	L5	30*30	14 × 32	2005-06-11	124,712478	TM	48
	LT50140322005178GNC01	15:27:28	L5	30*30	14 × 32	2005-06-27	123,166317	TM	94
	LT50140322005194GNC01	15:27:36	L5	30*30	14 × 32	2005-07-13	124,559188	TM	85
	LT50140322005210GNC01	15:27:47	L5	30*30	14 × 32	2005-07-29	128,549941	TM	66

	LT50140322005226GNC01	15:27:54	L5	30*30	14 × 32	2005-08-14	134,233430	TM	3
	LT50130321990178PAC04	14:53:51	L5	30*30	13 × 32	1990-06-27	114,091415	TM	61
	LT50130321990210XXX03	14:53:44	L5	30*30	13 × 32	1990-07-29	119,242742	TM	86
	LT50130321990226XXX03	14:53:39	L5	30*30	13 × 32	1990-08-14	124,797264	TM	35
	LT50140311990153PAC04	14:59:39	L5	30*30	14 × 31	1990-06-02	119,784912	TM	12
	LT50140311990169PAC04	14:59:38	L5	30*30	14 × 31	1990-06-18	117,147088	TM	88
	LT50140311990185XXX03	14:59:36	L5	30*30	14 × 31	1990-07-04	116,875339	TM	13
	LT50140311990201XXX01	14:59:32	L5	30*30	14 × 31	1990-07-20	119,182914	TM	28
	LT50140321990153PAC04	15:00:02	L5	30*30	14 × 32	1990-06-02	117,227510	TM	6
	LT50140321990169PAC04	15:00:02	L5	30*30	14 × 32	1990-06-18	114,530477	TM	46
	LT50140321990185XXX03	15:00:00	L5	30*30	14 × 32	1990-07-04	114,341422	TM	5
	LT50140321990201XXX01	14:59:56	L5	30*30	14 × 32	1990-07-20	116,833545	TM	2
	LT50140321990217XXX03	14:59:52	L5	30*30	14 × 32	1990-08-05	121,508772	TM	99

Table 18. The records of images used to extract information for Vienna (Austria)

City	Landsat Scene Identifier	Time	Mission	Resolution	Path and Row	Acquisition date	Sun Azimuth angle	Sensor	Cloud Cover
Vienna	LC81890262021152LGN00	09:38:46	L8	30*30	189 × 26	2021-06-01	147,190824	OLI/TIRS	44,04
	LC81890262021168LGN00	09:38:52	L8	30*30	189 × 26	2021-06-17	144,869683	OLI/TIRS	8,51
	LC81890262021184LGN00	09:38:55	L8	30*30	189 × 26	2021-07-03	143,907824	OLI/TIRS	54,26
	LC81890262021200LGN00	09:38:58	L8	30*30	189 × 26	2021-07-19	144,837838	OLI/TIRS	27,57
	LC81890262021216LGN00	09:39:06	L8	30*30	189 × 26	2021-08-04	147,522003	OLI/TIRS	95,49
	LC81890262021232LGN00	09:39:11	L8	30*30	189 × 26	2021-08-20	151,322339	OLI/TIRS	69,58
	LC81890272021152LGN00	09:39:10	L8	30*30	189 × 27	2021-06-01	144,990487	OLI/TIRS	29,03
	LC81890272021168LGN00	09:39:16	L8	30*30	189 × 27	2021-06-17	142,526814	OLI/TIRS	0,28
	LC81890272021184LGN00	09:39:19	L8	30*30	189 × 27	2021-07-03	141,596759	OLI/TIRS	27,47
	LC81890272021200LGN00	09:39:22	L8	30*30	189 × 27	2021-07-19	142,715265	OLI/TIRS	56,27
	LC81890272021216LGN00	09:39:30	L8	30*30	189 × 27	2021-08-04	145,679832	OLI/TIRS	97,94
	LC81890272021232LGN00	09:39:35	L8	30*30	189 × 27	2021-08-20	149,784116	OLI/TIRS	54,31
	LC81900262021159LGN00	09:45:00	L8	30*30	190 × 26	2021-06-08	146,074742	OLI/TIRS	31,92
	LC81900262021175LGN00	09:45:05	L8	30*30	190 × 26	2021-06-24	144,234882	OLI/TIRS	24,32
	LC81900262021191LGN00	09:45:07	L8	30*30	190 × 26	2021-07-10	144,074288	OLI/TIRS	4,26
	LC81900262021207LGN00	09:45:13	L8	30*30	190 × 26	2021-07-26	145,830079	OLI/TIRS	16,08
	LC81900262021223LGN00	09:45:20	L8	30*30	190 × 26	2021-08-11	149,088540	OLI/TIRS	14,78
	LC81900272021159LGN00	09:45:24	L8	30*30	190 × 27	2021-06-08	143,791797	OLI/TIRS	27,79
	LC81900272021175LGN00	09:45:29	L8	30*30	190 × 27	2021-06-24	141,883054	OLI/TIRS	2,03
	LC81900272021191LGN00	09:45:30	L8	30*30	190 × 27	2021-07-10	141,828831	OLI/TIRS	7,1
	LC81900272021207LGN00	09:45:37	L8	30*30	190 × 27	2021-07-26	143,824204	OLI/TIRS	14,86
	LC81900272021223LGN00	09:45:43	L8	30*30	190 × 27	2021-08-11	147,379743	OLI/TIRS	9,02
	LC81900272021239LGN00	09:45:48	L8	30*30	190 × 27	2021-08-27	151,741971	OLI/TIRS	90,06
	LT51890262005156KIS00	09:26:29	L5	30*30	189 × 26	2005-06-05	141,414894	TM	75
	LT51890262005172KIS00	09:26:36	L5	30*30	189 × 26	2005-06-21	139,363282	TM	5
	LT51890262005188KIS00	09:26:40	L5	30*30	189 × 26	2005-07-07	138,947651	TM	44
	LT51890262005204KIS00	09:26:53	L5	30*30	189 × 26	2005-07-23	140,530587	TM	95
	LT51890262005220MTI01	09:27:01	L5	30*30	189 × 26	2005-08-08	143,755691	TM	86
	LT51890272005156KIS00	09:26:53	L5	30*30	189 × 27	2005-06-05	139,123513	TM	92

	LT51890272005172KIS00	09:27:00	L5	30*30	189 × 27	2005-06-21	136,969130	TM	3
	LT51890272005188KIS00	09:27:04	L5	30*30	189 × 27	2005-07-07	136,647950	TM	49
	LT51890272005204KIS00	09:27:16	L5	30*30	189 × 27	2005-07-23	138,434019	TM	87
	LT51890272005220KIS00	09:27:25	L5	30*30	189 × 27	2005-08-08	141,946361	TM	51
	LT51890272005236KIS00	09:27:31	L5	30*30	189 × 27	2005-08-24	146,434907	TM	93
	LT51900262005179KIS00	09:32:48	L5	30*30	190 × 26	2005-06-28	138,930455	TM	16
	LT51900262005195KIS00	09:32:57	L5	30*30	190 × 26	2005-07-14	139,399638	TM	37
	LT51900262005211KIS00	09:33:08	L5	30*30	190 × 26	2005-07-30	141,777302	TM	2
	LT51900272005163KIS00	09:33:07	L5	30*30	190 × 27	2005-06-12	138,003709	TM	91
	LT51900272005179KIS00	09:33:12	L5	30*30	190 × 27	2005-06-28	136,566046	TM	31
	LT51900272005195KIS00	09:33:21	L5	30*30	190 × 27	2005-07-14	137,179194	TM	42
	LT51900272005211KIS00	09:33:32	L5	30*30	190 × 27	2005-07-30	139,804746	TM	3
	LT51890261990163FUI00	08:59:12	L5	30*30	189 × 26	1990-06-12	130,053529	TM	24
	LT51890261990179FUI00	08:59:11	L5	30*30	189 × 26	1990-06-28	128,701561	TM	23
	LT51890261990195FUI05	08:59:09	L5	30*30	189 × 26	1990-07-14	129,345959	TM	47
	LT51890261990211FUI00	08:59:04	L5	30*30	189 × 26	1990-07-30	131,926500	TM	4
	LT51890261990227FUI00	08:59:00	L5	30*30	189 × 26	1990-08-15	135,913633	TM	6
	LT51890271990163FUI00	08:59:36	L5	30*30	189 × 27	1990-06-12	127,725290	TM	30
	LT51890271990179FUI00	08:59:35	L5	30*30	189 × 27	1990-06-28	126,399049	TM	25
	LT51890271990195FUI05	08:59:33	L5	30*30	189 × 27	1990-07-14	127,151371	TM	26
	LT51890271990211FUI00	08:59:28	L5	30*30	189 × 27	1990-07-30	129,946536	TM	1
	LT51890271990227FUI00	08:59:24	L5	30*30	189 × 27	1990-08-15	134,211167	TM	6
	LT51900261990170FUI00	09:05:22	L5	30*30	190 × 26	1990-06-19	129,246671	TM	16
	LT51900261990186FUI01	09:05:20	L5	30*30	190 × 26	1990-07-05	128,738931	TM	35
	LT51900261990202FUI00	09:05:15	L5	30*30	190 × 26	1990-07-21	130,250900	TM	26
	LT51900261990218FUI00	09:05:12	L5	30*30	190 × 26	1990-08-06	133,532825	TM	65
	LT51900261990234FUI00	09:05:08	L5	30*30	190 × 26	1990-08-22	137,948736	TM	88
	LT51900271990154FUI00	09:05:47	L5	30*30	190 × 27	1990-06-03	129,183060	TM	63
	LT51900271990170FUI00	09:05:46	L5	30*30	190 × 27	1990-06-19	126,902372	TM	9
	LT51900271990186FUI01	09:05:44	L5	30*30	190 × 27	1990-07-05	126,457512	TM	7
	LT51900271990202FUI00	09:05:39	L5	30*30	190 × 27	1990-07-21	128,142405	TM	11
	LT51900271990218FUI00	09:05:36	L5	30*30	190 × 27	1990-08-06	131,662334	TM	37

Table 19. The records of images used to extract information for Washington D.C, (US)

City	Landsat Scene Identifier	Time	Mission	Resolution	Path and Row	Acquisition date	Sun Azimuth angle	Sensor	Cloud Cover
Washington	LC80150332021165LGN00	15:46:17	L8	30*30	15 × 33	2021-06-14	126,031650	OLI/TIRS	23,53
	LC80150332021181LGN00	15:46:20	L8	30*30	15 × 33	2021-06-30	124,961769	OLI/TIRS	7,36
	LC80150332021197LGN00	15:46:22	L8	30*30	15 × 33	2021-07-16	127,084529	OLI/TIRS	3,92
	LC80150332021229LGN00	15:46:36	L8	30*30	15 × 33	2021-08-17	138,087203	OLI/TIRS	96,24
	LT50150332005153GNC01	15:33:53	L5	30*30	15 × 33	2005-06-02	123,722860	TM	96
	LT50150332005169GNC01	15:34:00	L5	30*30	15 × 33	2005-06-18	120,657644	TM	16
	LT50150332005185GNC01	15:34:04	L5	30*30	15 × 33	2005-07-04	120,471557	TM	24
	LT50150332005217GNC01	15:34:25	L5	30*30	15 × 33	2005-08-05	128,570185	TM	3
	LT50150332005233GNC02	15:34:31	L5	30*30	15 × 33	2005-08-21	135,066962	TM	21
	LT50150331990160XXX03	15:06:37	L5	30*30	15 × 33	1990-06-09	113,139670	TM	69
	LT50150331990192XXX03	15:06:34	L5	30*30	15 × 33	1990-07-11	112,637709	TM	58
	LT50150331990224XXX04	15:06:26	L5	30*30	15 × 33	1990-08-12	122,029221	TM	0
	LT50150331990240XXX03	15:06:19	L5	30*30	15 × 33	1990-08-28	128,647900	TM	32

Table 20. The records of images used to extract information for Helsinki (Finland)

City	Landsat Scene Identifier	Time	Mission	Resolution	Path and Row	Acquisition date	Sun Azimuth angle	Sensor	Cloud Cover
Helsinki	LC81870182021154LGN00	09:23:14	L8	30*30	187 × 18	2021-06-03	161,990310	OLI/TIRS	56,04
	LC81870182021170LGN00	09:23:20	L8	30*30	187 × 18	2021-06-19	160,552746	OLI/TIRS	0,94
	LC81870182021186LGN00	09:23:23	L8	30*30	187 × 18	2021-07-05	159,617531	OLI/TIRS	9,44
	LC81870182021202LGN00	09:23:26	L8	30*30	187 × 18	2021-07-21	159,693031	OLI/TIRS	36,7
	LC81870182021218LGN00	09:23:34	L8	30*30	187 × 18	2021-08-06	160,910924	OLI/TIRS	6,36
	LC81870182021234LGN00	09:23:39	L8	30*30	187 × 18	2021-08-22	163,002417	OLI/TIRS	80,57
	LC81880182021161LGN00	09:29:28	L8	30*30	188 × 18	2021-06-10	161,345391	OLI/TIRS	8,67
	LC81880182021177LGN00	09:29:32	L8	30*30	188 × 18	2021-06-26	160,045359	OLI/TIRS	29,66
	LC81880182021193LGN00	09:29:34	L8	30*30	188 × 18	2021-07-12	159,504402	OLI/TIRS	2,84
	LC81880182021225LGN00	09:29:47	L8	30*30	188 × 18	2021-08-13	161,737763	OLI/TIRS	5,72
	LC81880182021241LGN00	09:29:52	L8	30*30	188 × 18	2021-08-29	164,082654	OLI/TIRS	63,3
	LC81890182021152LGN00	09:35:35	L8	30*30	189 × 18	2021-06-01	162,167574	OLI/TIRS	27,51
	LC81890182021168LGN00	09:35:41	L8	30*30	189 × 18	2021-06-17	160,717013	OLI/TIRS	17,09
	LC81890182021184LGN00	09:35:44	L8	30*30	189 × 18	2021-07-03	159,686470	OLI/TIRS	1,64
	LC81890182021200LGN00	09:35:47	L8	30*30	189 × 18	2021-07-19	159,618186	OLI/TIRS	43,6
	LC81890182021216LGN00	09:35:55	L8	30*30	189 × 18	2021-08-04	160,704326	OLI/TIRS	45,58
	LC81890182021232LGN00	09:36:00	L8	30*30	189 × 18	2021-08-20	162,707856	OLI/TIRS	50,49
	LT51870182005158KIS00	09:10:57	L5	30*30	187 × 18	2005-06-07	157,142405	TM	48
	LT51870182005174KIS00	09:11:03	L5	30*30	187 × 18	2005-06-23	155,753050	TM	41
	LT51870182005190KIS00	09:11:09	L5	30*30	187 × 18	2005-07-09	155,090035	TM	17
	LT51870182005206KIS00	09:11:21	L5	30*30	187 × 18	2005-07-25	155,609200	TM	33
	LT51870182005238KIS00	09:11:34	L5	30*30	187 × 18	2005-08-26	159,683637	TM	83
	LT51880182005165KIS00	09:17:11	L5	30*30	188 × 18	2005-06-14	156,479785	TM	80
	LT51880182005181KIS00	09:17:16	L5	30*30	188 × 18	2005-06-30	155,336304	TM	77
	LT51880182005197KIS00	09:17:26	L5	30*30	188 × 18	2005-07-16	155,164564	TM	11
	LT51880182005213KIS00	09:17:36	L5	30*30	188 × 18	2005-08-01	156,207138	TM	55
	LT51880182005229KIS00	09:17:43	L5	30*30	188 × 18	2005-08-17	158,241509	TM	32
	LT51890182005156KIS00	09:23:18	L5	30*30	189 × 18	2005-06-05	157,350609	TM	87
	LT51890182005172KIS00	09:23:24	L5	30*30	189 × 18	2005-06-21	155,889690	TM	55

	LT51890182005188KIS00	09:23:29	L5	30*30	189 × 18	2005-07-07	155,115260	TM	54
	LT51890182005204KIS00	09:23:41	L5	30*30	189 × 18	2005-07-23	155,479158	TM	88
	LT51890182005236KIS00	09:23:56	L5	30*30	189 × 18	2005-08-24	159,356803	TM	29
	LT51870181990165KIS00	08:43:38	L5	30*30	187 × 18	1990-06-14	146,855784	TM	88
	LT51870181990181KIS00	08:43:38	L5	30*30	187 × 18	1990-06-30	145,721114	TM	10
	LT51870181990197KIS00	08:43:34	L5	30*30	187 × 18	1990-07-16	145,706791	TM	60
	LT51870181990213KIS00	08:43:30	L5	30*30	187 × 18	1990-08-01	146,996217	TM	65
	LT51870181990229KIS03	08:43:26	L5	30*30	187 × 18	1990-08-17	149,365768	TM	25
	LT51880181990156KIS00	08:49:50	L5	30*30	188 × 18	1990-06-05	147,785239	TM	100
	LT51880181990172KIS00	08:49:49	L5	30*30	188 × 18	1990-06-21	146,252909	TM	11
	LT51880181990188KIS00	08:49:48	L5	30*30	188 × 18	1990-07-07	145,561143	TM	98
	LT51880181990204KIS00	08:49:43	L5	30*30	188 × 18	1990-07-23	146,117340	TM	44
	LT51880181990220KIS00	08:49:39	L5	30*30	188 × 18	1990-08-08	147,920775	TM	14
	LT51880181990236KIS00	08:49:33	L5	30*30	188 × 18	1990-08-24	150,615825	TM	66
	LT51890181990163KIS00	08:56:01	L5	30*30	189 × 18	1990-06-12	147,043582	TM	25
	LT51890181990179KIS00	08:56:00	L5	30*30	189 × 18	1990-06-28	145,806337	TM	91
	LT51890181990195KIS00	08:55:57	L5	30*30	189 × 18	1990-07-14	145,637464	TM	73
	LT51890181990211KIS00	08:55:53	L5	30*30	189 × 18	1990-07-30	146,764895	TM	94
	LT51890181990227KIS00	08:55:48	L5	30*30	189 × 18	1990-08-15	149,019363	TM	8

Table 21. The records of images used to extract information for Quebec (Canada)

City	Landsat Scene Identifier	Time	Mission	Resolution	Path and Row	Acquisition date	Sun Azimuth angle	Sensor	Cloud Cover
Quebec	LC80130272021167LGN00	15:31:32	L8	30*30	13 × 27	2021-06-16	142,609822	OLI/TIRS	79,08
	LC80130272021183LGN00	15:31:35	L8	30*30	13 × 27	2021-07-02	141,589862	OLI/TIRS	39,47
	LC80130272021199LGN00	15:31:38	L8	30*30	13 × 27	2021-07-18	142,610888	OLI/TIRS	76,93
	LC80130272021215LGN00	15:31:46	L8	30*30	13 × 27	2021-08-03	145,503479	OLI/TIRS	82,66
	LC80130272021231LGN00	15:31:52	L8	30*30	13 × 27	2021-08-19	149,570994	OLI/TIRS	53,23
	LC80130282021167LGN00	15:31:56	L8	30*30	13 × 28	2021-06-16	140,149176	OLI/TIRS	49,81
	LC80130282021183LGN00	15:31:59	L8	30*30	13 × 28	2021-07-02	139,160450	OLI/TIRS	95,27
	LC80130282021199LGN00	15:32:02	L8	30*30	13 × 28	2021-07-18	140,382367	OLI/TIRS	93,76
	LC80130282021215LGN00	15:32:10	L8	30*30	13 × 28	2021-08-03	143,574010	OLI/TIRS	14,52
	LC80130282021231LGN00	15:32:15	L8	30*30	13 × 28	2021-08-19	147,966877	OLI/TIRS	90,07
	LC80140272021158LGN00	15:37:40	L8	30*30	14 × 27	2021-06-07	143,908924	OLI/TIRS	14,35
	LC80140272021174LGN00	15:37:45	L8	30*30	14 × 27	2021-06-23	141,930610	OLI/TIRS	72,44
	LC80140272021190LGN00	15:37:47	L8	30*30	14 × 27	2021-07-09	141,779029	OLI/TIRS	77,69
	LC80140272021206LGN00	15:37:53	L8	30*30	14 × 27	2021-07-25	143,683989	OLI/TIRS	80,57
	LC80140272021222LGN00	15:38:00	L8	30*30	14 × 27	2021-08-10	147,183010	OLI/TIRS	42,39
	LC80140272021238LGN00	15:38:04	L8	30*30	14 × 27	2021-08-26	151,524998	OLI/TIRS	55,08
	LT50130272005155GNC01	15:19:09	L5	30*30	13 × 27	2005-06-04	139,242677	TM	85
	LT50130272005171GNC01	15:19:16	L5	30*30	13 × 27	2005-06-20	137,029490	TM	17
	LT50130272005187GNC01	15:19:20	L5	30*30	13 × 27	2005-07-08	136,600798	TM	1
	LT50130272005203GNC01	15:19:32	L5	30*30	13 × 27	2005-07-22	138,304740	TM	28
	LT50130272005219GNC01	15:19:41	L5	30*30	13 × 27	2005-08-07	141,744189	TM	20
	LT50130282005155GNC01	15:19:33	L5	30*30	13 × 28	2005-06-04	136,859801	TM	40
	LT50130282005171GNC01	15:19:40	L5	30*30	13 × 28	2005-06-20	134,551290	TM	3
	LT50130282005187GNC01	15:19:44	L5	30*30	13 × 28	2005-07-06	134,202966	TM	45
	LT50130282005203GNC01	15:19:56	L5	30*30	13 × 28	2005-07-22	136,126786	TM	52
	LT50130282005219GNC01	15:20:05	L5	30*30	13 × 28	2005-08-07	139,860668	TM	7
	LT50140272005162GNC01	15:25:23	L5	30*30	14 × 27	2005-06-11	138,104653	TM	13
	LT50140272005178GNC01	15:25:28	L5	30*30	14 × 27	2005-06-27	136,584765	TM	1
	LT50140272005194GNC01	15:25:37	L5	30*30	14 × 27	2005-07-13	137,101336	TM	35

	LT50140272005210GNC01	15:25:48	L5	30*30	14 × 27	2005-07-29	139,638452	TM	83
	LT50140272005226GNC01	15:25:55	L5	30*30	14 × 27	2005-08-14	143,622137	TM	70
	LT50130271990162PAC03	14:51:52	L5	30*30	13 × 27	1990-06-11	127,878874	TM	80
	LT50130271990194PAC02	14:51:49	L5	30*30	13 × 27	1990-07-13	127,123636	TM	11
	LT50130271990210PAC02	14:51:44	L5	30*30	13 × 27	1990-07-29	129,817517	TM	5
	LT50130271990226PAC02	14:51:40	L5	30*30	13 × 27	1990-08-14	134,017994	TM	46
	LT50130281990162PAC05	14:52:16	L5	30*30	13 × 28	1990-06-11	125,506990	TM	94
	LT50130281990194PAC04	14:52:13	L5	30*30	13 × 28	1990-07-13	124,882411	TM	3
	LT50130281990210XXX03	14:52:08	L5	30*30	13 × 28	1990-07-29	127,793429	TM	1
	LT50130281990226PAC04	14:52:04	L5	30*30	13 × 28	1990-08-14	132,255266	TM	87
	LT50140271990153PAC02	14:58:03	L5	30*30	14 × 27	1990-06-02	129,378489	TM	70
	LT50140271990169PAC02	14:58:02	L5	30*30	14 × 27	1990-06-18	127,021316	TM	79
	LT50140271990201PAC02	14:57:56	L5	30*30	14 × 27	1990-07-20	128,074652	TM	88
	LT50140271990233PAC03	14:57:48	L5	30*30	14 × 27	1990-08-21	136,137924	TM	4

Table 22. The records of images used to extract information for Canberra (Australia)

City	Landsat Scene Identifier	Time	Mission	Resolution	Path and Row	Acquisition date	Sun Azimuth angle	Sensor	Cloud Cover
Canberra	LC80900842021018LGN00	23:50:26	L8	30*30	90 × 84	2021-01-18	74,54598710	OLI/TIRS	39,68
	LC80900842021034LGN00	23:50:25	L8	30*30	90 × 84	2021-02-03	69,47608719	OLI/TIRS	10,08
	LC80900842021050LGN00	23:50:20	L8	30*30	90 × 84	2021-02-19	62,88944881	OLI/TIRS	3,82
	LC80900852021018LGN00	23:50:50	L8	30*30	90 × 85	2021-01-18	72,82205922	OLI/TIRS	4,7
	LC80900852021034LGN00	23:50:49	L8	30*30	90 × 85	2021-02-03	68,03025617	OLI/TIRS	16,8
	LC80900852021050LGN00	23:50:44	L8	30*30	90 × 85	2021-02-19	61,73695429	OLI/TIRS	3,95
	LC80910842021009LGN00	23:56:41	L8	30*30	91 × 84	2021-01-09	76,34763687	OLI/TIRS	0,16
	LC80910842021025LGN00	23:56:37	L8	30*30	91 × 84	2021-01-25	72,57961341	OLI/TIRS	92,6
	LC80910842021041LGN00	23:56:34	L8	30*30	91 × 84	2021-02-10	66,72034626	OLI/TIRS	0,56
	LC80910842021057LGN00	23:56:28	L8	30*30	91 × 84	2021-02-26	59,77901288	OLI/TIRS	32,05
	LC80910852021009LGN00	23:57:05	L8	30*30	91 × 85	2021-01-09	74,48164070	OLI/TIRS	1,38
	LC80910852021041LGN00	23:56:58	L8	30*30	91 × 85	2021-02-10	65,40280068	OLI/TIRS	13,27
	LC80910852021057LGN00	23:56:52	L8	30*30	91 × 85	2021-02-26	58,75318715	OLI/TIRS	74,92
	LC80900842021338LGN00	23:50:39	L8	30*30	90 × 84	2021-12-04	73,06249576	OLI/TIRS	84,25
	LC80900842021354LGN00	23:50:37	L8	30*30	90 × 84	2021-12-20	76,71117283	OLI/TIRS	0,74
	LC80900852021354LGN00	23:51:01	L8	30*30	90 × 85	2021-12-20	74,61743084	OLI/TIRS	6,08
	LC80910842021345LGN00	23:56:49	L8	30*30	91 × 84	2021-12-11	75,06940574	OLI/TIRS	4,97
	LC80910842021361LGN00	23:56:44	L8	30*30	91 × 84	2021-12-27	77,21284522	OLI/TIRS	33,04
	LC80910852021345LGN00	23:57:13	L8	30*30	91 × 85	2021-12-11	72,94478605	OLI/TIRS	26,65
	LC80910852021361LGN00	23:57:08	L8	30*30	91 × 85	2021-12-27	75,17861641	OLI/TIRS	14,33
	LE70900842005014ASN00	23:39:42	L7	30*30	90 × 84	2005-01-14	77,89287810	TM	22
	LE70900842005030ASA00	23:39:45	L7	30*30	90 × 84	2005-01-30	73,41709126	TM	34
	LE70900842005046ASN00	23:39:54	L7	30*30	90 × 84	2005-02-15	67,32360956	TM	19
	LE70900852005014ASN00	23:40:05	L7	30*30	90 × 85	2005-01-14	76,23281303	TM	27
	LE70900852005030ASA00	23:40:08	L7	30*30	90 × 85	2005-01-30	71,98690456	TM	6
	LE70900852005046ASN00	23:40:18	L7	30*30	90 × 85	2005-02-15	66,15488782	TM	46
	LE70910842005005ASN00	23:45:51	L7	30*30	91 × 84	2005-01-05	79,25566301	TM	23
	LE70910842005021ASN00	23:45:52	L7	30*30	91 × 84	2005-01-21	76,24350078	TM	0
	LE70910842005037ASN00	23:46:00	L7	30*30	91 × 84	2005-02-06	70,94941679	TM	1

	LE70910842005053ASN01	23:46:07	L7	30*30	91 × 84	2005-02-22	64,31161224	TM	3
	LE70910852005005ASN00	23:46:15	L7	30*30	91 × 85	2005-01-05	77,47540899	TM	43
	LE70910852005021ASN00	23:46:16	L7	30*30	91 × 85	2005-01-21	74,67650599	TM	0
	LE70910852005037ASN00	23:46:24	L7	30*30	91 × 85	2005-02-06	69,63463045	TM	13
	LE70910852005053ASN01	23:46:31	L7	30*30	91 × 85	2005-02-22	63,25328070	TM	1
	LE70900842005350ASN00	23:39:55	L7	30*30	90 × 84	2005-12-16	78,58566632	TM	11
	LE70900852005350ASN00	23:40:19	L7	30*30	90 × 85	2005-12-16	76,62451372	TM	26
	LE70910842005341ASN00	23:46:05	L7	30*30	91 × 84	2005-12-07	76,63400592	TM	0
	LE70910842005357ASN00	23:46:08	L7	30*30	91 × 84	2005-12-23	79,39567975	TM	87
	LE70910852005341ASN00	23:46:29	L7	30*30	91 × 85	2005-12-07	74,66299774	TM	15
	LE70910852005357ASN00	23:46:32	L7	30*30	91 × 85	2005-12-23	77,47582844	TM	48
	LT50900841990045ASA00	23:11:47	L5	30*30	90 × 84	1990-02-14	73,78267424	TM	64
	LT50900851990045ASA00	23:12:11	L5	30*30	90 × 85	1990-02-14	72,74641794	TM	75
	LT50910841990052ASA00	23:17:46	L5	30*30	91 × 84	1990-02-21	71,02614518	TM	69
	LT50910851990052ASA00	23:18:09	L5	30*30	91 × 85	1990-02-21	70,08179448	TM	54
	LT50900841990349ASA00	23:09:42	L5	30*30	90 × 84	1990-12-15	83,98735796	TM	25
	LT50900851990349ASA00	23:10:06	L5	30*30	90 × 85	1990-12-15	82,38539235	TM	46
	LT50910841990340ASA00	23:15:43	L5	30*30	91 × 84	1990-12-06	82,22870892	TM	3
	LT50910841990356ASA00	23:16:04	L5	30*30	91 × 84	1990-12-22	84,74101659	TM	3
	LT50910851990340ASA00	23:16:07	L5	30*30	91 × 85	1990-12-06	80,61698866	TM	38
	LT50910851990356ASA00	23:16:28	L5	30*30	91 × 85	1990-12-22	83,16968265	TM	27

Table 23. The records of images used to extract information for Palma (Spain)

City	Landsat Scene Identifier	Time	Mission	Resolution	Path and Row	Acquisition date	Sun Azimuth angle	Sensor	Cloud Cover
Palma	LC81960322021153LGN00	10:24:26	L8	30*30	196 × 32	2021-06-02	131,81580080	OLI/TIRS	32,15
	LC81960322021169LGN00	10:24:31	L8	30*30	196 × 32	2021-06-18	128,68711290	OLI/TIRS	17,27
	LC81960322021185LGN00	10:24:34	L8	30*30	196 × 32	2021-07-04	128,26146383	OLI/TIRS	64,84
	LC81960322021201LGN00	10:24:38	L8	30*30	196 × 32	2021-07-20	130,78128027	OLI/TIRS	0,07
	LC81960322021217LGN00	10:24:45	L8	30*30	196 × 32	2021-08-05	135,58541999	OLI/TIRS	20,06
	LC81960322021233LGN00	10:24:51	L8	30*30	196 × 32	2021-08-21	141,58551943	OLI/TIRS	2,12
	LC81960332021153LGN00	10:24:49	L8	30*30	196 × 33	2021-06-02	128,77130965	OLI/TIRS	29,55
	LC81960332021169LGN00	10:24:55	L8	30*30	196 × 33	2021-06-18	125,49800262	OLI/TIRS	10,26
	LC81960332021185LGN00	10:24:58	L8	30*30	196 × 33	2021-07-04	125,18808421	OLI/TIRS	20,27
	LC81960332021201LGN00	10:25:01	L8	30*30	196 × 33	2021-07-20	128,01298283	OLI/TIRS	0,05
	LC81960332021217LGN00	10:25:09	L8	30*30	196 × 33	2021-08-05	133,22588457	OLI/TIRS	13,21
	LC81960332021233LGN00	10:25:15	L8	30*30	196 × 33	2021-08-21	139,66227643	OLI/TIRS	0,86
	LC81970322021160LGN00	10:30:39	L8	30*30	197 × 32	2021-06-09	130,18261348	OLI/TIRS	11,26
	LC81970322021176LGN00	10:30:44	L8	30*30	197 × 32	2021-06-25	128,12839264	OLI/TIRS	2,02
	LC81970322021192LGN00	10:30:46	L8	30*30	197 × 32	2021-07-11	129,02273095	OLI/TIRS	1,8
	LC81970322021208LGN00	10:30:52	L8	30*30	197 × 32	2021-07-27	132,66708000	OLI/TIRS	0,8
	LC81970322021224LGN00	10:30:59	L8	30*30	197 × 32	2021-08-12	138,12720239	OLI/TIRS	10,35
	LC81970322021240LGN00	10:31:03	L8	30*30	197 × 32	2021-08-28	144,31825254	OLI/TIRS	8,9
	LC81970332021160LGN00	10:31:03	L8	30*30	197 × 33	2021-06-09	127,04067056	OLI/TIRS	2,88
	LC81970332021176LGN00	10:31:08	L8	30*30	197 × 33	2021-06-25	124,96110268	OLI/TIRS	1,75
	LC81970332021192LGN00	10:31:09	L8	30*30	197 × 33	2021-07-11	126,06508587	OLI/TIRS	30,55
	LC81970332021208LGN00	10:31:16	L8	30*30	197 × 33	2021-07-27	130,06936196	OLI/TIRS	1,93
	LC81970332021224LGN00	10:31:23	L8	30*30	197 × 33	2022-08-12	135,95913318	OLI/TIRS	54,63
	LC81970332021240LGN00	10:31:27	L8	30*30	197 × 33	2022-08-28	142,57886283	OLI/TIRS	12,21
	LT51960332005157MTI00	10:12:33	L5	30*30	196 × 33	2005-06-06	122,78267623	TM	0
	LT51960332005189MTI00	10:12:44	L5	30*30	196 × 33	2005-07-08	120,90284853	TM	30
	LT51960332005205MTI00	10:12:56	L5	30*30	196 × 33	2005-07-24	124,41728336	TM	15
	LT51960332005221MTI00	10:13:04	L5	30*30	196 × 33	2005-08-09	130,03148070	TM	42
	LT51960332005237MTI00	10:13:10	L5	30*30	196 × 33	2005-08-25	136,66717844	TM	1

	LT51970322005180MTI00	10:18:28	L5	30*30	197 × 32	2005-06-29	123,18961971	TM	4
	LT51970322005196MTI00	10:18:37	L5	30*30	197 × 32	2005-07-15	124,88013633	TM	5
	LT51970322005228MTI00	10:18:54	L5	30*30	197 × 32	2005-08-16	134,93572125	TM	39
	LT51970332005164MTI00	10:18:47	L5	30*30	197 × 33	2005-06-13	121,37579646	TM	36
	LT51970332005180MTI00	10:18:52	L5	30*30	197 × 33	2005-06-29	120,19531274	TM	49
	LT51970332005196MTI00	10:19:01	L5	30*30	197 × 33	2005-07-15	122,12336072	TM	36
	LT51970332005212MTI00	10:19:11	L5	30*30	197 × 33	2005-07-31	126,68885201	TM	23
	LT51960321990164FUI00	09:44:51	L5	30*30	196 × 32	1990-06-13	115,08629110	TM	27
	LT51960321990212FUI00	09:44:43	L5	30*30	196 × 32	1990-07-31	119,75323344	TM	0
	LT51960321990228FUI00	09:44:38	L5	30*30	196 × 32	1990-08-16	125,42430204	TM	1
	LT51960331990164FUI00	09:45:15	L5	30*30	196 × 33	1990-06-13	112,47328468	TM	35
	LT51960331990180FUI00	09:45:14	L5	30*30	196 × 33	1990-06-29	111,44279775	TM	0
	LT51960331990212FUI00	09:45:07	L5	30*30	196 × 33	1990-07-31	117,54781001	TM	2
	LT51960331990228FUI00	09:45:02	L5	30*30	196 × 33	1990-08-16	123,51157936	TM	1
	LT51970321990155FUI00	09:51:02	L5	30*30	197 × 32	1990-06-04	116,76611817	TM	22
	LT51970321990171FUI00	09:51:01	L5	30*30	197 × 32	1990-06-20	114,28811265	TM	34
	LT51970321990187FUI00	09:50:59	L5	30*30	197 × 32	1990-07-06	114,43710394	TM	55
	LT51970321990203FUI01	09:50:54	L5	30*30	197 × 32	1990-07-22	117,20600961	TM	0
	LT51970321990219FUI00	09:50:51	L5	30*30	197 × 32	1990-08-07	122,08629452	TM	80
	LT51970321990235FUI00	09:50:46	L5	30*30	197 × 32	1990-08-23	128,21206285	TM	0
	LT51970331990155FUI00	09:51:26	L5	30*30	197 × 33	1990-06-04	114,17013566	TM	51
	LT51970331990171FUI00	09:51:25	L5	30*30	197 × 33	1990-06-20	111,67958656	TM	8
	LT51970331990187FUI00	09:51:23	L5	30*30	197 × 33	1990-07-06	111,90796325	TM	17
	LT51970331990203FUI01	09:51:18	L5	30*30	197 × 33	1990-07-22	114,86653044	TM	0
	LT51970331990219FUI00	09:51:15	L5	30*30	197 × 33	1990-08-07	119,99565415	TM	48
	LT51970331990235FUI00	09:51:10	L5	30*30	197 × 33	1990-08-23	126,40662263	TM	3

Table 24. The records of images used to extract information for Latur (India)

City	Landsat Scene Identifier	Time	Mission	Resolution	Path and Row	Acquisition date	Sun Azimuth angle	Sensor	Cloud Cover
Latur	LC81450472021100LGN00	05:15:11	L8	30*30	145 × 47	2021-04-10	111,019629	OLI/TIRS	6,65
	LC81450472021116LGN00	05:15:03	L8	30*30	145 × 47	2021-04-26	99,348729	OLI/TIRS	4,17
	LC81450472021132LGN00	05:15:00	L8	30*30	145 × 47	2021-05-12	87,778615	OLI/TIRS	0,09
	LC81450472021148LGN00	05:15:10	L8	30*30	145 × 47	2021-05-28	79,005526	OLI/TIRS	58,97
	LC81460472021091LGN00	05:21:24	L8	30*30	146 × 47	2021-04-01	116,838145	OLI/TIRS	0
	LC81460472021107LGN00	05:21:18	L8	30*30	146 × 47	2021-04-17	106,058471	OLI/TIRS	0,17
	LC81460472021123LGN00	05:21:09	L8	30*30	146 × 47	2021-05-03	94,105940	OLI/TIRS	4,15
	LC81460472021139LGN00	05:21:16	L8	30*30	146 × 47	2021-05-19	83,456276	OLI/TIRS	48,41
	LE71450472005096PFS00	05:05:05	L7	30*30	145 × 47	2005-04-06	111,125148	TM	0
	LE71460472005103ASN00	05:11:13	L7	30*30	146 × 47	2005-04-13	106,628068	TM	68
	LE71460472005119ASN00	05:11:12	L7	30*30	146 × 47	2005-04-29	95,684499	TM	6
	LE71460472005135ASN00	05:11:15	L7	30*30	146 × 47	2005-05-15	85,453497	TM	1

Table 25. The records of images used to extract information for Niihama (Japan)

City	Landsat Scene Identifier	Time	Mission	Resolution	Path and Row	Acquisition date	Sun Azimuth angle	Sensor	Cloud Cover
Niihama	LC81110362021166LGN00	01:40:47	L8	30*30	111 × 36	2021-06-15	115,531140	OLI/TIRS	96,26
	LC81110362021182LGN00	01:40:50	L8	30*30	111 × 36	2021-07-01	114,821040	OLI/TIRS	91,29
	LC81110362021198LGN00	01:40:52	L8	30*30	111 × 36	2021-07-17	117,899677	OLI/TIRS	84,07
	LC81110362021214LGN00	01:41:00	L8	30*30	111 × 36	2021-02-08	123,943646	OLI/TIRS	43,38
	LC81110372021166LGN00	01:41:10	L8	30*30	111 × 37	2021-06-15	111,796476	OLI/TIRS	98,31
	LC81110372021214LGN00	01:41:24	L8	30*30	111 × 37	2021-02-08	121,033478	OLI/TIRS	63,23
	LT51110362005154BJC00	01:28:23	L5	30*30	111 × 36	2005-06-03	114,162217	TM	72
	LT51110362005170BJC00	01:28:30	L5	30*30	111 × 36	2005-06-19	110,943315	TM	38
	LT51110362005186BJC00	01:28:34	L5	30*30	111 × 36	2005-07-05	111,243972	TM	100
	LT51110362005202BJC00	01:28:46	L5	30*30	111 × 36	2005-07-21	114,989834	TM	4
	LT51110362005218BJC00	01:28:55	L5	30*30	111 × 36	2005-08-06	121,328565	TM	65
	LT51110362005234BJC00	01:29:01	L5	30*30	111 × 36	2005-08-22	129,050253	TM	64
	LT51110372005154BJC00	01:28:47	L5	30*30	111 × 37	2005-06-03	110,810345	TM	77
	LT51110372005170BJC00	01:28:54	L5	30*30	111 × 37	2005-06-19	107,556263	TM	81
	LT51110372005186BJC00	01:28:58	L5	30*30	111 × 37	2005-07-05	107,997008	TM	73
	LT51110372005202BJC00	01:29:10	L5	30*30	111 × 37	2005-07-21	112,014120	TM	13
	LT51110372005218BJC00	01:29:19	L5	30*30	111 × 37	2005-08-06	118,677921	TM	52
	LT51110372005234BJC00	01:29:25	L5	30*30	111 × 37	2005-08-22	126,808488	TM	27
	LT51110361990161BJC00	01:01:07	L5	30*30	111 × 36	1990-06-10	104,957236	TM	68
	LT51110361990177HAJ00	01:01:06	L5	30*30	111 × 36	1990-06-26	103,472717	TM	96
	LT51110361990193BJC00	01:01:04	L5	30*30	111 × 36	1990-07-12	105,102409	TM	90
	LT51110361990225HAJ01	01:00:55	L5	30*30	111 × 36	1990-08-13	115,940658	TM	66
	LT51110361990241HAJ00	01:00:49	L5	30*30	111 × 36	1990-08-29	123,448370	TM	32
	LT51110371990161BJC00	01:01:31	L5	30*30	111 × 37	1990-06-10	102,215970	TM	85
	LT51110371990225HAJ01	01:01:19	L5	30*30	111 × 37	1990-08-13	113,779028	TM	59
	LT51110371990241HAJ00	01:01:13	L5	30*30	111 × 37	1990-08-29	121,564069	TM	62

Table 26. The records of images used to extract information for Springfield (US)

City	Landsat Scene Identifier	Time	Mission	Resolution	Path and Row	Acquisition date	Sun Azimuth angle	Sensor	Cloud Cover
Springfield	LC80230322021157LGN00	16:35:16	L8	30*30	23 × 32	2021-06-06	130,77664963	OLI/TIRS	62,33
	LC80230322021173LGN00	16:35:21	L8	30*30	23 × 32	2021-06-22	128,27415796	OLI/TIRS	0,28
	LC80230322021205LGN00	16:35:29	L8	30*30	23 × 32	2021-07-24	131,87503436	OLI/TIRS	26,8
	LC80230322021221LGN00	16:35:36	L8	30*30	23 × 32	2021-08-09	137,10321624	OLI/TIRS	99,98
	LC80230322021237LGN00	16:35:41	L8	30*30	23 × 32	2021-08-25	143,24303538	OLI/TIRS	30,27
	LC80230332021157LGN00	16:35:40	L8	30*30	23 × 33	2021-06-06	127,66709260	OLI/TIRS	71,67
	LC80230332021173LGN00	16:35:45	L8	30*30	23 × 33	2021-06-22	125,09193014	OLI/TIRS	0,46
	LC80230332021189LGN00	16:35:48	L8	30*30	23 × 33	2021-07-08	125,64406047	OLI/TIRS	46,5
	LC80230332021205LGN00	16:35:53	L8	30*30	23 × 33	2021-07-24	129,20859320	OLI/TIRS	7,93
	LC80230332021221LGN00	16:36:00	L8	30*30	23 × 33	2021-08-09	134,86065335	OLI/TIRS	76,1
	LC80230332021237LGN00	16:36:05	L8	30*30	23 × 33	2021-08-25	141,43256043	OLI/TIRS	10,63
	LC80240322021164LGN00	16:41:30	L8	30*30	24 × 32	2021-06-13	129,36928399	OLI/TIRS	0,01
	LC80240322021180LGN00	16:41:34	L8	30*30	24 × 32	2021-06-29	128,06394250	OLI/TIRS	68,25
	LC80240322021196LGN00	16:41:35	L8	30*30	24 × 32	2021-07-15	129,74515492	OLI/TIRS	99,96
	LC80240322021212LGN00	16:41:43	L8	30*30	24 × 32	2021-07-31	133,98258108	OLI/TIRS	99,96
	LC80240322021228LGN00	16:41:49	L8	30*30	24 × 32	2021-08-16	139,73942015	OLI/TIRS	28,88
	LT50230322005161PAC01	16:23:00	L5	30*30	23 × 32	2005-06-10	124,88921991	TM	73
	LT50230322005177PAC01	16:23:05	L5	30*30	23 × 32	2005-06-26	123,17966237	TM	5
	LT50230322005209PAC01	16:23:24	L5	30*30	23 × 32	2005-07-28	128,25115895	TM	46
	LT50230322005225PAC01	16:23:31	L5	30*30	23 × 32	2005-08-13	133,86809861	TM	82
	LT50230322005241PAC01	16:23:35	L5	30*30	23 × 32	2005-08-29	140,20571683	TM	0
	LT50230332005161PAC01	16:23:24	L5	30*30	23 × 33	2005-06-10	121,86538346	TM	51
	LT50230332005177PAC01	16:23:29	L5	30*30	23 × 33	2005-06-26	120,16426145	TM	7
	LT50230332005209PAC01	16:23:48	L5	30*30	23 × 33	2005-07-28	125,74493371	TM	39
	LT50230332005225PAC01	16:23:55	L5	30*30	23 × 33	2005-08-13	131,74097333	TM	18
	LT50230332005241PAC01	16:23:59	L5	30*30	23 × 33	2005-08-29	138,46730088	TM	44
	LT50240322005152PAC02	16:29:06	L5	30*30	24 × 32	2005-06-01	126,90818656	TM	9
	LT50240322005168PAC01	16:29:13	L5	30*30	24 × 32	2005-06-17	123,80236059	TM	1

	LT50240322005184GNC01	16:29:18	L5	30*30	24 × 32	2005-07-03	123,34644163	TM	18
	LT50240322005200PAC01	16:29:29	L5	30*30	24 × 32	2005-07-19	125,79639203	TM	11
	LT50240322005216PAC01	16:29:38	L5	30*30	24 × 32	2005-08-04	130,54606519	TM	52
	LT50240322005232GNC01	16:29:44	L5	30*30	24 × 32	2005-08-20	136,60585307	TM	12
	LT50230321990168XXX04	15:55:39	L5	30*30	23 × 32	1990-06-17	114,62336572	TM	33
	LT50230321990184XXX03	15:55:38	L5	30*30	23 × 32	1990-07-03	114,28230842	TM	1
	LT50230321990200XXX03	15:55:33	L5	30*30	23 × 32	1990-07-19	116,61886352	TM	5
	LT50230331990168XXX04	15:56:03	L5	30*30	23 × 33	1990-06-17	111,96264787	TM	36
	LT50230331990184XXX03	15:56:02	L5	30*30	23 × 33	1990-07-03	111,70192467	TM	1
	LT50230331990200XXX03	15:55:57	L5	30*30	23 × 33	1990-07-19	114,23198829	TM	2
	LT50230331990232XXX03	15:55:50	L5	30*30	23 × 33	1990-08-20	125,28577315	TM	83
	LT50240321990159XXX03	16:01:51	L5	30*30	24 × 32	1990-06-08	115,95728781	TM	52
	LT50240321990175AAA04	16:01:50	L5	30*30	24 × 32	1990-06-24	114,13733477	TM	0
	LT50240321990207XXX03	16:01:44	L5	30*30	24 × 32	1990-07-26	118,38400522	TM	63
	LT50240321990223XXX03	16:01:39	L5	30*30	24 × 32	1990-08-11	123,67685525	TM	88
	LT50240321990239XXX03	16:01:33	L5	30*30	24 × 32	1990-08-27	129,97076817	TM	0

Table 27. The records of images used to extract information for Villach (Austria)

City	Landsat Scene Identifier	Time	Mission	Resolution	Path and Row	Acquisition date	Sun Azimuth angle	Sensor	Cloud Cover
Villach	LC81910272021166LGN00	09:51:37	L8	30*30	191×27	2021-06-15	142,76900404	OLI/TIRS	3,14
	LC81910272021182LGN00	09:51:41	L8	30*30	191×27	2021-07-01	141,60374855	OLI/TIRS	99,91
	LC81910272021214LGN00	09:51:51	L8	30*30	191×27	2021-08-02	145,23333874	OLI/TIRS	80,09
	LC81910272021230LGN00	09:51:56	L8	30*30	191×27	2021-08-18	149,23620275	OLI/TIRS	83,88
	LC81910282021166LGN00	09:52:01	L8	30*30	191×28	2021-06-15	140,31397837	OLI/TIRS	13,75
	LC81910282021182LGN00	09:52:04	L8	30*30	191×28	2021-07-01	139,16456406	OLI/TIRS	65,99
	LC81910282021198LGN00	09:52:06	L8	30*30	191×28	2021-07-17	140,21449440	OLI/TIRS	98,74
	LC81910282021214LGN00	09:52:15	L8	30*30	191×28	2021-08-02	143,27834461	OLI/TIRS	69,92
	LC81910282021230LGN00	09:52:20	L8	30*30	191×28	2021-08-18	147,60735077	OLI/TIRS	27,76
	LT51910272005154KIS00	09:39:14	L5	30*30	191×27	2005-06-03	139,47096964	TM	6
	LT51910272005170KIS00	09:39:21	L5	30*30	191×27	2005-06-19	137,15787149	TM	8
	LT51910272005202KIS00	09:39:37	L5	30*30	191×27	2005-07-21	138,10590551	TM	54
	LT51910272005218KIS00	09:39:46	L5	30*30	191×27	2005-08-06	141,44359826	TM	84
	LT51910282005154KIS00	09:39:38	L5	30*30	191×28	2005-06-03	137,10213231	TM	5
	LT51910282005170KIS00	09:39:44	L5	30*30	191×28	2005-06-19	134,67328898	TM	2
	LT51910282005202KIS00	09:40:01	L5	30*30	191×28	2005-07-21	135,90748456	TM	36
	LT51910282005218KIS00	09:40:10	L5	30*30	191×28	2005-08-06	139,53666557	TM	50
	LT51910271990177FUI00	09:11:57	L5	30*30	191×27	1990-06-26	126,44418946	TM	12
	LT51910271990193FUI00	09:11:55	L5	30*30	191×27	1990-07-12	126,94752318	TM	2
	LT51910271990209FUI00	09:11:51	L5	30*30	191×27	1990-07-28	129,49816191	TM	6
	LT51910271990225FUI00	09:11:46	L5	30*30	191×27	1990-08-13	133,61240714	TM	4
	LT51910271990241FUI00	09:11:40	L5	30*30	191×27	1990-08-29	138,55194470	TM	11
	LT51910281990177FUI00	09:12:21	L5	30*30	191×28	1990-06-26	124,07352076	TM	11
	LT51910281990193FUI00	09:12:19	L5	30*30	191×28	1990-07-12	124,69842050	TM	2
	LT51910281990209FUI00	09:12:15	L5	30*30	191×28	1990-07-28	127,46119445	TM	6
	LT51910281990225FUI00	09:12:10	L5	30*30	191×28	1990-08-13	131,83456972	TM	3
	LT51910281990241FUI00	09:12:03	L5	30*30	191×28	1990-08-29	137,03946203	TM	3